Electromagnetic Design Optimization:

Application to a Patch Antenna Reflection Loss on a Textured Material ("Metamaterial") Substrate

by

Brian E. Fischer

A dissertation submitted in partial fulfillment
of the requirements for the degree of
Doctor of Philosophy
(Electrical Engineering: Systems)
in The University of Michigan
2005

Doctoral Committee:

Professor Andrew E. Yagle, Co-Chair
Professor John L. Volakis, Co-Chair
Professor Alfred O. Hero III
Professor Kamal Sarabandi

DEDICATION

This dissertation is dedicated to my family. This undertaking has been fraught with difficulties I could not have imagined or prepared them for at the outset – yet they have supported me completely to the end. I will always love you.

ACKNOWLEDGMENTS

First and foremost, this dissertation would not have been possible without the valuable support of my co-advisors, Prof Andrew E. Yagle and Prof John L. Volakis. Their guidance throughout the course of this work, to include suggestions for related papers, has made it what it is. Thank you for your insights and encouragement. I am grateful to the General Dynamics Advanced Information Systems Company (formerly Veridian, ERIM International, and the Environmental Research Institute of Michigan) for supporting my pursuits of related Government work and underwriting the entire effort. I am indeed grateful to my co-workers at General Dynamics who have supported many hours of stimulating discussion and ideas for “non-linear” pursuits.

PREFACE

The signal processing and electromagnetic disciplines share much in common and often work together. Joint applications include antenna array technologies such as direction finding, space-time adaptive processing, synthetic aperture radar processing, and a host of others. Fundamental staples of signal processing such as detection and estimation often find their best applications in the exploitation of electromagnetic phenomenology. Detection of phenomenological effects generally involves the quest for a signal subspace in which some observable most clearly manifests. Electromagnetic prediction work, by contrast, is not typically a subject of concern for signal processors. In some cases, "indirect" methods for solving electromagnetic systems have found application (e.g. Generalized Minimum Residual), speeding the solution of the system, but *exploitation* of the subspace associated with the solution of the electromagnetic system itself has seen little attention. Optimization of materials is a current topic of high interest in the electromagnetic community, and may turn out to be one of the chief benefits of such subspace exploitation… it should pique the interest of signal processors as well.

TABLE OF CONTENTS

LIST OF FIGURES

LIST OF TABLES

LIST OF APPENDICES

LIST OF ACRONYMS

- **2-D** Two-dimensional
- **3-D** Three-dimensional
- **ACO** Ant Colony Optimization; a multi-modal (global) optimization approach
- **BiCG** Biconjugate Gradient; matrix system solution technique
- **dB** Decibels; typically $10\log_{10}(\cdot)$, for $(\cdot)$ a dimensionless power ratio
- **EM** Electromagnetic
- **FE** Finite Element; integral-based prediction technique
- **FE-BI** Finite Element Boundary Integral; prediction technique
- **FEMA-BRICK** Finite Element Method Approach for BRICK geometries
- **GA** Genetic Algorithm; a multi-modal (global) optimization approach
- **GO** Geometric Optics; a high frequency electromagnetic scattering prediction theory
- **GMRES** Generalized Minimum Residual; matrix system solution technique
- **GTD** Geometric Theory of Diffraction; accounts for GO diffraction terms
- **MoM** Method of Moments; a low frequency electromagnetic scattering prediction theory
- **PO** Physical Optics; an high frequency electromagnetic scattering prediction theory
- **PEC** Perfect Electric Conductor
- **PTD** Physical Theory of Diffraction; accounts for PO diffraction terms
- **PMCHWT** Poggio, Miller, Chang, Harrington, Wu, and Tsai; formulation of the SIE approach
- **R-Card** Resistive impedance layer constructed as a “card” of thin material
- **RCS** Radar Cross Section
- **SA** Simulated Annealing; a multi-modal (global) optimization approach
- **SIE** Surface Integral Equation; an EM prediction approach

- **SLP** Sequential Linear Programming; a local optimization approach
- **SVD** Singular Value Decomposition
- **TLS** Total Least Squares

ABSTRACT

As electromagnetic analysis and prediction codes have improved dramatically over the past decade, design using these tools becomes an obvious next step to improve antenna or other RF device performance. Both shape and material can be varied to improve antenna characteristics, such as reflection loss and gain. Typical implementations involve a choice of applicable electromagnetic prediction codes (e.g., moment method, finite element method, etc.) nested within a nonlinear optimization construct. Currently, a popular approach to electromagnetic optimization entails use of non-linear and multi-modal optimization methods such as genetic algorithms and simulated annealing. These are known to require thousands of points to achieve a globally optimal solution, even for design spaces that are parametrically small. Generality of design is lost because one is often forced to seek from amongst an endless array of parametric models for shape and material to converge to a solution in a reasonable time.

This work demonstrates that a non-parametric solution to a difficult electromagnetic optimization problem is possible by analyzing the eigendecomposition of a unique form of a Finite Element Boundary Integral (FE-BI) system solution. This new expansion of the FE-BI matrix system provides a broadband approximant that is orders of magnitude faster than the baseline FE-BI prediction code. More importantly, the identified

functional form of the eigenvalues allows for the optimal adjustment of the electromagnetic system.

The design goal of this work is to increase the effective bandwidth of a patch antenna by texturing (via contrasting materials) the supporting substrate. The aforementioned eigenvalue adjustments are used to derive the required substrate material texture. This forms a “metamaterial” antenna design approach, as discussed in numerous publications. This new approach is a dramatic leap forward from traditional metamaterial design approaches in that no parametric assumptions or engineering judgments for texturing are required to perform an optimization. Optimized designs with only a few iterative updates are therefore possible. This work demonstrates that antenna reflection loss can be optimized over a wide bandwidth using straightforward engineering principles.

CHAPTER 1 INTRODUCTION

For over three decades, electromagnetic (EM) prediction codes have been developed and perfected to solve difficult problems; ones where geometry and material treatments are sufficiently complex that analytical solutions to Maxwell's equations can not be accomplished in closed form. Of interest typically are problems involving radiation (e.g., antennas) and scattering (e.g., radar cross section (RCS)).

There are seemingly countless applications of electromagnetic prediction needs today. As society demands faster and more miniaturized communications devices (e.g., cell phones, laptops), the need to understand increasingly complex designs with electromagnetic consequence grows. More is being asked from antennas to accommodate needs such as cell phone and GPS frequency bands. Antennas for such applications must have optimally tuned performance for specific needs and must be very small in size as shown in Figure 1-1. The left-most figure contains a recent example of a cell-phone antenna for watches based on high-dielectric (ceramic) composites. Many techniques exist for the design of such antennas today.

Figure 1-1. Application Examples of Improved Antenna Technologies

Defense needs push this envelope even further by requiring smaller and lighter-weight multi-function sensor packages with (often) extraordinary specifications as highlighted on the right-most figure. Many varied electromagnetic prediction approaches have been developed over the past decade to meet these needs; some have met with remarkable success.

In many cases today, prediction techniques are being relied on to formulate entire aircraft and aperture design concepts before ever "bending metal". Having achieved this level of sophistication, a logical extension (and ultimate goal) is the *optimization of designs* based on electromagnetic predictions. While a great deal of time and effort has been spent optimizing the performance (speed and core memory requirements) and accuracy of the codes themselves, the optimization of designs based on the codes is relatively new.

Electromagnetic optimization typically requires the interrogation of an enormous solution space, since radiation or RCS are fundamentally functions of aspect angle (azimuth and elevation), electromagnetic frequency, polarization and geometry. Geometry can be decomposed into shape (or configuration) and material treatment, the combinations of which are infinite. Not only are these solution spaces infinite, but in the most interesting

cases they are also highly sensitive to parametric adjustment. It would seem that our situation is dire indeed, but such things always depend on your point of view. It is best to be an optimist in this field of pursuit!

A typical characteristic of solutions in a given parametric space is that they are multi-modal, having a large number of local extrema. While unimodal objective functions lend themselves to a variety of useful solutions such as conjugate gradient, multi-modal objective functions have a more limited set of solution approaches if a global solution is sought. Two widely held approaches for finding global solutions to multi-modal objective functions are Genetic Algorithms (GA) and Simulated Annealing (SA). Both approaches are statistical, and both approaches are capable of reaching the global solution in the limit. Most researchers agree, however, that a solution that meets design requirements is sufficient, even if it is not the global optimum. For this reason, a GA or SA solution may be monitored and stopped prematurely if the design requirements are met.

In 1999, Rahmat-Samii and Michielssen published an entire book devoted to the optimization of electromagnetic problems using GA [35]. David Goldberg (a leader in GA research) begins the treatise by prudently asking, “whether GA’s [sic], like so many other methods that have come and gone in the past, will become a permanent part of the toolkit or will they fade like some computational hoola hoop du jour.” Goldberg concludes that GA will be here for some time based on a variety of applications to include artificial systems and economics. This author agrees. But while GA and many other optimization approaches will long be of need in a variety of complex applications, it

is troublesome to think that we can do no better for electromagnetic problems. Such general purpose optimization approaches may not afford insight into the particular reasons why a design works. Often, at the point an optimizer terminates, the user is left to question why a particular parametric combination was deemed the "best"; more troubling still is the fact that the question remains as to whether there might be a better combination given different parametric functionality, a better starting point, etc. even under the same time constraints. While there can be no "one size fits all" solution given the infinite possible electromagnetic design geometries and approaches, this work shows that for one interesting optimization problem a more thorough coupling between electromagnetic prediction and optimization can yield impressive insights into the nature of the optimum solution. Future efforts can endeavor to apply a similar approach to other electromagnetic problems of interest. In the meantime, pursuit of optimized designs using GA, SA, and the like will continue to be an essential element of enhancing our understanding of ever more complex electromagnetic design trades.

1.1 Problem Overview

A fundamental limitation of many of the current electromagnetic optimization approaches is that they do not leverage all of the information available in the electromagnetic predictions themselves. Instead, the prediction code is often treated as an "engine" or module and the optimization technique is treated as a "wrapper" along the lines of the diagram shown in Figure 1-2.

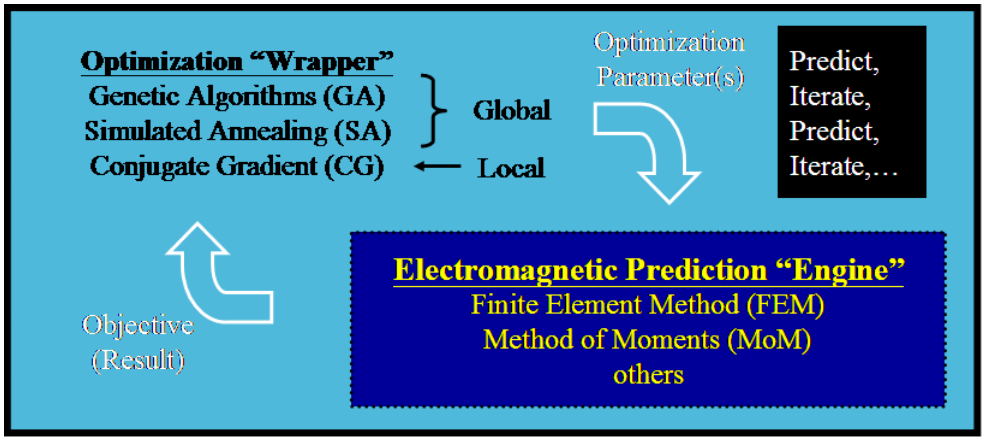

Figure 1-2. Commonly-Used Electromagnetic Optimization Approach

In theory, this optimization paradigm can reach the global minimum, provided enough time is allowed for the optimization. Time required depends on a variety of factors, but primarily on a) speed of the prediction, b) number of prediction points (e.g., frequencies) required to complete the objective, and c) required number of optimization iterations. The latter is generally proportional to the degrees of freedom afforded to the design by an appropriate parameter vector.

The anticipated process is illustrated by Figure 1-3, where the iteration process is not completely obviated, but rather the total number of iterations is greatly reduced by utilizing the information found in the prediction code electric (or magnetic) field or equivalent current. A good prediction code is required in any event to produce an optimized result that is reliable.

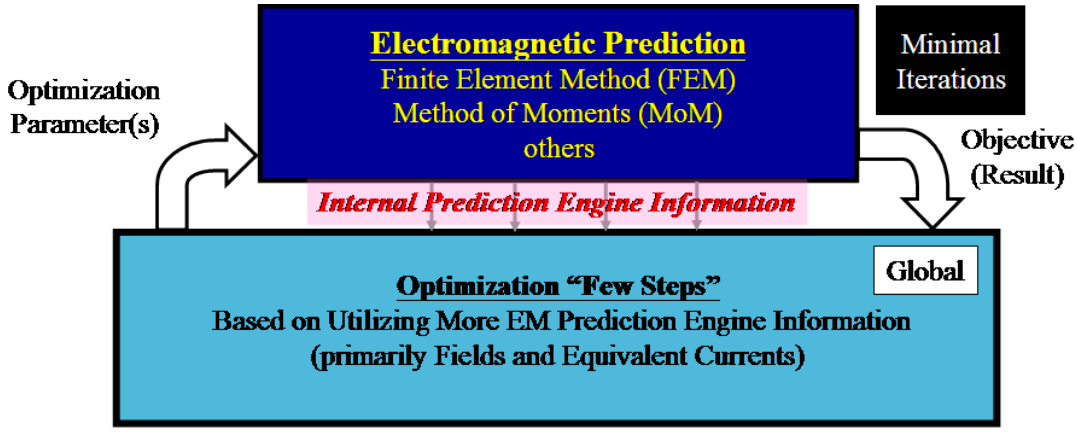

Figure 1-3. Proposed Optimization Paradigm

To begin to understand the tradespace associated with this problem, it was first necessary to become familiar with a reliable electromagnetic prediction code upon which remaining research could build. Closely associated with this was the determination of the specific application and geometry. A tremendous body of past work was available to aid this decision process. A challenge existed relative to the existing body of work regarding the manner in which parametric and local optimum solutions were sought.

1.2 Previous Work

This dissertation leverages a significant amount of past work in the areas of electromagnetics and optimization, most notably the work led by Prof John Volakis at the University of Michigan Radiation Lab, and later the Ohio State University ElectroScience Labs. That work demonstrated that textured substrates for patch antennas can be designed, predicted and tested accurately to produce wideband input reflection loss solutions [17, 18, 19, 20, 21, 22, 23, 24]. A typical geometry for such an antenna is depicted in Figure 1-4.

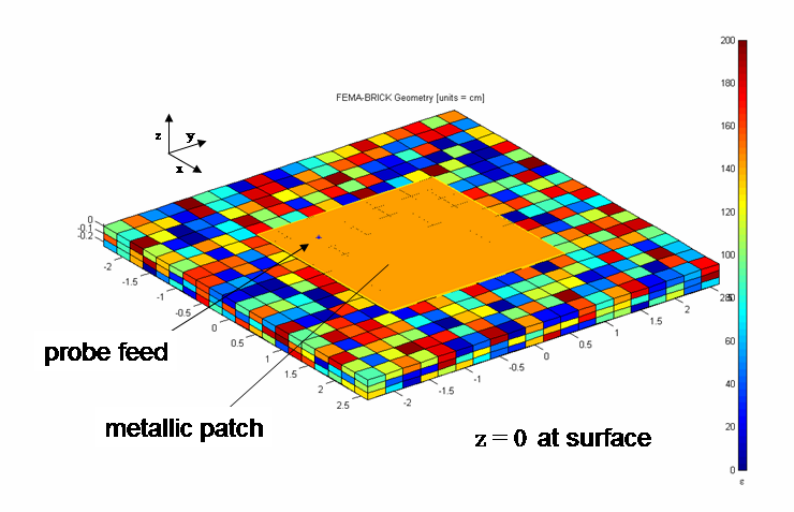

Figure 1-4. Basic Textured Substrate Patch Antenna Geometry

The geometry is constructed with regularly spaced substrate bricks of (possibly) varying permittivity and a perfect electric conductor (PEC) patch or similar radiative structure. All sides but the top are terminated in PEC, and the surface (at z=0) is embedded in an infinite ground plane. The substrate is modeled within a cavity. An offset probe feed (offset from the center of the patch) attaches to the surface patch, and is assumed to be fed by a coaxial transmission line from behind the cavity with a given characteristic impedance. The patch itself need not be rectangular. The scope of this work is limited to any metallic conductive shape that can be modeled by rectangular surface elements. Note that the rectangular modeling requirement is really driven by the particular prediction code implementation chosen for this work. Other implementations utilize more complex shapes (e.g., prism, tetrahedral), allowing for more general surface patch (and substrate) shape designs.

In developing this topic, two general categories of past work are noteworthy: 1) advancements in the speed with which Finite Element Boundary Integral (FE-BI)

predictions could be performed for a material substrate embedded in a cavity, and 2) advancements in the use of FE-BI prediction codes to optimize antenna performance via a textured substrate. The former was accomplished by Jin and Volakis [25, 26, 27] starting in 1991. The later work on optimization was pursued more recently by Kiziltas and Volakis, and Psychoudakis and Volakis [17, 18, 19, 20, 20, 21, 23, 24] starting in 2002 and continuing to the point of this writing. This work has clearly demonstrated that textured substrates can be effectively used to modify the reflection loss behavior of an antenna. Both probe-fed and gap-fed concepts have been designed, constructed and validated through extensive testing. This past work establishes two important concepts: 1) the FE-BI codes effectively predict the measurement performance of antennas with complex textured substrates *including* high-contrast textures, and 2) local optimization schemes are available.

A prime example of such an optimization is shown in Figure 1-5, courtesy of the Volakis-led team at the University of Michigan and the Ohio State University [18]. In this case, a local optimization scheme, Sequential Linear Programming (SLP) was utilized along with an FE-BI prediction code to find the solution. Notable is the fact that the frequency behavior predicted is indeed captured in the measurement, albeit with a small shift. As will be demonstrated later, such shifting can be due to lack of perfect knowledge of the substrate properties or known issues with the prediction itself. Errors in magnitude can also be attributed to imperfect construction and measurement error. Solution spaces for reflection loss prediction and measurement are tremendously sensitive to a variety of

factors, so agreement such as below is remarkable and provides confidence in the viability of textured substrates to be well-modeled and produce the expected results.

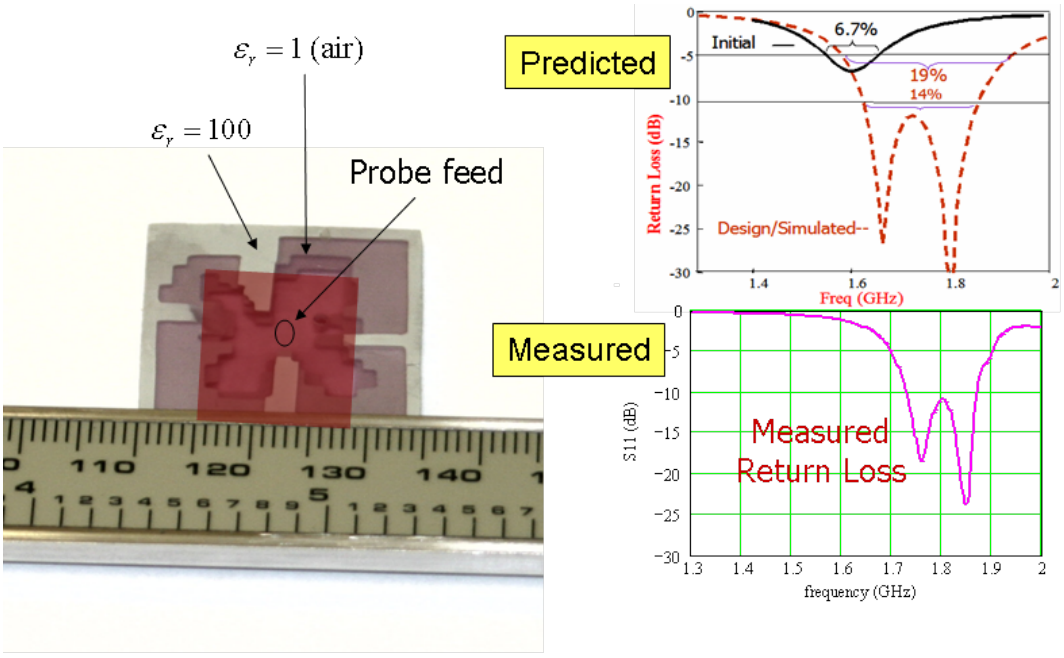

Figure 1-5. Example of a High-Contrast Textured Material Optimization (results in [18, 20])

The SLP approach makes use of the E-field unknown values in order to determine likely candidates for material modification. The basic method involves the linearization of an objective (J) [18, 34] according to

$$J\left(\boldsymbol{\alpha}^{(k+1)}\right) = J\left(\boldsymbol{\alpha}^{(k)}\right) + \sum_{i=1}^{N} \Delta\alpha_i \left(\frac{\partial J}{\partial \alpha_i}\right)\Bigg|_{\boldsymbol{\alpha}^{(k)}}, \tag{1}$$

for the parametric state vector $\boldsymbol{\alpha}^{(k)} = \left[\alpha_1^{(k)}, \alpha_2^{(k)}, \ldots, \alpha_N^{(k)}\right]$ and its deviation $\Delta\boldsymbol{\alpha} = \boldsymbol{\alpha}^{(k+1)} - \boldsymbol{\alpha}^{(k)}$, subject to the linearized volume constraint

$$V_{\min}^{(m)} - V^{(m)}\left(\boldsymbol{\alpha}^{(k)}\right) \le \sum_{i=1}^{N} \Delta\alpha_i \left(\frac{\partial V^{(m)}}{\partial \alpha_i} \right)\Bigg|_{\boldsymbol{\alpha}^{(k)}} \le V_{\max}^{(m)} - V^{(m)}\left(\boldsymbol{\alpha}^{(k)}\right) \tag{2}$$

(V is a volumetric density related to the available materials), other general (g) constraints

$$g_j^{\min} - g_j\left(\boldsymbol{\alpha}^{(k)}\right) \le \sum_{i=1}^{N} \Delta\alpha_i \left(\frac{\partial g}{\partial \alpha_i} \right)\Bigg|_{\boldsymbol{\alpha}^{(k)}}, \tag{3}$$

and the parametric limits

$$\Delta\alpha_{\max} \le \Delta\alpha_i \le \Delta\alpha_{\min}. \tag{4}$$

From an initial condition ($\boldsymbol{\alpha}^{(0)}$), and an initial $\Delta\boldsymbol{\alpha}$ deviation, the objective and its update may be computed. From that point forward, the updates are guided by the relative success of subsequent deviations toward the objective goals. Constraints are used to ensure that a given update does not "overshoot" the local optimum. Additional constraints regarding the relative density of the material values are also imposed. The general conclusions regarding the approach were to be cautious in allowing large deviations to take place. Large deviations from state to state lead to inconsistent (and non-convergent) results.

Numerous examples of electromagnetic optimization using genetic algorithms can be found in the literature. Haupt may have first popularized the idea by introducing such examples and demonstrating the relative ease with which an optimization could be constructed [30]. In that paper, he even offered a small GA code fragment (binary) in Matlab that could be tested in an afternoon by any interested researcher. A thorough

treatment of wire antenna design, linear and planar array optimization, wideband array optimization, and electromagnetic filter design via GA is provided in [35]. It is a fair statement that a consistent theme of all treatments of electromagnetic designs with a GA optimization involves a great deal of focus on the parameters of the optimizer and a high-level parameterization of the electromagnetic problem. If the number of independent parameters becomes large, the GA may not find the solution in a reasonable amount of time.

1.3 Contributions of this Dissertation

This dissertation demonstrates for the first time that a specific decomposition of a computational electromagnetic formulation can be used to provide a rapid solution and *non-parametric* optimization of a complex electromagnetic problem. Specifically, via an eigendecomposition and derived functional form for the eigenvalues, this work shows that it is possible to work within such a subspace to optimize the wideband performance of an electrically small antenna. The general flow of key accomplishments under this work can be viewed according to Figure 1-6, where the first block represents the starting point and block 2 and 3 represent the new developments leading to example case demonstrations.

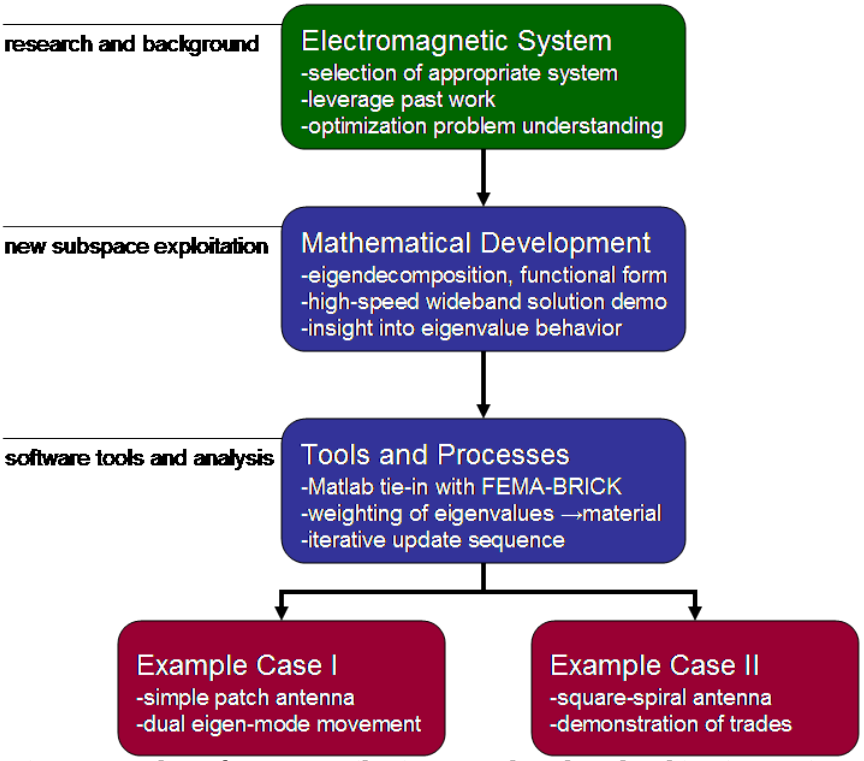

Figure 1-6. Flow of Key Contributions Developed Under this Dissertation

The wideband optimum return loss sought is realized by texturing the substrate beneath the antenna. One key ingredient for successful application of the approach discussed herein is to linearize the explicit frequency dependence of the electromagnetic system. If this is accomplished, a fundamental insight into the nature of the behavior of the system can be found. This insight enables the movement of resonant terms within the eigenvalue-structure, allowing for near-ideal wideband objective performance.

The development of a specific electromagnetic system (Finite Element Boundary Integral [FE-BI]) is included to thoroughly explain the frequency dependence and set up a useful eigendecomposition. Mathematically, it is shown that a Taylor approximant to the appropriate Green's function results in a quadratic functional form for the system versus

frequency. This leads to a new approach for extremely rapid wideband solutions. In Chapter 3, the insights and uses of eigendecomposition are first introduced, starting with this wideband example. The full power of the approach is shown in Chapter 5, where a complete wideband formulation for eigenvalue functionality is highlighted. This allows for very fast wideband solutions for a given system [3], and further provides for the organized movement of eigenvalue terms toward an optimized system.

A library of Matlab tools was developed to facilitate the demonstration of mathematical results contained in this dissertation; these are described in Appendix C. This effort culminates in the demonstration of two basic optimization cases using generalized numerical optimization schemes.

1.4 Organization of this Dissertation

The remainder of this dissertation is organized into six main chapters. Chapter 2, Problem Statement, describes the problem by examining the tradespace associated with electromagnetic optimization and describing the goal of this work. This chapter contains a description of the chosen electromagnetic prediction code for this work (FEMA-BRICK) and introduces the generalized optimization problem. Chapter 3, Linear System Optimization Approach, goes into appropriate detail of the Finite Element Boundary Integral (FE-BI) electromagnetic system to establish the baseline for a thorough eigen-space analysis. Parameters necessary to ensure the appropriate conditioning of an FE-BI system are highlighted and an early attempt to optimize the system based on the Total Least Squares (TLS) approach is visited. Chapter 4, Narrowband System Optimization, introduces the exploitation of the eigendecomposition for optimization; showing that

eigenvalues can be modified to provide a useful textured material update at a single frequency. Chapter 5, Wideband System Optimization, then develops the complete wideband functional form for eigenvalues in a particular eigendecomposition of the FE-BI system; demonstrating how the eigenvalue functional form provides mathematical insight into electromagnetic system behavior that can lead to optimization. Chapter 6, Wideband System Optimization Results, then puts the mathematical development of the previous chapter to work and illustrates two key examples of design optimization. Each of these two cases is based on different patch radiator geometries. Finally, 6.2.1 summarizes the development and results of the work and provides recommendations for future work.

CHAPTER 2 PROBLEM STATEMENT

It has long been known that obtaining reliable low losses at the feed of patch antennas over a wide bandwidth is a tricky business. By their very nature, patch antennas are capacitively-coupled to a ground plane with a dielectric substrate that is sandwiched between the ground plane and the patch. A poor design will be sensitive to even small substrate material uncertainties. Like many things in engineering, a tradespace emerges. One can choose to employ lossy substrates that encourage more stable bandwidth behavior, but also obviously ensure a fair amount of loss across the band (reduced gain). With higher material losses, one increasingly loses the ability to correlate reflection loss to antenna radiation. Low reflection losses are important primarily because lower input losses should translate to improved radiation by the patch antenna element.

In the previous chapter, the nature and setup of the problem was provided. In this chapter, the mathematical setup of the problem is given. The problem of optimizing the reflection loss for a probe-fed patch antenna on a textured low-loss material substrate over a wide bandwidth is highlighted. Included is the overall mathematical context of the optimization, the specific choice of electromagnetic prediction (approach and actual computer program with modifications), and introduction to the optimization problem.

2.1 Background

Prediction codes are based on a variety of basic scattering theories or principles and combinations thereof – all solve Maxwell's equations in one form or another. Today, these basic theories are often combined to form *hybrid* codes – typically a self-consistent formulation hinging on some matching condition (e.g., at a surface). Scattering theories are usually identified as having predominantly low or high frequency regions of applicability; involving a trade-off between speed, memory and accuracy. Codes based on the Method of Moments (MoM) and Finite Elements (FE) are often considered to be most applicable to low frequency problems. These solutions are integral-based and have the characteristic of high accuracy at the expense of the computation and inversion of an impedance matrix that must be recomputed for each individual frequency (and angle and polarization in the case of monostatic scattering). Asymptotic codes based on geometric or physical optics (GO or PO) and improved versions that consider the effects of diffraction (GTD – geometric theory of diffraction, PTD – physical theory of diffraction), are often considered to be most applicable to high frequency problems, since their code complexity is low (resulting in high speed) and accuracy improves with increasing frequency. These comprise only a few examples; there are many other types of prediction code theoretic foundations and variants. Designs at lower frequencies can be more challenging due to the need to consider the entire geometry; separating the geometry into smaller components is problematic due to increased interaction terms at lower frequencies.

In addition to low and high frequency characteristics, predictions can be formulated in two or three dimensions. Two-dimensional (2-D) codes are an attractive way to analyze

long (cylindrical) geometries, since they can be computed more easily than their three-dimensional (3-D) counterparts. The assumption made is that the 2-D geometry extends to infinity in the third dimension (an infinite cylinder). Scattering for 2-D is often reported as *echo width* in units of dBKE (decibels relative to a knife edge [flat strip]), whereas scatter in 3-D is typically reported as RCS in units of dBsm (decibels relative to a square meter). Body of revolution (BOR) codes also exist, which can efficiently predict RCS in dBsm if revolving a contour about an axis can generate the 3-D body.

In order for predictions to be formulated on a computer, the problem must be discretized. A numerical interpretation of an object geometry is the result. There are in principle an infinite number of ways to do this. As an example, one could assume the entire world consists of non-interacting spherical metal objects. Since a theoretic infinite series (Mie series) exists to predict spheres, this provides a good underpinning for a code. All that is needed is a way to describe to the code the location and size of all the spheres. A coherent sum that accounts for these discrete values then results in a prediction. The trouble is, most things in the world can not be modeled this way.

Ultimately, all computer-based prediction codes involve the formulation of a discrete system of equations that must be solved. A great deal of community effort has been applied to the problem of solving these systems (which only grow in size and complexity) in a reasonable amount of time. For instance, given a matrix system $\mathbf{AX} = \mathbf{B}$, it is a simple matter to solve for $\mathbf{A} = \mathbf{X}^{-1}\mathbf{B}$; simple, that is, until the matrix sizes approach 100,000 unknowns! Many approaches exist to solve $\mathbf{AX} = \mathbf{B}$ for $\mathbf{A}$ that do not require matrix inversion (i.e., indirect approaches such as biconjugate gradient [BiCG] or

generalized minimum residual [GMRES]). In some cases, they are able to leverage matrix structure (e.g., sparsity or symmetry) to speed a solution.

The solution is a function of a geometry that the user provides, and *must be cast in a particular context*. There are no "one-size-fits-all" electromagnetic prediction solutions. The FEMA-BRICK program, discussed next, is no exception to this rule. This prediction code was built around a particular hybrid finite element (FE) and method of moments (MoM) concept for the geometry associated with a cavity embedded in an infinite ground plane.

2.2 The FEMA-BRICK Program

A large variety of electromagnetic codes exist which are applicable to the general optimization problem of interest. That said, any given code requires significant effort in order to "retrofit" a new optimization paradigm, so only one could be chosen for detailed analysis. To help ensure accuracy, an integral-based code was chosen as appropriate to the application. An integral-based code comes at the expense of processing speed, but accuracy was deemed to be paramount when investigating key optimization parameters. This section begins with a brief review of the general FE-BI formulation followed by the specific treatment for the case of a cavity embedded in an infinite metallic plane. This is relevant since the FEMA-BRICK prediction code (upon which all of the examples for this work are based) involves the specific FE-BI solution relevant to a cavity structure meshed in rectangular brick regions.

FEMA-BRICK, which is a brick-based Finite Element Method Analysis (FEMA) code [typically referred to as a finite element boundary integral (FE-BI) code] is a hybrid between Method of Moments (MoM) and Finite Elements (FE) solutions.

2.2.1 General Three-Dimensional FE-BI System Development

The general formulation begins with an arbitrary geometry comprised of a closed contour which contains some dielectric material region(s) and conductive material according to Figure 2-1. As shown, internal fields are spatially dependent on the local material values. This forms the basis of the textured material (metamaterial) design concept discussed in this work.

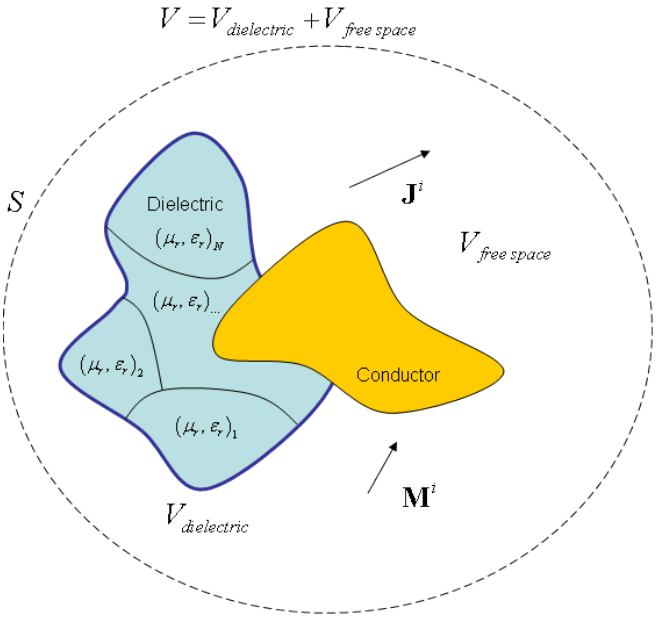

Figure 2-1. General 3-D FE-BI Geometry

The geometry above may be characterized by the weak form of the vector wave equation given by [28]

$$\int_V \left[\frac{\nabla \times \mathbf{E}^{\text{int}} \cdot \nabla \times \mathbf{W}_i}{\mu_{r_n}} - k_0^2 \, \varepsilon_{r_n} \mathbf{E}^{\text{int}} \cdot \mathbf{W}_i \right] dV - j k_0 Z_0 \oint_S \left[\hat{\mathbf{n}} \times \mathbf{H}^{\text{int}} \cdot \mathbf{W}_i \right] dS = f_i^{\text{int}}, \qquad (5)$$

where

$$f_i^{\text{int}} = -\int_V \left\{ \nabla \times \left[\frac{\mathbf{M}^i}{\mu_{r_n}} \right] + j k_0 Z_0 \mathbf{J}^i \right\} \cdot \mathbf{W}_i \, dV, \qquad (6)$$

and

$\mathbf{E}^{\text{int}}, \mathbf{H}^{\text{int}} \equiv$ Internal Electric and Magnetic Field Vectors
$\mathbf{M}^i, \mathbf{J}^i \equiv$ Impressed Excitation Currents
$\varepsilon_{r_n}, \mu_{r_n} \equiv$ Constitutive Parameters of Material in Region *n*
$Z_0 \equiv$ Free Space Impedance ($\sqrt{\mu_0/\varepsilon_0}$)
$k_0 \equiv$ Wavenumber ($2\pi/\lambda_0$)
$\mathbf{W}_j \equiv j^{\text{th}}$ Internal Edge Expansion Basis
$f_i^{\text{int}} \equiv$ Internal Excitation Vectors

For FE-BI to be successful, three conditions must be met (three separate equations) which ensure mesh closure on the boundary of the finite element mesh and that the tangential electric and magnetic fields are properly related. These are delineated as the *interior*, *exterior*, and *coupling* equations. The interior equation is given by equation (5). The exterior equation is given by

$$\begin{aligned} -\frac{1}{2}\oint_S \left[\mathbf{Q}_i \cdot \left(\hat{\mathbf{n}} \times \mathbf{H}^{\text{int}} \right) \right] dS - \oint_S \oint_{S'} \left[\mathbf{Q}_i \cdot \left(\hat{\mathbf{n}} \times \nabla \times \overline{\overline{G}} \times \hat{\mathbf{n}}' \right) \right] \cdot \mathbf{H}^{\text{int}} dS' dS \\ - jk_0 Y_0 \oint_S \oint_{S'} \left[\mathbf{Q}_i \cdot \left(\hat{\mathbf{n}} \times \overline{\overline{G}} \times \hat{\mathbf{n}}' \right) \right] \cdot \mathbf{E}^{\text{ext}} dS' dS = f_i^{\text{ext}} \end{aligned}, \qquad (7)$$

where

$$f_i^{\text{ext}} = -\oint_S \mathbf{Q}_i \cdot \hat{\mathbf{n}} \times \left[\mathbf{H}^{inc} + \mathbf{H}^{refl} \right] dS \,, \tag{8}$$

and

$$\mathbf{H}^{\text{ext}} = \mathbf{H}^{inc} + \mathbf{H}^{refl} + \mathbf{H}^{scat} \text{ (decomposition of external fields)}$$
$$\overline{\overline{G}} \equiv \text{Relevant Dyadic Green's Function}$$
$$k_0 \equiv \text{Wavenumber } (2\pi/\lambda_0)$$
$$Y_0 \equiv \text{Free Space Impedance } (1/Z_0)$$
$$\mathbf{Q}_j \equiv j^{\text{th}} \text{ External Edge Expansion Basis}$$
$$f_i^{\text{ext}} \equiv \text{External Excitation Vectors}$$

The coupling equation is given by

$$\oint_S \left[\mathbf{Q}_i \cdot \hat{\mathbf{n}} \times \left(\mathbf{E}^{\text{int}} - \mathbf{E}^{\text{ext}} \right) \right] dS = 0 \,, \tag{9}$$

completing a particular form of the most general FE-BI equations. Solving for these equations requires that a mesh be established for some canonical geometry which lends itself to efficient solution. Solving these equations for general (arbitrary) geometries can be very computationally intensive.

2.2.2 Three-Dimensional FE-BI for a Cavity in an Infinite Ground Plane

One of the most successful applications of the FE-BI approach involves a geometry composed of a cavity embedded in an infinite ground plane. The cavity may be completely or partially filled with a dielectric as depicted in Figure 2-2, where the relevant Green's function may now be associated with radiation from the infinite plane, thus obviating large BI computations. In essence, the BI computation need only be concerned with the non-zero (non-metallic) edges in the aperture itself.

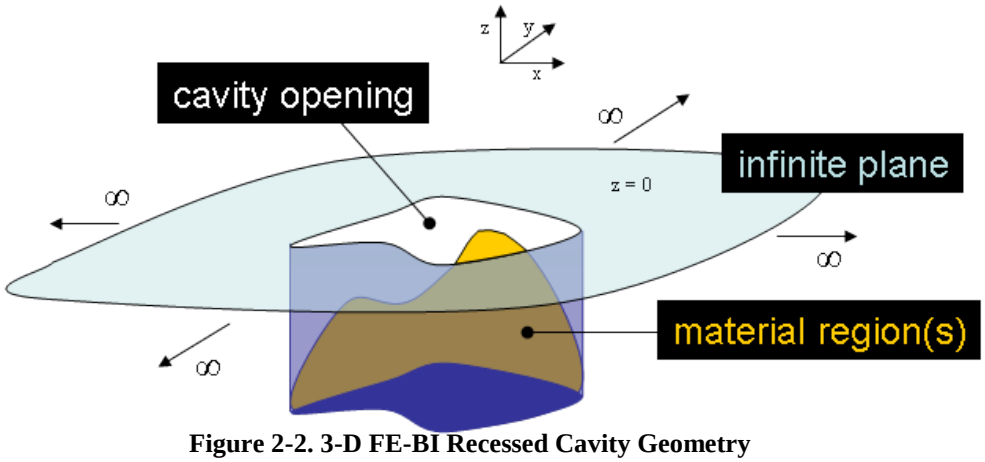

Figure 2-2. 3-D FE-BI Recessed Cavity Geometry

An additional efficiency is realized by recognizing that the magnetic fields in the aperture can be completely represented by the electric field unknowns. Also the volume (internal) expansion function bases can be reduced as equal to the surface (external) expansion function bases in the aperture, ensuring enforcement of electric field boundary conditions at the aperture. This allows the established equations which are normally written as two "separate, but coupled" equations to be written as a single equation according to

$$\sum_{j=1}^{N} E_j \left\{ \int_V \left[\frac{\nabla \times \mathbf{W}_i \cdot \nabla \times \mathbf{W}_j}{\mu_r} - k_0^2 \, \varepsilon_r \mathbf{W}_i \cdot \mathbf{W}_j \right] dV - k_0^2 \int_S \int_{S'} \left[\mathbf{W}_i \cdot \hat{\mathbf{z}} \times \overline{\overline{G}}_{e2} \times \hat{\mathbf{z}} \cdot \mathbf{W}_j \right] dS' dS \right\} = f_i^{\text{int}} + \tilde{f}_i^{\text{ext}}, \quad i = 1, 2, 3, \ldots, N \tag{10}$$

where

$$\tilde{f}_i^{\text{ext}} = j \, k_0 \, Z_0 \, f_i^{\text{ext}}$$
$$\overline{\overline{G}}_{e2} = 2\overline{\overline{G}}_0 = -\left(\overline{\overline{I}} + \frac{\nabla\nabla}{k_0^2} \right) \left[\frac{e^{-jk_0 R}}{2\pi R} \right], \tag{11}$$

and

$E_j \equiv j^{\text{th}}$ Edge Unknown Value

$\varepsilon_r, \mu_r \equiv$ Constitutive Parameters of Material

$k_0 \equiv$ Wavenumber $(2\pi/\lambda_0)$

$\mathbf{W}_j \equiv j^{\text{th}}$ Edge Expansion Basis

$\overline{\overline{G}}_{e2} \equiv$ Electric Dyadic Green's Function of the Second Kind

$\overline{\overline{G}}_0 \equiv$ Free Space Dyadic Green's Function

$f_i^{\text{int}}, \tilde{f}_i^{\text{ext}} \equiv$ Excitation Vectors (internal and external)

2.2.3 FEMA-BRICK Prediction Code

The FEMA-BRICK electromagnetic prediction code is based on the development of a cavity solution by imposing a regular mesh in a rectangular (brick) structure as depicted by example in Figure 2-3. Note in the figure that the infinite ground plane is assumed at the z = 0 surface, and extends beyond the aperture in all directions.

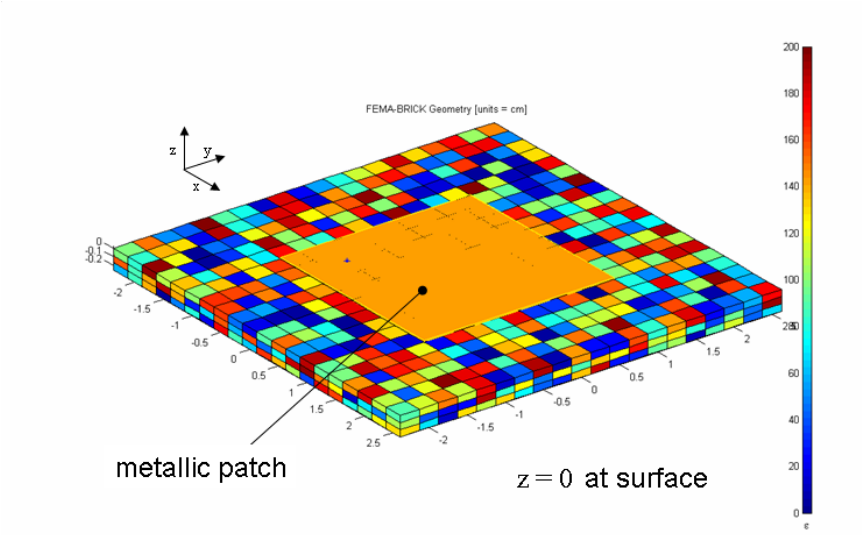

Figure 2-3. 3-D FEMA-BRICK Geometry

By constructing the geometry this way, efficiency is gained: specifically, the BI matrix structure becomes symmetric block Toeplitz allowing for computation of vector

contributions via Fast Fourier Transform (FFT) [28, 29]. Within FEMA-BRICK, there is no need to maintain the entire matrix structure in core memory. The system is solved using the biconjugate gradient approach (BiCG) and the contributions to the solution vector (field vector) are summed explicitly at each iterative update. Since the FE matrix portion is sparse, and the BI matrix contribution can now be computed quickly, this produces a very efficient prediction scheme. However, the optimization work for this purpose requires the explicit elements from the matrix system. These matrices were extracted from the executable FEMA-BRICK code into the Matlab environment for subsequent processing. Details of the code modifications are discussed in Appendix C.

FEMA-BRICK is nearly an ideal code for this type of application. The primary exception (as will be seen later) is that the substrate model is limited to consist only of bricks, and the patch antenna geometry must be constructed from square facets. Use of round (or spiral) patch geometries is not possible.

An example of a FEMA-BRICK prediction as compared to measured data is contained in the FEMA-BRICK user's guide [36] and is reproduced below in Figure 2-4. The figure highlights the improved accuracy afforded by FEMA-BRICK for measurement comparison, relative to a prior (calculated) approach.

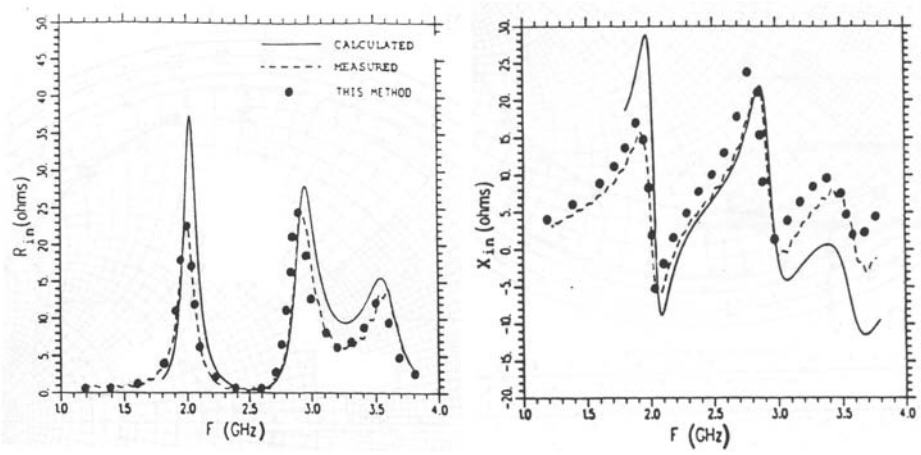

Figure 2-4. FEMA-BRICK Performance Versus Measured Data for Geometry at $\varepsilon_r = 2.17 - j0.0033$ **[36]**

This measurement and prediction was accomplished for the geometry shown in Figure 2-5. It is a non-ideal case to compare reflection loss to radiation, given the resistive load. Nevertheless, this made for an interesting starting point and verified that the code itself was working as expected.

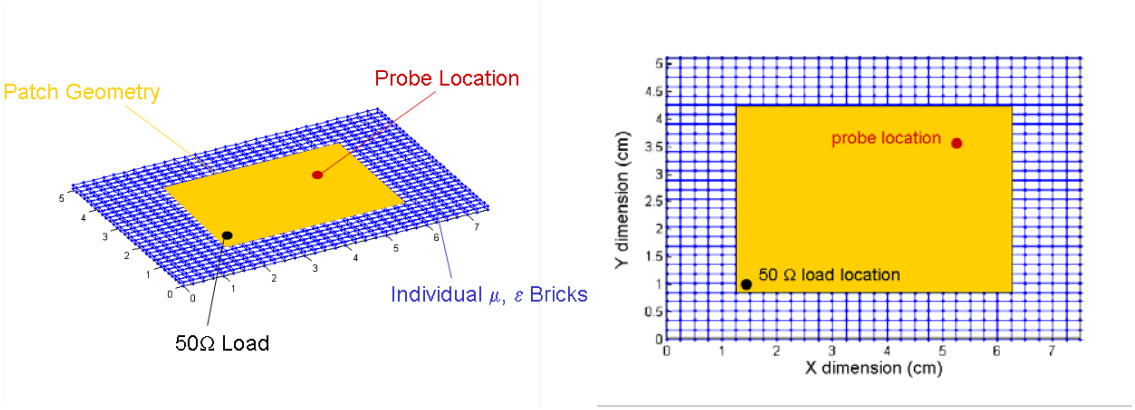

Figure 2-5. Patch Antenna Configuration Utilized for Initial FEMA-BRICK Comparison Work

Of interest is the behavior encountered by such a geometry with various solid substrates. As stated earlier, the optimization problem space is one characterized by a high degree of sensitivity. Sensitivity increases in proportion to dielectric material density. As

permittivity increases, wavelength in the substrate decreases (as $\sqrt{\varepsilon_r}$) and the pattern scintillations grow more rapid; effectively there is a compression effect as material becomes increasingly dense. Results of predicted input impedance (real and imaginary) and the corresponding reflection loss (in dB; assuming a 50Ω input) are shown for the case of air (Figure 2-6), as well as $\varepsilon_r = 2.17 - j0.0033$ (Figure 2-7). Observe that the spike near 2.9 GHz moves to approximately 2 GHz in proportion to $\sqrt{2.17}$ as expected. Increased field sensitivity as a function of increased dielectric is a desirable quality for optimization, as long as it is controlled.

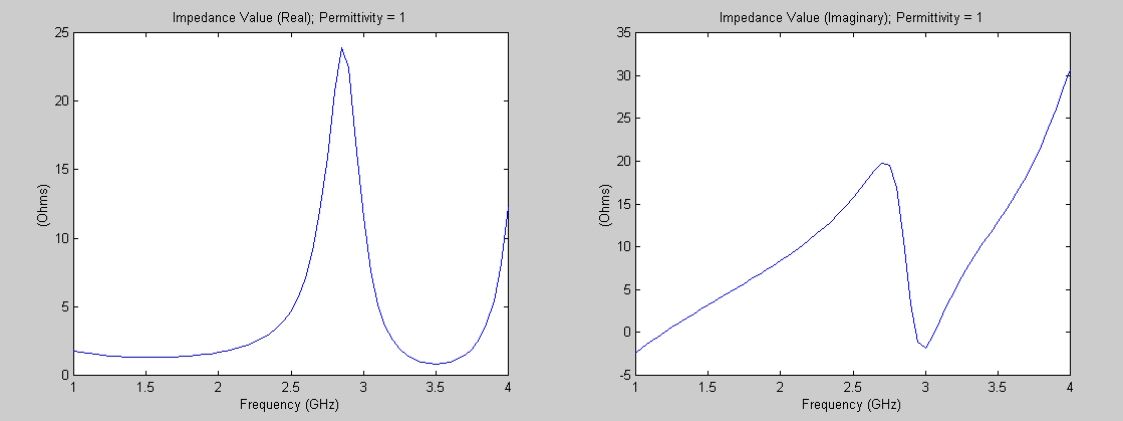

Figure 2-6. FEMA-BRICK Results for Prescribed Geometry at $\varepsilon_r = 1$; Real (left) and Imaginary (right) Predicted Input Impedance

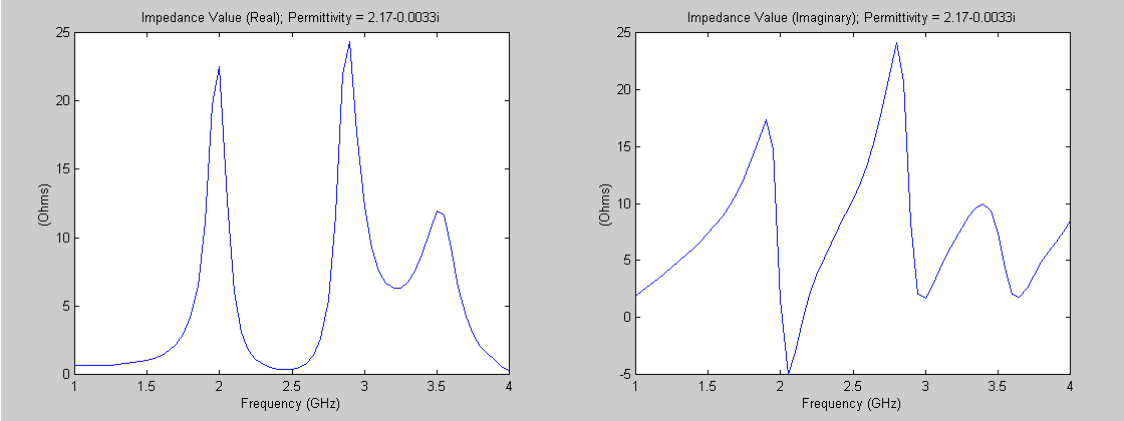

Figure 2-7. FEMA-BRICK Results for Prescribed Geometry at $\varepsilon_r = 2.17 - j0.0033$; Real (left) and Imaginary (right) Predicted Input Impedance [Note Comparison to Figure 2-4]

Probe input impedance is calculated by determining the unknown electric field at the probe location and dividing by the input (source) current, which is defined by the user (typically set to unity). Mathematically, input impedance is given by

$$Z_L = \left.\frac{\left\langle \mathbf{E}^{\text{int}}, \mathbf{W}_\eta \right\rangle}{\mathbf{J}^\eta}\right|_{\mathbf{J}^\eta = 1} = \left\langle \mathbf{E}^{\text{int}}, \mathbf{W}_\eta \right\rangle. \tag{12}$$

For a given input probe current, input impedance is dictated by the predicted electric field at the feed element location (denoted by η in the relation above). For a given geometry, this simply serves to illustrate that the E-field unknown at the probe location and the physical input impedance are directly proportional. For much of this work, optimizations are associated with the actual system unknowns (Z-directed E-field). The input impedance reflection loss or other more physical quantities are not highlighted directly until the completion of the optimization.

2.2.4 FEMA-BRICK FE-BI System

The FE-BI system can be described by the matrix system given by [28]

$$\left(\left[\mathbf{A}\right] + \begin{bmatrix} \left[\mathbf{G}\right] & \left[\mathbf{0}\right] \\ \left[\mathbf{0}\right] & \left[\mathbf{0}\right] \end{bmatrix} \right) \begin{bmatrix} \mathbf{E}_j^{\text{bi}} \\ \mathbf{E}_j^{\text{fe}} \end{bmatrix} = \begin{bmatrix} \tilde{\mathbf{f}}_i^{\text{ext}} \\ \mathbf{f}_i^{\text{int}} \end{bmatrix}, \tag{13}$$

where the finite element (FE) contribution is given by $\left[\mathbf{A}\right]$ and the boundary integral (BI) Green's function contribution is given by $\left[\mathbf{G}\right]$. The unknowns are *X*-, *Y*-, and *Z*-directed E-field components associated with the edges of the individual physical mesh elements. Each brick edge in Figure 2-3 above is described by a unique unknown. Edge elements that are strictly internal to the cavity have only a FE contribution and no BI contribution (hence the block form above).

Sufficient detail for computation of all elements of the above system is provided in [28], with solutions based on a linear edge-based expansion function.

The individual FE and BI matrix components can be further decomposed according to

$$\left[\mathbf{A}\right] = \mathbf{A}^{(1)}\left(\mu\right) + \mathbf{A}^{(2)}\left(\varepsilon\right) \tag{14}$$

and

$$\begin{bmatrix} \mathbf{G} & \mathbf{0} \\ \mathbf{0} & \mathbf{0} \end{bmatrix} = \mathbf{G}^{(1)} + \mathbf{G}^{(2)}. \tag{15}$$

Explicitly,

$$
\begin{aligned}
\mathbf{A}_{ij}^{(1)} &= \int_V \left[\frac{\nabla \times \mathbf{W}_i \cdot \nabla \times \mathbf{W}_j}{\mu_r} \right] dV \\
\mathbf{A}_{ij}^{(2)} &= -k_0^2 \int_V \left[\varepsilon_r \mathbf{W}_i \cdot \mathbf{W}_j \right] dV \\
\mathbf{G}_{ij}^{(1)} &= \frac{k_0^2}{2\pi} \int_S \int_{S'} \left[\mathbf{W}_i \cdot \hat{\mathbf{z}} \times \overline{\overline{I}} \times \hat{\mathbf{z}} \cdot \mathbf{W}_j \right] \frac{e^{-jk_0 R}}{R} dS' dS \\
\mathbf{G}_{ij}^{(2)} &= \frac{1}{2\pi} \int_S \int_{S'} \left[\mathbf{W}_i \cdot \hat{\mathbf{z}} \times \left(\nabla \nabla \frac{e^{-jk_0 R}}{R} \right) \times \hat{\mathbf{z}} \cdot \mathbf{W}_j \right] dS' dS
\end{aligned}
\quad , \tag{16}
$$

recognizing that the BI can be further decomposed by breaking the Green's function into its two explicit sub-components [see Equation (11)].

Additionally, for the FEMA-BRICK code used for this study, the *X*, *Y*, and *Z* interaction terms are explicitly called out according to

$$
\mathbf{A}^{(1)}(\mu) = \begin{bmatrix} \mathbf{A}_{xx}^{(1)}(\mu) & \mathbf{A}_{xy}^{(1)}(\mu) & \mathbf{A}_{xz}^{(1)}(\mu) \\ \mathbf{A}_{yx}^{(1)}(\mu) & \mathbf{A}_{yy}^{(1)}(\mu) & \mathbf{A}_{yz}^{(1)}(\mu) \\ \mathbf{A}_{zx}^{(1)}(\mu) & \mathbf{A}_{zy}^{(1)}(\mu) & \mathbf{A}_{zz}^{(1)}(\mu) \end{bmatrix}, \tag{17}
$$

$$
\mathbf{A}^{(2)}(\varepsilon) = \begin{bmatrix} \mathbf{A}_{xx}^{(2)}(\varepsilon) & \mathbf{0} & \mathbf{0} \\ \mathbf{0} & \mathbf{A}_{yy}^{(2)}(\varepsilon) & \mathbf{0} \\ \mathbf{0} & \mathbf{0} & \mathbf{A}_{zz}^{(2)}(\varepsilon) \end{bmatrix}, \tag{18}
$$

$$
\mathbf{G}^{(1)} = \begin{bmatrix} \mathbf{G}_{xx}^{(1)} & \mathbf{0} & \mathbf{0} \\ \mathbf{0} & \mathbf{G}_{yy}^{(1)} & \mathbf{0} \\ \mathbf{0} & \mathbf{0} & \mathbf{0} \end{bmatrix}, \tag{19}
$$

and

$$\mathbf{G}^{(2)} = \begin{bmatrix} \mathbf{G}_{xx}^{(2)} & \mathbf{G}_{xy}^{(2)} & \mathbf{0} \\ \mathbf{G}_{xy}^{(2)} & \mathbf{G}_{yy}^{(2)} & \mathbf{0} \\ \mathbf{0} & \mathbf{0} & \mathbf{0} \end{bmatrix}. \tag{20}$$

Note that the aperture of the cavity is explicitly in the *x*-*y* plane ($z = 0$), obviating any need for a z term in the BI matrices. The FE matrices are typically very sparse as shown in Figure 2-8, while the BI matrices are in general dense (see Figure 2-9).

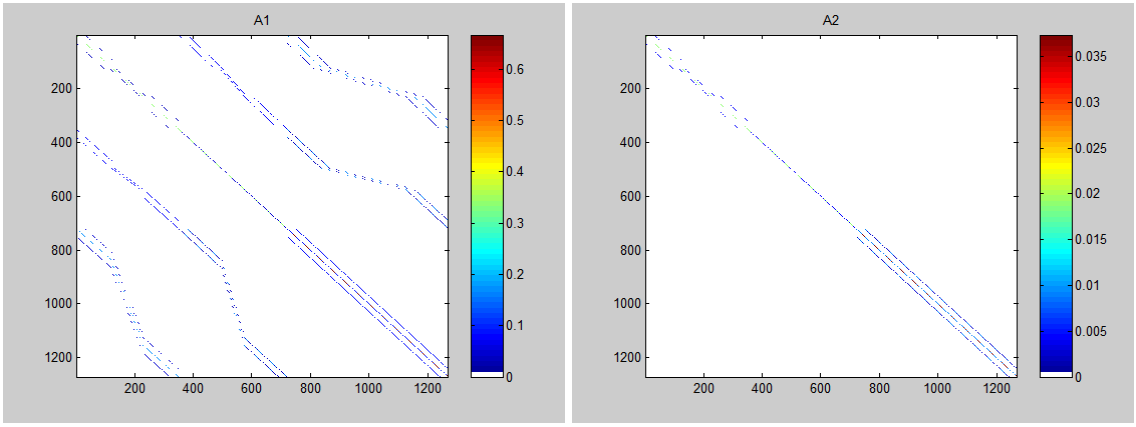

Figure 2-8. Typical Structure of Sparse Finite Element (FE) Matrices

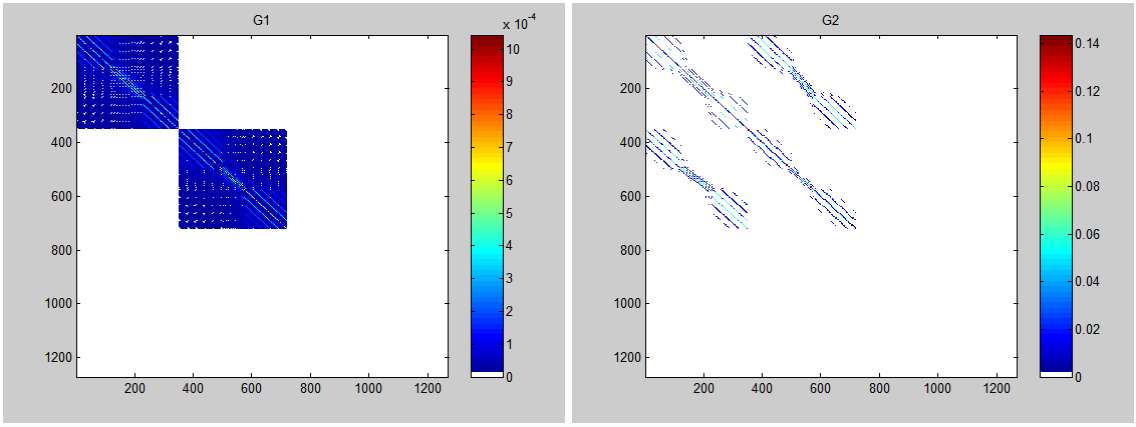

Figure 2-9. Typical Structure of Dense Boundary Integral (BI) Matrices

2.3 Optimization Problem Introduction

Electromagnetic optimization typically requires the interrogation of an enormous solution space, since radiation or RCS are fundamentally functions of aspect angle (azimuth and elevation), electromagnetic frequency, polarization and geometry. Geometry can be further decomposed into shape (or configuration) and material treatment, the combinations of which are infinite. In this context, the radiation or RCS can be described by

$$\mathbf{S} = \mathbf{S}[\boldsymbol{\theta}, f, p, g(\boldsymbol{\alpha})], \tag{21}$$

for the independent variables

$\boldsymbol{\theta} \equiv$ aspect angle vector
$f \equiv$ frequency
$p \equiv$ polarization
$g \equiv$ geometry
$\boldsymbol{\alpha} \equiv$ parameter vector

where the parameter vector is of arbitrary dimension, dependent on the particular shape (configuration) and material treatment under investigation. The result, $\mathbf{S}$, may be taken to represent scatter, radiation, field unknowns, insertion/reflection loss or any of a number of electromagnetic "products" and itself may be *highly* sensitive to changes in certain parameters. In fact, a certain degree of sensitivity is desired in order to perform an effective optimization as alluded to in Section 2.2.

The objective function is typically taken to be more than a single $\mathbf{S}$ result. For instance, optimization could be wide-band in frequency: one could seek the optimal geometry as a

function of multiple frequencies, $f_1, f_2, \ldots f_N$. In that case, the objective (i.e., cost function) is chosen according to

$$J(\boldsymbol{\alpha}) = \left\| \mathbf{S}(\boldsymbol{\alpha}) - \mathbf{S}_{obj} \right\|_f^{\infty}, \tag{22}$$

for $\mathbf{S}(\boldsymbol{\alpha}) = \left[S(f_1, g(\boldsymbol{\alpha})), S(f_2, g(\boldsymbol{\alpha})), \ldots, S(f_N, g(\boldsymbol{\alpha})) \right]^T$, some objective value $\mathbf{S}_{obj}$, and $\|\bullet\|_f^{\infty}$ the infinity-norm over the frequency span, with remaining independent variables assumed fixed. The infinity-norm is chosen so that the optimization over the band consistently forces $\mathbf{S}$ to the objective; any excursion (at any point) about the objective penalizes the solution. As is typical, the optimum parametric vector is sought such that

$$\boldsymbol{\alpha}_{opt} = \underset{\boldsymbol{\alpha}}{\operatorname{argmin}} \left[J(\boldsymbol{\alpha}) \right]. \tag{23}$$

The field of signal processing is rich with the history of parametric estimation and optimization of systems associated with on- and off-line signal estimation. Much of that is predicated on the idea that a signal is present in noise or clutter to some degree and a model is available for fitting the signal to, or a covariance matrix can be used to enhance the estimate of the signal. Many nonparametric approaches utilize an eigendecomposition or singular value decomposition in order to understand the true nature of the signal or system, and the sensitivity to certain changes in the system (e.g., condition). These are powerful tools available to aid the understanding of complex signal environments so that researchers can better estimate features of interest.

In contrast, the environment in which this work takes place is entirely deterministic with respect to the prediction tool itself. However, it is just as true for the systems in electromagnetic predictions as it is for the systems in signal processing, that

nonparametric decompositions of the system can provide significant insights into the nature of system behavior. In the sense that an optimization which modifies that behavior according to some objective is sought, information present in the decomposition may be used to guide an optimization.

To this point, a reasonable existing (and validated) prediction code has been determined upon which to base the remainder of the work. The composition and structure of the associated matrix system has been discussed in Section 2.2. The work will continually refer back to the basic FEMA-BRICK system *viz.* Equation (13) as the heart of the optimization discussion proceeds. A wideband representation of this system that allows for modification of associated eigenvalues toward a particular objective will be given.

Contained in Appendix A is a description of some early work based on standard "global" (or gradient-free, statistical) optimization approaches. The two approaches evaluated under this effort were Genetic Algorithms (GA) and Simulated Annealing (SA). This small study showed that while these approaches are reasonable for cases involving a small number of parameters, they quickly become unreasonable when the number of parameters passes a certain point. The particular problem chosen for this dissertation topic is one such case. This was not an exhaustive test of options available via these two approaches. There are always potential ways to squeeze more out of the basic algorithm (GA or SA). However, it was shown that for this particular problem cast as-is, neither approach is readily applicable, further highlighting the need for an improved approach discussed next.

CHAPTER 3 LINEAR SYSTEM OPTIMIZATION APPROACH

While the general optimization techniques comprising this dissertation (and this chapter) are applicable to any electromagnetic system in principle, specific applications will always require an intimate knowledge of the physical geometry and material decomposition as it relates to the system. The previous chapters have served to set up the construct for the use of the FEMA-BRICK code "engine" to solve this particular application of a patch antenna over a textured substrate. The reader is asked to keep in mind that the techniques discussed in this chapter are applicable to other types of systems. Broad applicability is non-trivial, however, as will be shown. This is primarily true because of the very specific nature of electromagnetic systems.

3.1 Matrix Structure and Exploitation

As is typical of electromagnetic systems, the FE-BI system matrix utilized within FEMA-BRICK is complex symmetric (block Toeplitz). The total FE-BI system matrix for a given frequency, geometry, and material profile goes according to

$$\mathbf{R} = \mathbf{A}^{(1)} + \mathbf{A}^{(2)} + \mathbf{G}^{(1)} + \mathbf{G}^{(2)}. \tag{24}$$

Defining

$$\mathbf{e} = \begin{bmatrix} \mathbf{E}_j^{\text{bi}} \\ \mathbf{E}_j^{\text{fe}} \end{bmatrix} \text{ and } \mathbf{f} = \begin{bmatrix} \tilde{\mathbf{f}}_i^{\text{ext}} \\ \mathbf{f}_i^{\text{int}} \end{bmatrix}, \tag{25}$$

it is clear that $\mathbf{e} = \mathbf{R}^{-1}\mathbf{f}$ solves the system for a given frequency, geometry, and material profile. This is effectively what the FEMA-BRICK code accomplishes, but without explicitly forming the system matrix in core memory (the system is solved via the biconjugate gradient technique).

There are two fundamental aspects to the optimization problem under consideration: 1) control of the optimization is accomplished by adjusting the dielectric permittivity only ($\mathbf{A}^{(2)}\boldsymbol{\varepsilon} = \mathbf{A}^{(2)}(\ )$), and 2) a wideband optimum solution is needed. The matrix structure associated with each of these issues is discussed in the next two sections.

3.1.1 Matrix Structure Dependence on Permittivity

The focus of this section is on $\mathbf{A}\boldsymbol{\varepsilon}^{(2)}(\ )$. No other matrix components noted are affected by changes in the structure of material permittivity within the FE-BI context. As such, this component represents the only noted "control mechanism" to provide the optimum solution. Since this is the centerpiece of this research activity, it is necessary to clearly understand the development of the elements within this control matrix in order to provide a usable decomposition; this is covered in the sections that follow.

As previously mentioned, specific computation of individual brick contributions involves a volume integral about the brick itself according to

$$\mathbf{A}_{ij}^{(2)}\left(\left[\varepsilon_r\right]_n\right) = -k_0^2 \int_V \left[\left[\varepsilon_r\right]_n \mathbf{W}_i \cdot \mathbf{W}_j\right] dV\,, \tag{26}$$

highlighting the fact that the FE contributions are taken over a textured material substrate structure: each brick within the 3-D lattice must be indexed by n ($\boldsymbol{\varepsilon} = \left[\varepsilon_r\right]_n$) to describe the total geometry.

Computations within the FEMA-BRICK code begin with the linear edge-based expansion functions given by

$$
\begin{aligned}
\mathbf{W}_1^e &= \hat{\mathbf{x}}\left(-y + y_c^e + h_y^e/2\right)\left(-z + z_c^e + h_z^e/2\right)\Big/ h_y^e h_z^e \\
\mathbf{W}_2^e &= \hat{\mathbf{x}}\left(y - y_c^e + h_y^e/2\right)\left(-z + z_c^e + h_z^e/2\right)\Big/ h_y^e h_z^e \\
\mathbf{W}_3^e &= \hat{\mathbf{x}}\left(-y + y_c^e + h_y^e/2\right)\left(z - z_c^e + h_z^e/2\right)\Big/ h_y^e h_z^e \\
\mathbf{W}_4^e &= \hat{\mathbf{x}}\left(y - y_c^e + h_y^e/2\right)\left(z - z_c^e + h_z^e/2\right)\Big/ h_y^e h_z^e \\
\mathbf{W}_5^e &= \hat{\mathbf{y}}\left(-x + x_c^e + h_x^e/2\right)\left(-z + z_c^e + h_z^e/2\right)\Big/ h_x^e h_z^e \\
\mathbf{W}_6^e &= \hat{\mathbf{y}}\left(-x + x_c^e + h_x^e/2\right)\left(z - z_c^e + h_z^e/2\right)\Big/ h_x^e h_z^e \\
\mathbf{W}_7^e &= \hat{\mathbf{y}}\left(x - x_c^e + h_x^e/2\right)\left(-z + z_c^e + h_z^e/2\right)\Big/ h_x^e h_z^e \\
\mathbf{W}_8^e &= \hat{\mathbf{y}}\left(x - x_c^e + h_x^e/2\right)\left(z - z_c^e + h_z^e/2\right)\Big/ h_x^e h_z^e \\
\mathbf{W}_9^e &= \hat{\mathbf{z}}\left(-x + x_c^e + h_x^e/2\right)\left(-y + y_c^e + h_y^e/2\right)\Big/ h_x^e h_y^e \\
\mathbf{W}_{10}^e &= \hat{\mathbf{z}}\left(x - x_c^e + h_x^e/2\right)\left(-y + y_c^e + h_y^e/2\right)\Big/ h_x^e h_y^e \\
\mathbf{W}_{11}^e &= \hat{\mathbf{z}}\left(-x + x_c^e + h_x^e/2\right)\left(y - y_c^e + h_y^e/2\right)\Big/ h_x^e h_y^e \\
\mathbf{W}_{12}^e &= \hat{\mathbf{z}}\left(x - x_c^e + h_x^e/2\right)\left(y - y_c^e + h_y^e/2\right)\Big/ h_x^e h_y^e
\end{aligned}
$$

for the brick geometry element (e) as shown in Figure 3-1. With this construction, the field is represented *within* the brick by the 12 edge element unknowns according to

$$\mathbf{E}^e = \sum_{k=1}^{12} E_k^e \mathbf{W}_k^e \,. \tag{27}$$

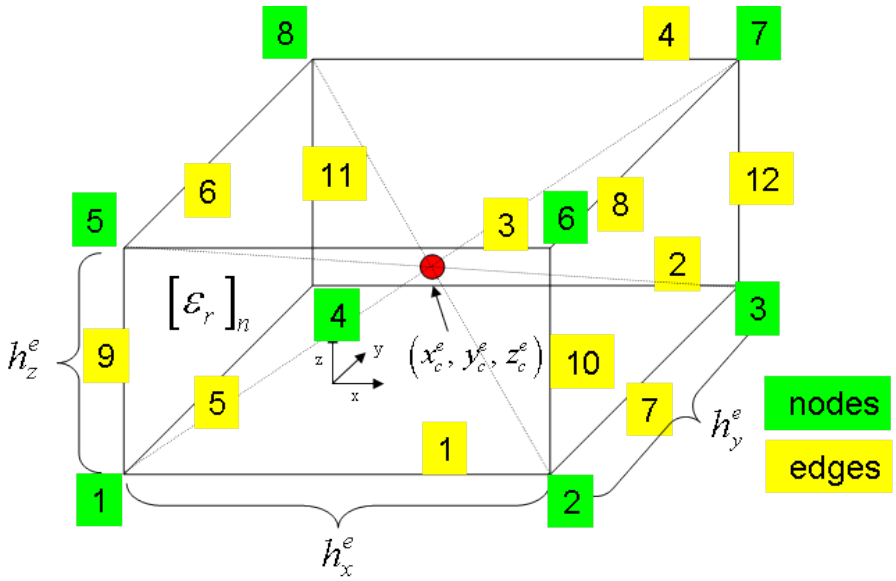

Figure 3-1. Brick Geometry within FEMA-BRICK

The entire geometry is constructed from these fundamental elements, such that a given edge-based unknown is derived from a combination of those brick material values surrounding it. Computation of entries within $\mathbf{A}_{\varepsilon}^{(2)}(\ )$ involves the superposition of all brick elements, where each brick element contribution is augmented according to

$$\mathbf{A}_{ij}^{(2)}\left(\left[\varepsilon_r\right]_n\right) \rightarrow \mathbf{A}_{ij}^{(2)}\left(\left[\varepsilon_r\right]_n\right) - k_0^2\left[\varepsilon_r\right]_n h_x^e h_y^e h_z^e \begin{bmatrix} \mathbf{L} & \mathbf{0} & \mathbf{0} \\ \mathbf{0} & \mathbf{L} & \mathbf{0} \\ \mathbf{0} & \mathbf{0} & \mathbf{L} \end{bmatrix}_{i'j'}, \tag{28}$$

where the $i, j,$ and i', j' terms associate the element system position with the global matrix structure (to be superimposed), and the symmetric matrix

$$\mathbf{L} = \begin{bmatrix} 1/9 & 1/18 & 1/18 & 1/36 \\ 1/18 & 1/9 & 1/36 & 1/18 \\ 1/18 & 1/36 & 1/9 & 1/18 \\ 1/36 & 1/18 & 1/18 & 1/9 \end{bmatrix}.$$

The values within the matrix are evident by noting that

$$\begin{aligned}
&\frac{1}{a^2b^2}\int_{-a/2}^{a/2}\int_{-b/2}^{b/2}\left(\pm s+a/2\right)^2\left(\pm t+b/2\right)^2\,dsdt=\frac{ab}{9}\\
&\frac{1}{a^2b^2}\int_{-a/2}^{a/2}\int_{-b/2}^{b/2}\left(\mp s+a/2\right)\left(\pm s+a/2\right)\left(\pm t+b/2\right)^2\,dsdt=\frac{ab}{18}\\
&\frac{1}{a^2b^2}\int_{-a/2}^{a/2}\int_{-b/2}^{b/2}\left(\mp s+a/2\right)\left(\pm s+a/2\right)\left(\mp t+b/2\right)\left(\pm t+b/2\right)\,dsdt=\frac{ab}{36}
\end{aligned}, \qquad (29)$$

and observing the manner in which the linear edge-based element expansion functions are arranged.

Computing the contribution within $\mathbf{A}\tilde{\boldsymbol{\varepsilon}}^{(2)}(\ )$ to a given edge-based unknown therefore involves the sum of the contributions of the surrounding material bricks. The resultant matrix is clearly symmetric in structure and is extremely sparse. Typically, less than 1% of the terms in $\mathbf{A}\tilde{\boldsymbol{\varepsilon}}^{(2)}(\ )$ will be non-zero.

This symmetric matrix can be decomposed according to

$$\mathbf{A}\tilde{\boldsymbol{\varepsilon}}^{(2)}(\ )=\mathbf{LDL}^{T}, \qquad (30)$$

(as can any symmetric matrix) where $\mathbf{L}$ is a lower triangular matrix with unity diagonal, and $\mathbf{D}$ is a diagonal matrix. The algorithm which accomplishes this decomposition is $O(N^3)$ [29]. As described above, a given edge element unknown is affected by at most 4 bricks. It is straightforward to construct a geometric mapping between the physical material bricks and the locations within the global matrix structure (unknowns), thus weighting the element contributions appropriately. As will be shown, the geometric mapping is most strongly represented in $\mathbf{L}$, while the material value contributions are

most strongly represented in $\mathbf{D}$, such that $\mathbf{D} = \mathrm{diag}(d_i) \approx \mathbf{D}(\ )$. To observe this, note that for a particular realization of $\mathbf{A}^{(2)}(\ ) = \mathbf{LDL}^T$, a constant material adjustment and subsequent $\mathbf{LDL}^T$ decomposition will result in no change to $\mathbf{L}$, and a similar constant adjustment to $\mathbf{D}$ regardless of the initial $\boldsymbol{\varepsilon}$ profile. This approximation loses validity as the structure of the material profile increasingly deviates from the baseline, or if material transitions are not smooth.

Assuming that $\mathbf{D} = \mathrm{diag}(d_i) \approx \mathbf{D}(\ )$, a transformation matrix can be determined that gives the material profile weight update from a corresponding diagonal element $\mathbf{d} = [d_1, d_2, \ldots, d_N]^T$ update according to

$$\mathbf{w}_d = \mathbf{T}_\varepsilon \mathbf{w}_\varepsilon \quad \Leftrightarrow \quad \mathbf{w}_\varepsilon = \mathbf{T}_\varepsilon^+ \mathbf{w}_d \,, \tag{31}$$

where $\mathbf{w}_\varepsilon$ is a vector of weights applied to permittivity values in the cavity structure taken row by row in the material profile 2-D structure, $\mathbf{w}_d$ is the corresponding weighting applied to $\mathbf{d}$ (via Hadamard product), and $\mathbf{T}_\varepsilon^+ = \left(\mathbf{T}_\varepsilon^T \mathbf{T}_\varepsilon\right)^{-1} \mathbf{T}_\varepsilon^T$ is simply the Moore-Penrose pseudo-inverse.

As a final remark, the Cholesky decomposition is given by

$$\mathbf{A}^{(2)}(\ ) = \mathbf{GG}^T, \tag{32}$$

for $\mathbf{G} = \mathbf{LD}^{1/2}$, but note that the $\mathbf{LDL}^T$ form is preferred for aforementioned reasons of electromagnetic mechanism (geometry and material) separability.

3.1.2 Wideband Matrix Structure

Since the goal is to produce a wideband optimization for (a) particular component(s) of the **e** vector, it is prudent to examine the frequency dependence of the system matrix components.

Based on Equation (16), note the frequency dependencies for the FE matrices can be given by

$$\begin{aligned} \mathbf{A}^{(1)}(k) &= \mathbf{A}^{(1)}(k_0) \\ \mathbf{A}^{(2)}(k) &= \tilde{k}^2\ \mathbf{A}^{(2)}(k_0) \end{aligned}, \tag{33}$$

for the normalized frequency variable $\tilde{k} = k/k_0$, where k_0 is a reference frequency point within the band of interest (e.g., center frequency). Further, to first order, the frequency dependencies for the BI matrices can be approximated according to

$$\begin{aligned} \mathbf{G}^{(1)}(k) &\approx \tilde{k}^2\ \mathbf{G}^{(1)}(k_0) \\ \mathbf{G}^{(2)}(k) &\approx \mathbf{G}^{(2)}(k_0) \end{aligned}. \tag{34}$$

To see why this approximation is reasonable, consider the Taylor series expansion about the center frequency for the complex exponential term within the integrand for these two matrices. This is given by

$$\frac{e^{-jkR}}{R} \approx \frac{e^{-jk_0R}}{R}\left(1 - j(k-k_0)R - \frac{1}{2}(k-k_0)^2 R^2 + \ldots\right). \tag{35}$$

There are two things that lend validity to the first-order approximation of Equation (34). First, the values which dominate the resultant BI matrices are those for which $R \to 0$.

This is evidenced in Figure 3-2, where the self- and close-impedance terms (small R) are highlighted. Note that the values are shown in dB ($20\log_{10}|-|$) to highlight the differences in the coefficients associated with larger R.

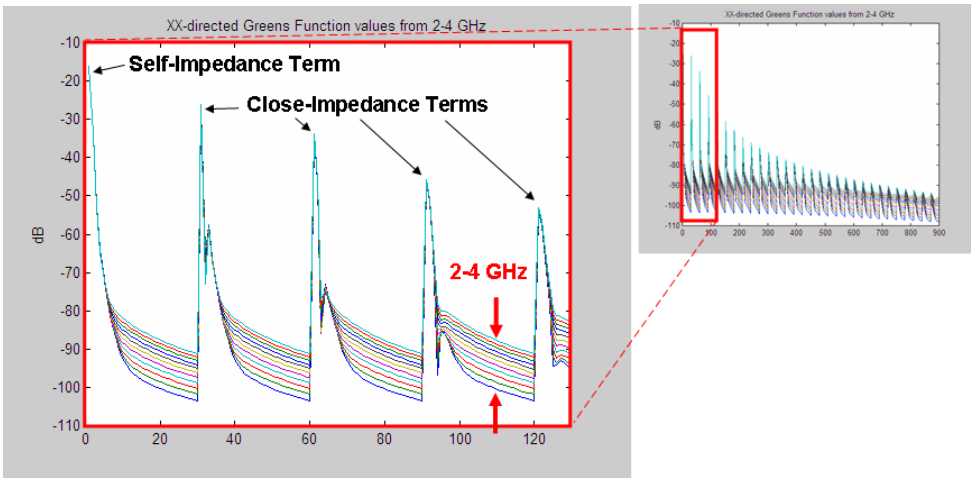

Figure 3-2. Typical Values within BI Matrices over a Wide Band (2-4 GHz)

Obviously, the second factor weighing favorably is that for $R \to 0$, the first term in the Taylor series is highly dominant, allowing for Equation (34). This provides a convenient linear relationship between the overall FE-BI system matrix versus frequency.

Support for this idea is available in the literature. The asymptotic waveform evaluation (AWE) technique was introduced as a means to speed-up solutions of matrix systems at frequencies (k) away from a particular reference frequency (k_0), by approximating the unknown surface current solutions via some numerical expansion. AWE was initially introduced using a Taylor series expansion, and was later improved upon via a Padé expansion [37, 38, 39, 40]. The latest work demonstrates that accurate approximations over very large fractional bandwidths [> 1.6 for L=6, M=6, see below for variable descriptions] are possible. The fact that Padé expansions provide enhanced accuracy is

readily seen by observing that poles and zeros are each well-modeled according to the representation

$$P_n\left(L/M\right)=\frac{\sum_{l=0}^{L}a_n^l\left(k-k_0\right)^l}{1+\sum_{m=1}^{M}b_n^m\left(k-k_0\right)^m}. \tag{36}$$

Since the basic electromagnetic problem consists of (perhaps, several) resonances at pole locations, such an expansion leads to a suitable broadband approximation from a knowledge of the solution (fields, radar scattering, radiation pattern, impedance, etc.) at a few frequency points. As an example, Erdemli, et. al. [37], determined the coefficients in the Padé expansion via Taylor and then directly computed the surface current using the expansion

$$\left\{I_n\left(k\right)\right\}_{N\times 1}=\left\{P_n\left(L/M\right)\right\}_{N\times 1}. \tag{37}$$

In general, solutions are examined for increasing orders of expansion. For illustration purposes, it is possible to keep only the first term and formulate the solution via eigendecomposition. The reasonableness of the approximation for this case follows.

As before, for any given frequency,

$$\left\{\mathbf{A}^{(1)}\left(k\right)+\mathbf{A}^{(2)}\left(k\right)+\mathbf{G}^{(1)}\left(k\right)+\mathbf{G}^{(2)}\left(k\right)\right\}\mathbf{e}\left(k\right)=\mathbf{f}\left(k\right). \tag{38}$$

Utilizing the approximation of Equations (33) and (34), rewrite (38) as

$$\left\{\mathbf{A}^{(1)}\left(k_0\right)+\tilde{k}^2\ \mathbf{A}^{(2)}\left(k_0\right)+\tilde{k}^2\ \mathbf{G}^{(1)}\left(k_0\right)+\mathbf{G}^{(2)}\left(k_0\right)\right\}\mathbf{e}\left(k\right)\approx\mathbf{f}\left(k\right), \tag{39}$$

or equivalently

$$\mathbf{C}_{\mu}(k_0) + \mathbf{E}_{\varepsilon}(k_0)\,\mathbf{F}^{2} \approx \quad , \tag{40}$$

where

$$\mathbf{C}_{\mu}(k_0) \equiv \mathbf{A}^{(1)}(k_0) + \mathbf{G}^{(2)}(k_0)$$
$$\mathbf{C}_{\varepsilon}(k_0) \equiv \mathbf{A}^{(2)}(k_0) + \mathbf{G}^{(1)}(k_0)$$
$$\mathbf{K} \equiv \mathrm{diag}\left(\left[\tilde{k}_1, \tilde{k}_2, \ldots, \tilde{k}_F\right]\right)$$

and

$$\mathbf{E} \equiv \left[\mathbf{e}(k_1), \mathbf{e}(k_2), \ldots, \mathbf{e}(k_F)\right]$$
$$\mathbf{F} \equiv \left[\mathbf{f}(k_1), \mathbf{f}(k_2), \ldots, \mathbf{f}(k_F)\right]^{'}$$

where F is the total number of frequency points. Define $\mathbf{C}_{\mu}$ as the constituent matrix whose properties are primarily affected by substrate permeability (henceforth assumed to be unity as in free space), and $\mathbf{C}_{\varepsilon}$ as the constituent matrix whose properties are primarily affected by substrate permittivity (which will be adjusted). The optimization approach is developed as generally as possible, despite the assumption of free space permeability.

To test the approximation, FEMA-BRICK is exercised to compute all matrix elements above, plotting the residual, using the example geometry shown in Figure 3-3. The error relative to the associated field (frequency-by-frequency) is predominantly on the order of 1-2% as shown in Figure 3-4.

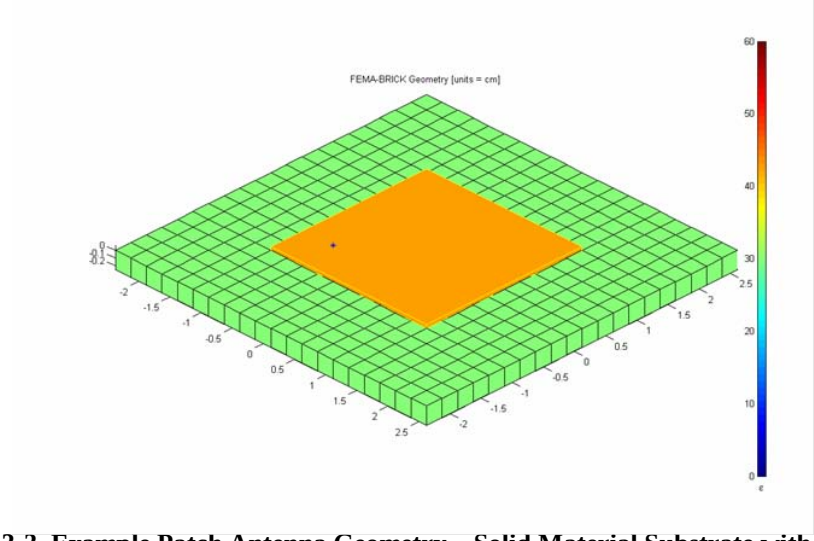

Figure 3-3. Example Patch Antenna Geometry – Solid Material Substrate with $\varepsilon_r = 30$

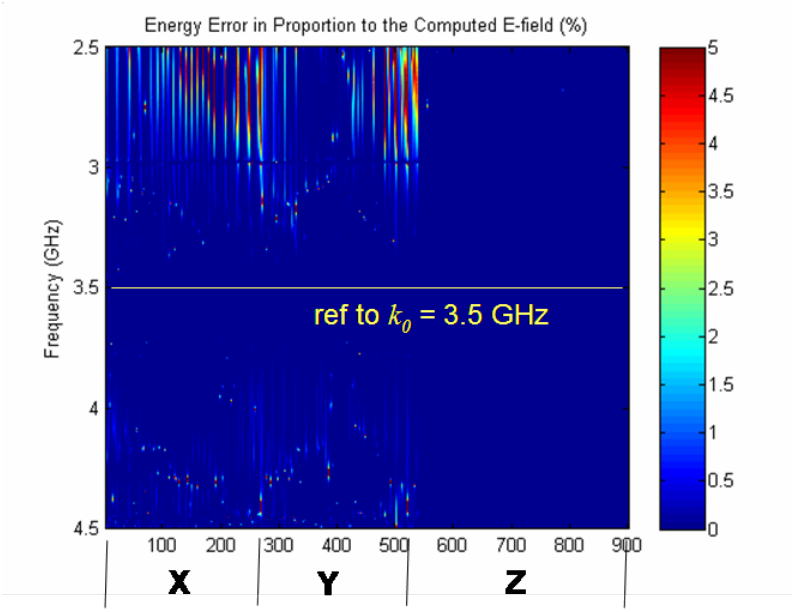

$$\mathbf{error} = \frac{\left|\left(\mathbf{A}^{(2)} + \mathbf{G}^{(1)}\right)\mathbf{E}\,\mathbf{K}^2 + \left(\mathbf{A}^{(1)} + \mathbf{G}^{(2)}\right)\mathbf{E} - \mathbf{F}\right|^2}{\left|\mathbf{E}\right|^2} \times 100\%$$

Figure 3-4. Approximation Error about the Center Frequency of 3.5 GHz

The relative error is expected to depend on the choice of reference frequency. Two such examples are shown in Figure 3-5, where clearly the error is minimized in the region of the reference point. Note that focusing on the particular regions of large error (e.g., $k_0 = 3\,\text{GHz}$) tends to reduce the average error over the entire band.

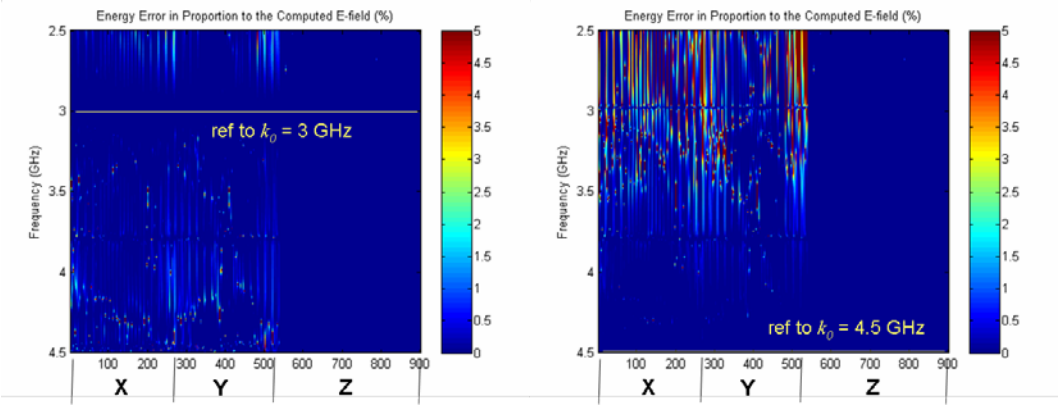

Figure 3-5. Approximation Error about 3 GHz (left) and 4.5 GHz (right)

3.2 System Condition Issues

The FE-BI system as defined above is well-conditioned provided adequate attention is given to the construction of the geometry. Consider the example of three identical geometries that have been constructed differently by a factor. The geometries are shown in Figure 3-6, where one has been subdivided into 10 segments per edge, the next has been subdivided into 20 segments per edge, and the third has been subdivided into 30 segments per edge. The substrate is of size 4.0 cm × 4.0 cm × 0.1 cm and has a value of $\varepsilon_r = 100 - j0.15$. The Z-directed E-field at the probe location is investigated from 1-2 GHz.

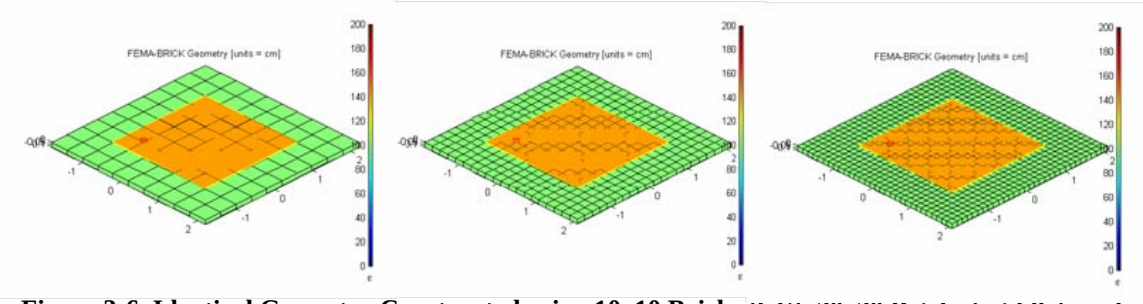

Figure 3-6. Identical Geometry Constructed using 10x10 Bricks (left), 20x20 Bricks (middle), and 30x30 Bricks (right)

The respective field calculated at the probe location for each case is shown in Figure 3-7. The high-density geometry is the most accurate. Observe that lower-density solutions are converging towards the high-density solution, as expected.

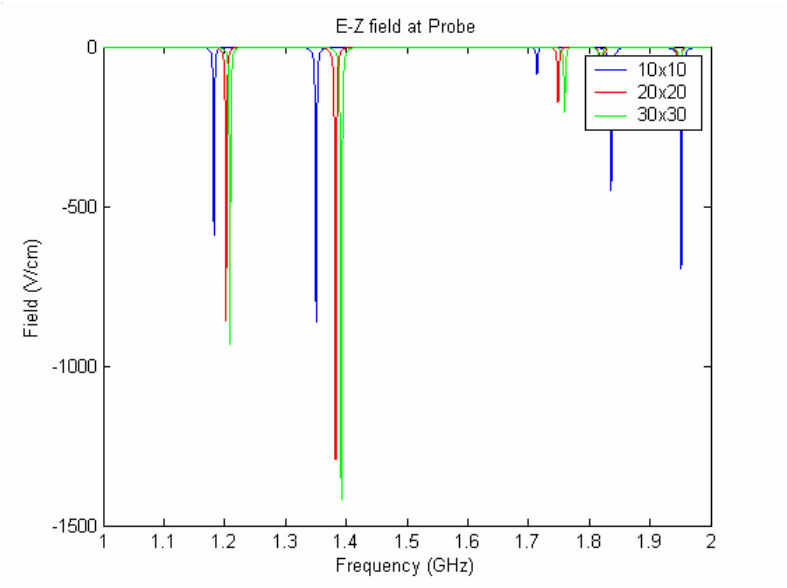

Figure 3-7. Probe Location E-field Unkown (real part) for 10x10 Bricks (blue), 20x20 Bricks (red), and 30x30 Bricks (green) Shows Convergence of Solution for $\varepsilon_r = 100 - j0.15$

If for these identical geometries the value of the solid substrate permittivity is increased to $\varepsilon_r = 200 - j0.3$, then $\varepsilon_r = 500 - j0.75$, the results shown in Figure 3-8 are obtained. There is an increased tendancy in these examples for the low-density mesh solution to show divergence from the high-density mesh solution.

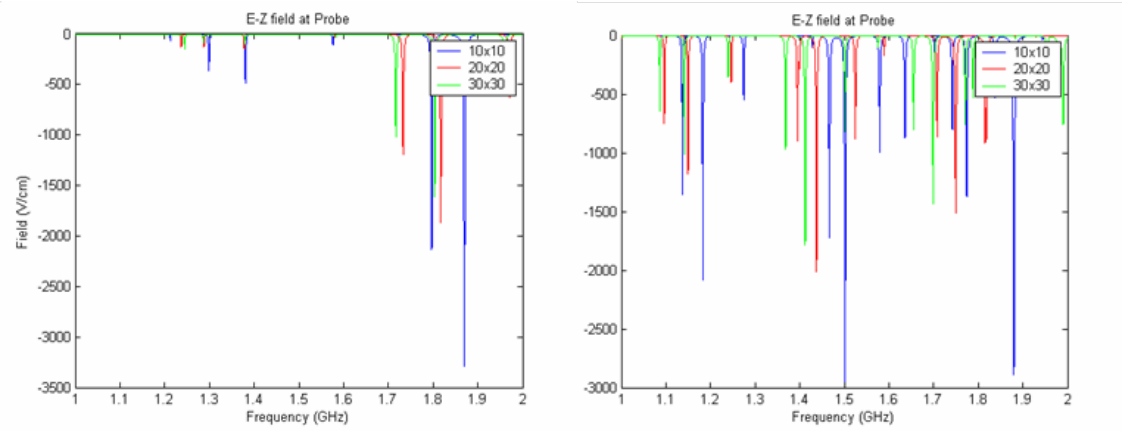

Figure 3-8. Probe Location E-field Unkown (real part) for Various Brick Meshes and Increasing Permittivity [$\varepsilon_r = 200 - j0.3$ (left) and $\varepsilon_r = 500 - j0.75$ (right)]

The differences in these predictions help to illustrate the sensitivity of the solution space to geometric meshing and material perturbation. In the context of the electromagnetic system, the following table is obtained by examining the computed condition of the matrix $\mathbf{R} = \mathbf{A}^{(1)}(k_0) + \mathbf{A}^{(2)}(k_0) + \mathbf{G}^{(1)}(k_0) + \mathbf{G}^{(2)}(k_0)$ in all cases.

Table 3-1. System Matrix Condition versus Material Permittivity and Mesh

Permittivity / Mesh	10 × 10	20 × 20	30 × 30
100 – j 0.15	101	168	285
200 – j 0.2	113	119	174
500 – j 0.75	2125	173	3418

The first two cases are reasonable condition numbers for the solution of the FE-BI system. The last case is beginning to approach erratic and problematic condition numbers. The purpose in highlighting these cases is to show that attention must be given to the maximum allowable material permittivity in a textured material solution. A standard rule of thumb for discretization of a geometry is that the segments (cells) should be on the order of $\lambda_g/10$, for the guide wavelength given by $\lambda_g = \lambda/\sqrt{\varepsilon_r}$. As material permittivity increases, physical cell size must decrease. This is a key solution space limitation.

3.3 Total Least Squares Optimization of the Electromagnetic System

An early attempt at optimization of the matrix system centered on the use of a constrained Total Least Squares (TLS) approach. This particular optimization attempted to make use of the frequency dependence of the finite element matrices only, such that the system was given by

$$\left\{\mathbf{A}^{(1)}\left(k_0\right)+\tilde{k}^2\,\mathbf{A}^{(2)}\left(k_0\right)+\mathbf{G}\left(k\right)\right\}\mathbf{e}\left(k\right)=\mathbf{f}\left(k\right), \tag{41}$$

without approximation. Control for optimization is given exclusively by $\mathbf{A}^{(2)}\left(k_0;\ \right)$ and a simplified means to update via a diagonal weight matrix, $\mathbf{W}$, is assumed. Defining the update according to

$$\mathbf{A}^{(2)}\left(k_0;\mathbf{W}_{t+1}\right)= \qquad \mathbf{A}^{(2)}\left(k_0;\ _t\right), \tag{42}$$

and constraining the field unknowns associated with the feed,

$$\tilde{k}^2\,\mathbf{W}\mathbf{A}^{(2)}(k_0;\ _t)\,\mathbf{f}(k) = (k) - \left\{ {}^{(1)}(k_0) + \mathbf{e}\ (k)\right\}\ (k) \\ = \mathbf{d}(k) \qquad (43)$$

is found. If the l.h.s. to the objective is constrained at *n*, where *n* defines the locations in the unknown vector associated with the feed, then

$$\mathbf{W}_u\left[\mathbf{A}^{(2)}(k_0;\ _t)\right]_u\ _u(k) = \tilde{k}^{-2}\mathbf{W}\ (k) - \ _n\left[\ ^{(2)}(k_0;\ _t)\right]_n\ _n(k) \\ = \mathbf{g}(k) \qquad (44)$$

where

$$\mathbf{W}_u = diag\left(\left[w_1, w_2, \ldots, w_{n-1}, w_{n+1}, w_N\right]\right)$$
$$\mathbf{W}_n = diag\left(\left[w_n\right]\right)$$
$$\mathbf{e}(k) = \left[\mathbf{e}_u(k)^T, \mathbf{e}_n(k)^T\right]^T$$
$$\mathbf{A}^{(2)}(k_0;\ _t) = \left[\left[\ ^{(2)}(k_0;\ _t)\right]_u, \left[\ ^{(2)}(k_0;\ _t)\right]_n\right]$$

and the $[\ ]_n$ terms are associated with the constraint, while the $[\ ]_u$ terms are unconstrained. The precise form of the update weight matrix is functionally dependent on the geometry of the FE-BI solution, since the feed location must be assigned within the matrix, $\mathbf{A}^{(2)}(k_0;\ )$. Once the proper relationship is established between the system and the physical structure, a Total Least Squares (TLS) solution may be found.

Generally, the TLS approach is attractive in cases where "error" may exist in both the operator (FE-BI) and solution (excitation) matrices. The technique fundamentally works by finding the minimum common solution space between the "data" ($\left[\mathbf{A}^{(2)}(k_0;\ _t)\right]_u$) and

the "measurement" ($\mathbf{g}(k)$). Each solution space is allowed to perturb to find the minimum error between both. It is an exact solution to the system when the error (or deviation) matrices are included. It can be proven that under certain (enforceable) conditions, the TLS solution exists and is unique, and this is very well explained in Golub and Van Loan [29]. An explanation of the constrained solution approach utilized for this work is given in Appendix B. In this case, however, the problem of encouraging a solution with diminishing error (convergence toward a solution) is confronted, and one must question whether this is possible. One limitation at the outset is that a value on the r.h.s. must be assumed in order to form an update. The solution proceeds by solving for

$$\left\{\left[\mathbf{A}\boldsymbol{\varepsilon}^{(2)}\left(k_0;\ _t\right)\right]_u + \Delta\left[\ \boldsymbol{\varepsilon}^{(2)}\left(k_0;\ \mathbf{e}_t\right)\right]_u\right\}\left\{\ _u(k) + \Delta\ _u(k)\right\} = \ (k) + \Delta\ (k), \tag{45}$$

via the TLS approach. The weight update is then solved for by equating

$$\mathbf{W}_u\left[\boldsymbol{\varepsilon}\mathbf{A}^{(2)}\left(k_0;\mathbf{A}_t\right)\right]_u = \left[\boldsymbol{\varepsilon}^{\ (2)}\left(k_0;\ _t\right)\mathbf{A}\right]_u + \Delta\left[\boldsymbol{\varepsilon}^{\ (2)}\left(k_0;\ _t\right)\right]_u. \tag{46}$$

The TLS approach determines the deviation matrices by minimizing

$$\left\| \mathbf{M}_r\left[\boldsymbol{\varepsilon}\Delta\left[\mathbf{A}^{(2)}\left(k_0;\ _t\right)\mathbf{M}\right]_u, \Delta\ (k)\right]\ _c\right\|_F, \tag{47}$$

where $\|\bullet\|_F$ is the Frobenius norm, and the **M** matrices are diagonal and represent row-wise and column-wise solution space norm matrices, respectively. Finding this minimum norm solution is accomplished via Singular Value Decomposition (SVD). It was only necessary to compute a few of the smallest singular values, so solution times were not prohibitive. Generally, both solution space norm matrices were chosen such that

det(**M**)=1 and the constrained matrix elements, *n*, were weighted more heavily than the remaining elements, thus encouraging convergence toward the constraint.

Narrowband optimizations were performed with only modest success using this approach. Again, for the case of the original patch antenna geometry, repeated for convenience below in Figure 3-9, a narrowband optimization was performed.

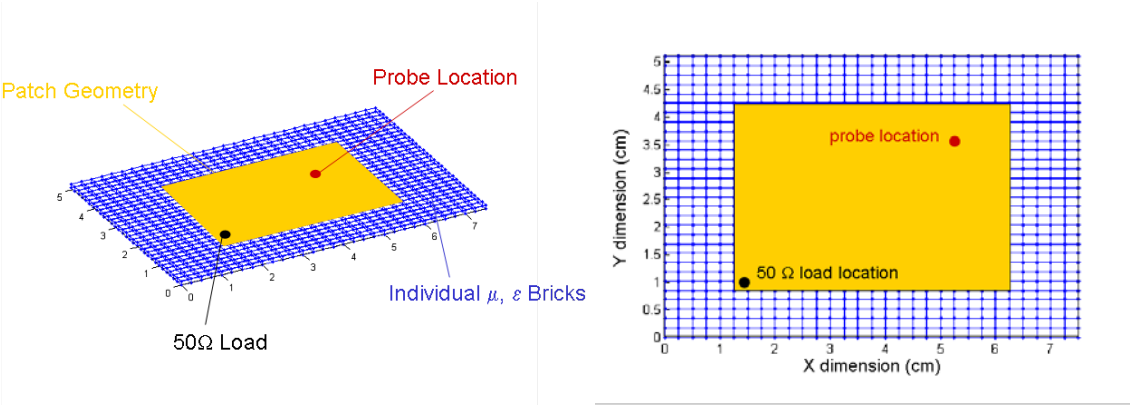

Figure 3-9. Patch Antenna Configuration Utilized for TLS Optimization Tests

A typical optimization run is shown in Figure 3-10, where a sharp truncation of material (to air) in the material profile to the left is observed, and a somewhat inconsistent approach toward the objective in the iteration on the right is shown. Indeed, the typical TLS optimization run did not actually achieve the objective, though it did approach it.

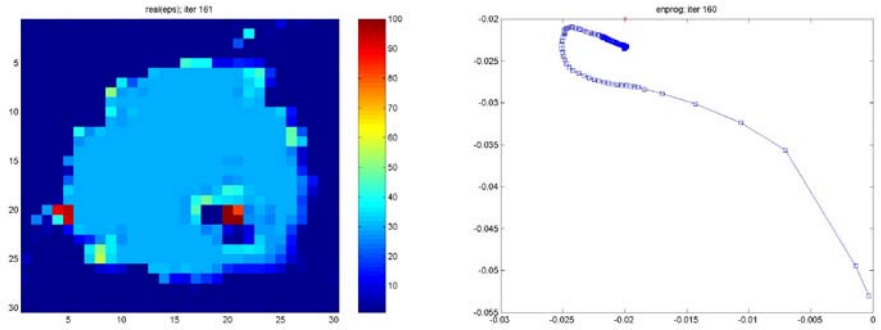

Figure 3-10. Patch Antenna TLS Optimization Result; Material Profile (left), Iteration (right)

A significant issue associated with TLS optimization as it was implemented here was that the structure associated with the deviation "data matrix" in question ($\Delta\left[\mathbf{A}\boldsymbol{\varepsilon}^{(2)}\left(k_0;\ _t\right)\right]_u$), for which the update weight was extracted, differed in form from the original data matrix ($\left[\mathbf{A}\boldsymbol{\varepsilon}^{(2)}\left(k_0;\ _t\right)\right]_u$). This is not surprising, since the deviation matrix is formed from a single outer product of eigenvectors (based on the most insignificant eigenvalue), and the form of the original data matrix is sparse and largely diagonal (see Figure 2-8 on page 30). This caused the update weighting to be very slow in converging.

CHAPTER 4 NARROWBAND SYSTEM OPTIMIZATION

The constrained TLS approach served to highlight a number of useful qualities associated with the eigendecomposition of electromagnetic systems such as FE-BI; most significantly, the manner in which update weights should be applied. It led to the observed need to consider *all* terms in the eigendecomposition. An approach that could effectively capture updates across the spectrum of weights available by material texturing held much more promise than one based on only one singular value.

This chapter introduces the manner in which the eigendecomposition of an electromagnetic system may be used to guide an optimization process. This was first pursued as a narrowband optimization only, and offered some particular interesting insights into system behavior, allowing for a basic iterative optimization.

4.1 Narrowband System Matrix Eigendecomposition

As presented in Section 3.1, the FE-BI system matrix may be given by

$$\mathbf{R} = \mathbf{A}^{(1)} + \mathbf{A}^{(2)} + \mathbf{G}^{(1)} + \mathbf{G}^{(2)}, \tag{48}$$

where $\mathbf{A}^{(2)}\boldsymbol{\varepsilon} = \mathbf{A}^{(2)}(\ )$ is the "control" sub-matrix: the only matrix adjusted via textured material for optimization. The eigendecomposition may be written as

$$\mathbf{R} = \mathbf{X}\boldsymbol{\Lambda}\mathbf{X}^{-1}, \tag{49}$$

where $\boldsymbol{\Lambda} = \mathrm{diag}(\lambda_i)$ is the eigenvalue matrix, and $\mathbf{X}$ contains the associated eigenvectors. As such, the system solution is given as

$$\mathbf{e} = \mathbf{X}\boldsymbol{\Lambda}^{-1}\mathbf{X}^{-1}\mathbf{f}, \tag{50}$$

where $\mathbf{e}$ is the narrowband edge-based E-field unknown vector and $\mathbf{f}$ is the excitation. A particular objective value is determined based on one or more element(s) of $\mathbf{e} = [e_1, e_2, \ldots, e_N]^T$. If the n^{th} element is chosen to have as its objective the value $e_{n,obj}$, the constraint equation

$$e_{n,obj} = \mathbf{x}_n^T\boldsymbol{\Lambda}^{-1}\boldsymbol{\beta}, \tag{51}$$

is found where $\mathbf{X} = [\mathbf{x}_1, \mathbf{x}_2, \ldots, \mathbf{x}_N]^T$ and $\boldsymbol{\beta} = \mathbf{X}^{-1}\mathbf{f}$. This particular constraint equation can be further simplified by noting that

$$\mathbf{x}_n^T\boldsymbol{\Lambda}^{-1}\boldsymbol{\beta} = \boldsymbol{\lambda}^{-T}(\mathbf{x}_n \odot \boldsymbol{\beta}) = e_{n,obj}, \tag{52}$$

where $\odot$ is the point-wise (Hadamard) product and $\boldsymbol{\lambda}^{-T} = [\lambda_1^{-1}, \lambda_2^{-1}, \ldots, \lambda_N^{-1}]$. Since the excitation vector ($\mathbf{f}$) and the eigendecomposition is uniquely defined for a given system, this form defines one constraint for the optimum solution given by $\boldsymbol{\lambda}_{opt}$. It may be treated as approximate if it is difficult to achieve the desired objective due to other constraints.

Generally, it is possible that a metric could be established based on more than one element of $\mathbf{e}$. Through a simple extension of Equation (52),

$$\left[e_{n_1,obj}, e_{n_2,obj}, \ldots, e_{n_N,obj} \right] = \boldsymbol{\lambda}^{-T} \left(\left[\mathbf{x}_{n_1} \odot \boldsymbol{\beta}, \mathbf{x}_{n_2} \odot \boldsymbol{\beta}, \ldots, \mathbf{x}_{n_N} \odot \boldsymbol{\beta} \right] \right), \tag{53}$$

is given. Note that the single eigenvalue vector controls all objective values. In order to drive a particular optimization, the individual objective values may be combined to form a single-valued metric (e.g., minimum L_2 norm).

4.2 Solution for Constant Material Adjustment Only

From Equations (30) and (31) in Section 3.1, note that if a constant material change is introduced (all element permittivity values similarly changed) according to some scale factor, then a relationship between the eigenvalue vector ($\boldsymbol{\lambda}$) and the material update vector ($\mathbf{d}$) is immediately provided. Such a constant material update factor serves as an example to illustrate the main points of the optimization development to follow.

The system to be solved is constructed in such a way as to guide the nature of the anticipated matrix deviations. Under the simple constant material change criterion, observe that

$$\mathbf{X}\left[\boldsymbol{\lambda} + \operatorname{diag}(\Delta\boldsymbol{\lambda})\right]\mathbf{L}^{-1} = \left[\mathbf{d} + \operatorname{diag}(a_0)\right]\mathbf{R}^{T} + \quad , \tag{54}$$

making

$$\begin{aligned} \mathbf{X}\left[\boldsymbol{\lambda} + \operatorname{diag}(\Delta\boldsymbol{\lambda})\right]\mathbf{L}^{-1} &= \left[\mathbf{d} + \operatorname{diag}(a_0)\right]^{T} \\ &= a_0\, \mathbf{A}\boldsymbol{\varepsilon}^{(2)}(\quad) \end{aligned} \quad , \tag{55}$$

where a_0 is a constant and $\Delta\boldsymbol{\lambda}$ represents a deviation to the eigenvalue vector commensurate with a constant material adjustment factor, $a_0 + 1$. For practical material

updates, enforce $a_0 \in \{\mathbb{R}; a_0 > -1\}$, since the overall material adjustment factor can not be negative and a low-loss optimization result is desired. The diagonal form of the eigenvector deviation may thus be given by

$$\Delta\boldsymbol{\lambda} \approx a_0 \, \Delta\boldsymbol{\lambda}_0 , \tag{56}$$

defining

$$\Delta\boldsymbol{\lambda}_0 = \mathrm{diag}\left(\mathbf{X}^{-1}\mathbf{A}^{(2)}\left(\boldsymbol{\varepsilon}\right)\mathbf{X}\right). \tag{57}$$

Equation (56) is approximate in the sense that the result of the matrix product $\mathbf{X}^{-1}\mathbf{A}^{(2)}\left(\boldsymbol{\varepsilon}\right)\mathbf{X}$ is diagonally dominant, but not perfectly diagonal. An example of this behavior is shown in Figure 4-1 below.

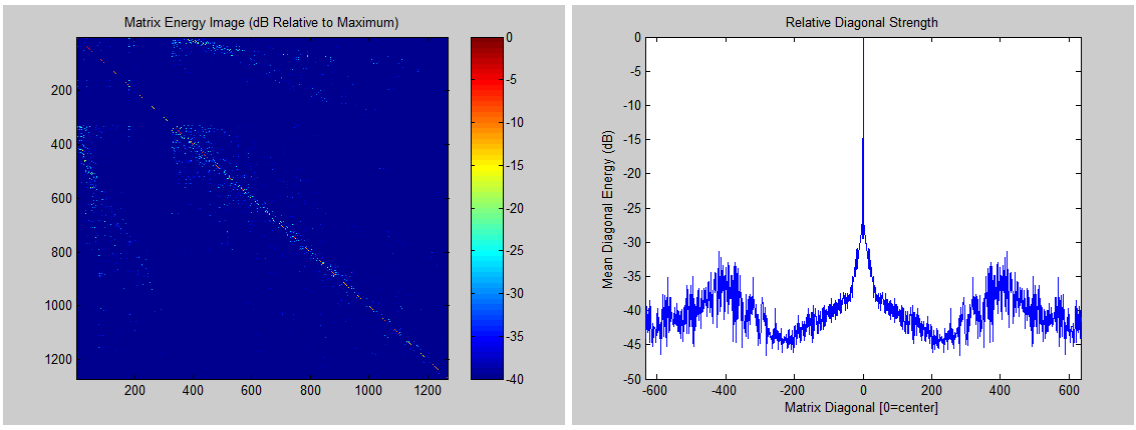

Figure 4-1. Typical Structure of Diagonally Dominant $\mathbf{X}^{-1}\mathbf{A}^{(2)}\left(\boldsymbol{\varepsilon}\right)\mathbf{X}$ (left) and Relative Diagonal Energy (right)

This is reasonable behavior to expect since the matrix $\mathbf{X}^{-1}\mathbf{R}\mathbf{X}$ *is* strictly diagonal and $\mathbf{A}^{(2)}\left(\boldsymbol{\varepsilon}\right)$ is one component of $\mathbf{R}$. As an aside, it is worthwhile to note that although $\mathbf{R}$ is

symmetric, it is not normal (i.e., $\mathbf{R}\mathbf{R}^H \neq \mathbf{R}^H\mathbf{R}$). For the above example, the departure from normality [29] is approximately 2×10^{-4} as given by

$$\Delta^2\left(\mathbf{R}\right) = \left\|\mathbf{R}\right\|_F^2 - \sum_i \left|\lambda_i\right|^2 . \tag{58}$$

Normality speaks to the degree with which a matrix is orthogonal. Orthogonality encourages changes in one eigenvalue to be independent from changes in the others.

The eigenvalue update equation for a constant material adjustment then goes according to

$$\boldsymbol{\lambda}^{-1}\left(a_0\right) \approx \left(\boldsymbol{\lambda} + a_0\,\Delta\boldsymbol{\lambda}_0\right)^{-1} = \boldsymbol{\lambda}^{-1} \odot \left(1 + a_0\,\Delta\boldsymbol{\lambda}_0 \odot \boldsymbol{\lambda}^{-1}\right)^{-1}, \tag{59}$$

where $\boldsymbol{\lambda}^{-1}\left(0\right) = \boldsymbol{\lambda}^{-1}$. Returning to (50),

$$\begin{aligned}
\mathbf{e}\left(a_0\right) &\approx \mathbf{X}\left[\operatorname{diag}\left(\boldsymbol{\lambda}^{-1} \odot \left(1 + a_0\,\Delta\boldsymbol{\lambda}_0 \odot \boldsymbol{\lambda}^{-1}\right)^{-1}\right)\right]\mathbf{X}^{-1}\mathbf{f} \\
&= \mathbf{X}\left[\operatorname{diag}\left(\boldsymbol{\lambda}^{-1}\right) - \operatorname{diag}\left(\frac{a_0\,\Delta\boldsymbol{\lambda}_0 \odot \boldsymbol{\lambda}^{-2}}{1 + a_0\,\Delta\boldsymbol{\lambda}_0 \odot \boldsymbol{\lambda}^{-1}}\right)\right]\mathbf{X}^{-1}\mathbf{f} \\
&= \mathbf{e}\left(0\right) - \mathbf{X}\left[\operatorname{diag}\left(\frac{a_0\,\Delta\boldsymbol{\lambda}_0 \odot \boldsymbol{\lambda}^{-2}}{1 + a_0\,\Delta\boldsymbol{\lambda}_0 \odot \boldsymbol{\lambda}^{-1}}\right)\right]\mathbf{X}^{-1}\mathbf{f}
\end{aligned} \tag{60}$$

is found, such that the deviation between the objective and the current state of the E-field may be given by

$$\Delta\mathbf{e}\left(a_0\right) \approx \mathbf{X}\left[\operatorname{diag}\left(\frac{a_0\,\Delta\boldsymbol{\lambda}_0 \odot \boldsymbol{\lambda}^{-2}}{1 + a_0\,\Delta\boldsymbol{\lambda}_0 \odot \boldsymbol{\lambda}^{-1}}\right)\right]\mathbf{X}^{-1}\mathbf{f} . \tag{61}$$

Additionally the derivative relative to the scale constant may be easily found as

$$\frac{\partial}{\partial a_0}\mathbf{E}\left(\hat{a}_0\right) \approx \mathbf{X}\left[\operatorname{diag}\left(\boldsymbol{\lambda}-\Delta_0 \odot \mathbf{X}\left(\mathbf{f}+a_0\,\Delta_0\right)^{-2}\right)\right]^{-1} . \tag{62}$$

The viability of this approach for solving constrained solutions is next examined by revisiting the objective Equation (52) under the condition of the update. This is accomplished by minimizing the objective function

$$\begin{aligned} J\left(a_0\right) &= \left|\left(\boldsymbol{\lambda}+a_0\Delta\boldsymbol{\lambda}_0\right)^{-T}\left(\mathbf{x}_n \odot \mathbf{b}\right)-e_{n,obj}\right|^2 \\ &= \left(\operatorname{Re}\left\{\left(\boldsymbol{\lambda}+a_0\Delta\boldsymbol{\lambda}_0\right)^{-T}\left(\mathbf{x}_n \odot \mathbf{b}\right)\right\}-\operatorname{Re}\left\{e_{n,obj}\right\}\right)^2 \\ &\quad +\left(\operatorname{Im}\left\{\left(\boldsymbol{\lambda}+a_0\Delta\boldsymbol{\lambda}_0\right)^{-T}\left(\mathbf{x}_n \odot \mathbf{b}\right)\right\}-\operatorname{Im}\left\{e_{n,obj}\right\}\right)^2 \end{aligned} . \tag{63}$$

The derivative may be given by

$$\begin{aligned} \frac{\partial}{\partial a_0}J\left(a_0\right) = &-2\left(\operatorname{Re}\left\{\left(\boldsymbol{\lambda}+a_0\Delta\boldsymbol{\lambda}_0\right)^{-T}\left(\mathbf{x}_n \odot \mathbf{b}\right)\right\}-\operatorname{Re}\left\{e_{n,obj}\right\}\right)\operatorname{Re}\left\{\left[\frac{\Delta\boldsymbol{\lambda}_0}{\left(\boldsymbol{\lambda}+a_0\Delta\boldsymbol{\lambda}_0\right)^2}\right]^T\left(\mathbf{x}_n \odot \mathbf{b}\right)\right\} \\ &-2\left(\operatorname{Im}\left\{\left(\boldsymbol{\lambda}+a_0\Delta\boldsymbol{\lambda}_0\right)^{-T}\left(\mathbf{x}_n \odot \mathbf{b}\right)\right\}-\operatorname{Im}\left\{e_{n,obj}\right\}\right)\operatorname{Im}\left\{\left[\frac{\Delta\boldsymbol{\lambda}_0}{\left(\boldsymbol{\lambda}+a_0\Delta\boldsymbol{\lambda}_0\right)^2}\right]^T\left(\mathbf{x}_n \odot \mathbf{b}\right)\right\} \end{aligned} . \tag{64}$$

Note that the derivative is zero when the objective itself is zero as should be expected for a function that approaches a minimum at zero gracefully. All conditions where

$$\left[\frac{\Delta\boldsymbol{\lambda}_0}{\left(\boldsymbol{\lambda}+a_0\Delta\boldsymbol{\lambda}_0\right)^2}\right]^T\left(\mathbf{x}_n \odot \mathbf{b}\right)=0, \tag{65}$$

are potential solution candidates in that they represent a local minima for the objective function. In fact, it is unlikely that a zero derivative will be realized by a perfectly matching objective. The higher likelihood is that solutions to Equation (65) will coincide

with the optimal solution. Observe in Figure 4-2 that the zero crossings of derivative terms correspond to rapidly deviating real and imaginary objective position E-field solutions. For this reason, the candidates for optimal values of a_0 may be found via a root-finding procedure in the derivative, as shown in Figure 4-2.

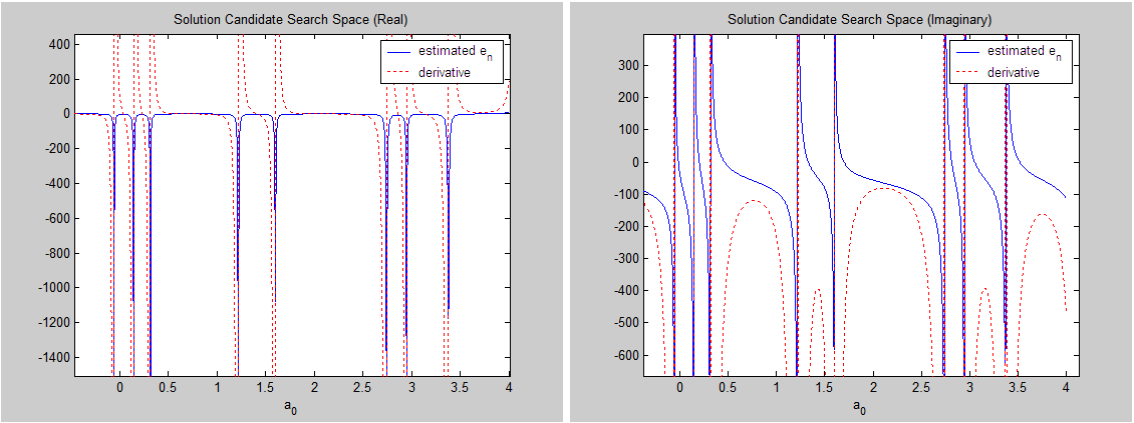

Figure 4-2. Example Real (left) and Imaginary (right) Eigenvector Deviation Search Space

Commensurate with experience, these optimum solutions are highly sensitive to choice of material parameterization, even for the case of a simple constant material adjustment. Once the eigendecomposition is completed, these potential solutions are generated rapidly as opposed to the tedious approach of continually exercising the prediction code and performing a search optimization. To compare the estimate with the true calculation, multiple calculations were performed and compared. The plot of results is shown in Figure 4-3, where the true value is in blue and the estimate is in red (dashed).

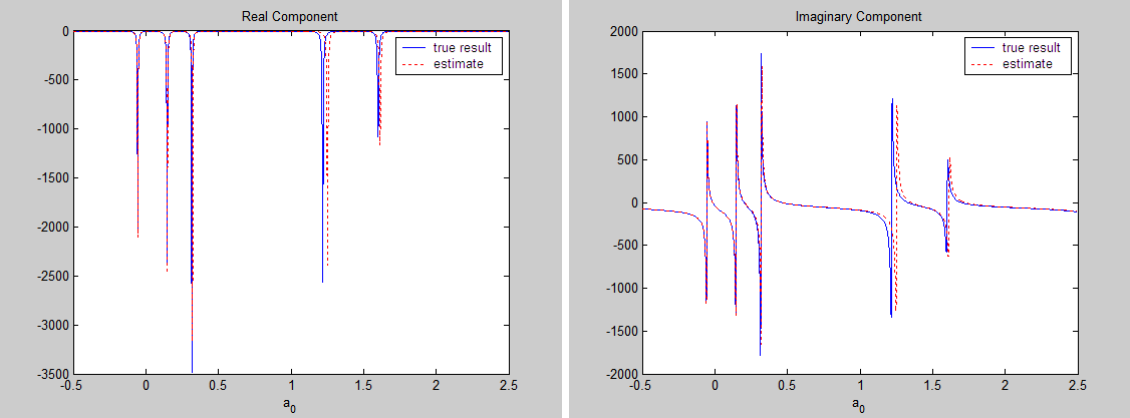

Figure 4-3. Comparison Between Estimated and True Pointwise Solutions (varying a_0)

As the plot above is generated from constant spacing of a_0, it is clear that the points desired (zero imaginary component and prescribed negative real component; e.g., a 50Ω input impedance for this geometry corresponds to a Z-directed E-field value of -200 V/cm) are highly sensitive. The accuracy will increase as a_0 approaches zero ($\boldsymbol{\lambda}^{-1}(0) = \boldsymbol{\lambda}^{-1}$), however, so a few iterations may be required. In Figure 4-3, observe that the error between plots (error in a_0) does indeed decrease with proximity to zero.

In the plots above, the true result was generated in approximately 8 hours versus 1.25 seconds on the same machine for the estimate (after eigendecomposition). The interesting (and encouraging) point to make in the plots above is that that the magnitude of the estimate in the regions of extrema is reasonably accurate. This bodes well for a global optimization solution.

4.3 Solution for Simple Textured Material

The constant material adjustment example may now be thought of as the first term in a basis designed to construct an optimal material solution to the objective. Indeed, an

overall eigenvalue deviation vector can be defined according to an arbitrary surface basis set. To generalize, assume a total eigenvalue deviation vector described by

$$\begin{aligned}\Delta\boldsymbol{\lambda} &= \sum_{\ell=0}^{L-1} a_\ell \, \Delta\boldsymbol{\lambda}_\ell \\ &= \mathbf{L}_{\Delta\lambda}\mathbf{a}\end{aligned}, \tag{66}$$

for $\mathbf{L}_{\Delta\lambda} = \left[\Delta\boldsymbol{\lambda}_0, \Delta\boldsymbol{\lambda}_1, \ldots, \Delta\boldsymbol{\lambda}_{L-1}\right]$, $\mathbf{a} = \left[a_0, a_1, \ldots, a_{L-1}\right]^T$, and some total number of deviation bases, L. Again returning to (50), the generalized form can be given by

$$\begin{aligned}\mathbf{e}(\mathbf{a}) &\approx \mathbf{X}\left[\boldsymbol{\lambda} + \mathrm{diag}\left(\mathbf{X}^{-1}\mathbf{f}\Delta\right)^{-1}\right]^{-1} \\ &= \mathbf{X}\left[\boldsymbol{\lambda} + \mathrm{diag}\left(\mathbf{f}^{-1}\mathbf{X}\mathbf{L}_{\Delta\lambda}\mathbf{a}\right)^{-1}\right]^{-1}\end{aligned}. \tag{67}$$

As before, the objective function

$$\begin{aligned}J(\mathbf{a}) &= \left|\left(\boldsymbol{\lambda} + \mathbf{L}_{\Delta\lambda}\mathbf{a}\right)^{-T}\boldsymbol{\beta}_n - e_{n,obj}\right|^2 \\ &= \left(\mathrm{Re}\left\{\left(\boldsymbol{\lambda} + \mathbf{L}_{\Delta\lambda}\mathbf{a}\right)^{-T}\boldsymbol{\beta}_n\right\} - \mathrm{Re}\left\{e_{n,obj}\right\}\right)^2 \\ &\quad + \left(\mathrm{Im}\left\{\left(\boldsymbol{\lambda} + \mathbf{L}_{\Delta\lambda}\mathbf{a}\right)^{-T}\boldsymbol{\beta}_n\right\} - \mathrm{Im}\left\{e_{n,obj}\right\}\right)^2\end{aligned}, \tag{68}$$

is minimized, where $\boldsymbol{\beta}_n = \mathbf{x}_n \odot \mathbf{b}$, and $e_{n,obj}$, $\mathbf{x}_n$, $\mathbf{b}$ are defined precisely as in Equation (52). The gradient of the objective is given by

$$\begin{aligned}\nabla_{\mathbf{a}} J(\mathbf{a}) = {} & -2\left(\mathrm{Re}\left\{\left(\boldsymbol{\lambda} + \mathbf{L}_{\Delta\lambda}\mathbf{a}\right)^{-T}\boldsymbol{\beta}_n\right\} - \mathrm{Re}\left\{e_{n,obj}\right\}\right)\mathrm{Re}\left\{\sum_{\ell=0}^{L-1} \hat{\mathbf{a}}_\ell \, \Delta\boldsymbol{\lambda}_\ell'^{T}\boldsymbol{\beta}_n\right\} \\ & -2\left(\mathrm{Im}\left\{\left(\boldsymbol{\lambda} + \mathbf{L}_{\Delta\lambda}\mathbf{a}\right)^{-T}\boldsymbol{\beta}_n\right\} - \mathrm{Im}\left\{e_{n,obj}\right\}\right)\mathrm{Im}\left\{\sum_{\ell=0}^{L-1} \hat{\mathbf{a}}_\ell \, \Delta\boldsymbol{\lambda}_\ell'^{T}\boldsymbol{\beta}_n\right\}\end{aligned}, \tag{69}$$

where $\hat{\mathbf{a}}_\ell$ is the ℓ^{th} unit vector and $\Delta\boldsymbol{\lambda}'_\ell$ is the partial derivative given by

$$\begin{aligned}\Delta\boldsymbol{\lambda}'_\ell &= \frac{\partial}{\partial a_\ell}\left(\boldsymbol{\lambda}+\mathbf{L}_{\Delta\lambda}\mathbf{a}\right)^{-1} \\ &= \Delta\boldsymbol{\lambda}_\ell \odot \left(\boldsymbol{\lambda}+\mathbf{L}_{\Delta\lambda}\mathbf{a}\right)^{-2}\end{aligned} . \tag{70}$$

Note that $\nabla_{\mathbf{a}} J(\mathbf{a}) = 0$ when $\forall \ell \in [0,1,\ldots,L-1], \Delta\boldsymbol{\lambda}'^{T}_{\ell}\boldsymbol{\beta}_n = 0$.

As an example, a second (non-orthogonal) basis was added in order to view the comparison in two dimensions. The basis set consisted of a constant (a_0) and a sinusoidal "rooftop" basis (a_1) over the span of the material solid itself. Plots showing the relative agreement between FEMA-BRICK computed results and those estimated via the scaling of two eigenvalue bases are shown in Figure 4-4. Just as in the case of scaling only, there is some divergence from the true result away from the origin. It is reasonable to expect that divergence will be a function of the distance from the origin for reasons mentioned earlier. There may be a limit to the number of parameters with which to model material changes, however, since the parametric limits must be bounded more tightly with the addition of each successive parameter.

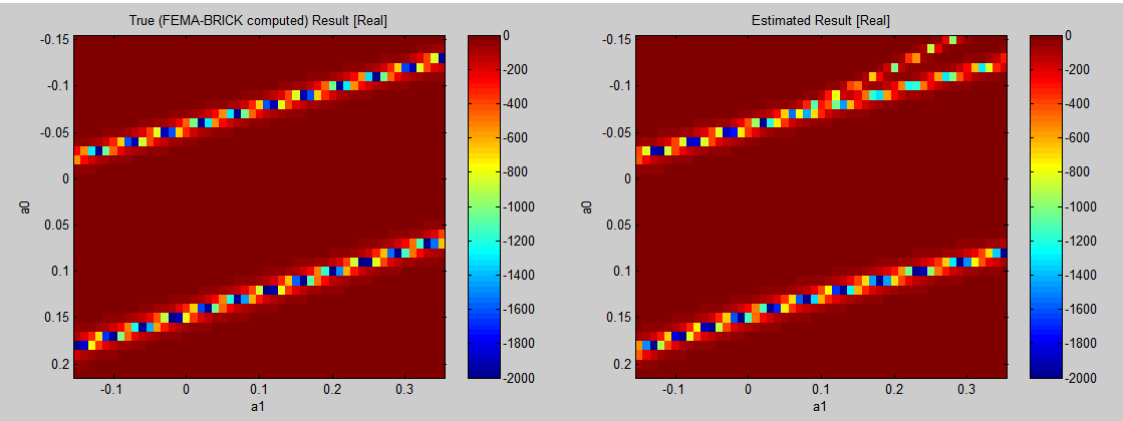

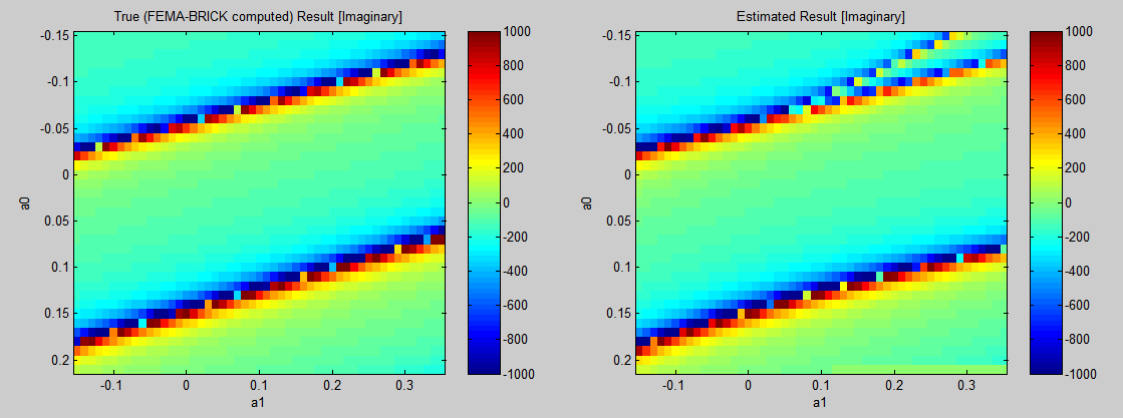

Figure 4-4. Comparison Between Estimated (left) and True (right) Pointwise Solutions (varying a_0 and a_1) for the Real (top) and Imaginary (bottom) Components

The concern over the limits in a parametric construct was not pursued in detail as part of this work, due to the findings contained in Chapter 5. It is nevertheless interesting that such a construct could be developed and solved in a manner amendable to genetic algorithms and the like. The narrowband results in the next section were obtained via an exhaustive search, considering only two parameters and a simple iteration. The iteration simply involved searching the two-parameter space for the next best solution, adjusting the substrate accordingly, and searching again.

4.4 Results for a Narrowband Exhaustive Search

Optimizations were performed using this small basis set as a proof of concept. Example results are shown below for the same original geometry shown in Figure 3-9 on page 51. In each case, the left-most figure shows the choice of optimum material profile and the right-most figure displays the resulting reflection loss. The first two examples were generated with relative ease and were representative of approximately 80% of the test runs performed. The third example illustrates an issue that could arise if the material bounds are allowed to exceed an upper limit.

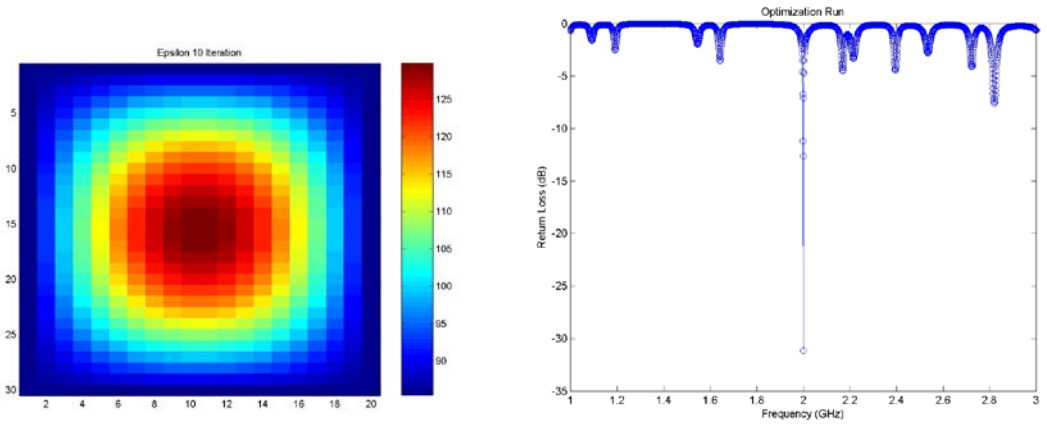

Figure 4-5. Test Narrowband Optimization (optimized at 2 GHz) for a Two-component Basis

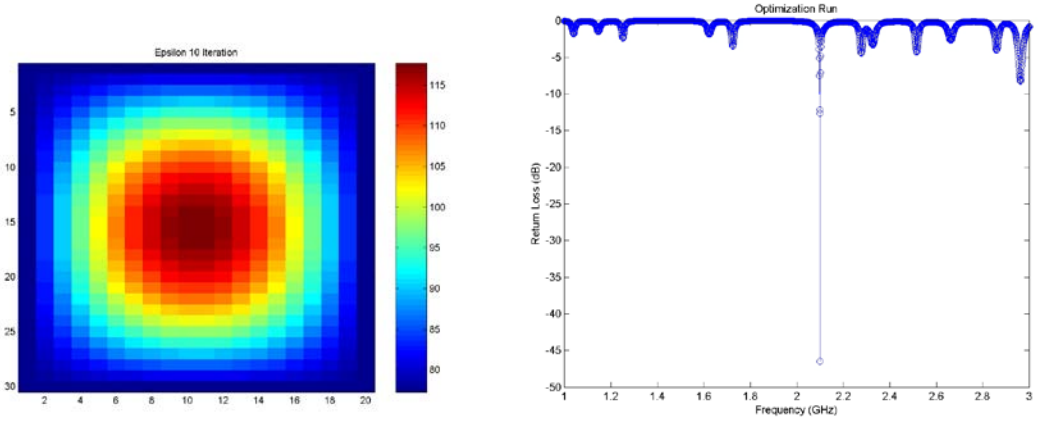

Figure 4-6. Test Narrowband Optimization (optimized at 2.1 GHz) for a Two-component Basis

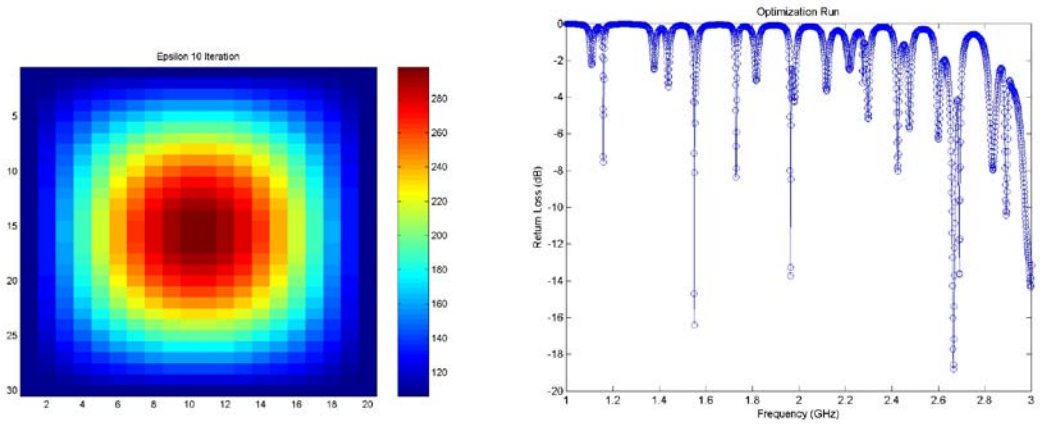

Figure 4-7. Test Narrowband Optimization (optimized at 1.55 GHz) for a Two-component Basis

While this last example did produce a reasonable minimum at the planned 1.55 GHz, it was clearly an inferior optimum when compared to the previous two cases. It is anticipated that this example highlights a failure in the choice of solid material model basis (2 component), and that an alternate basis may perform better. In this case, material values approaching $\mathrm{Re}\{\varepsilon_r\} = 300$ were considered to achieve the objective, and this quickly leads to a poorly conditioned FE-BI system.

CHAPTER 5 WIDEBAND SYSTEM OPTIMIZATION

This chapter extends the treatment of Chapter 4 to include how solutions covering a range of frequencies can be determined, allowing for fast wideband optimizations. It begins with the wideband system formulation of Section 3.1.2, and then discusses an appropriate eigendecomposition from which optimization can be performed.

5.1 Wideband System Matrix Eigendecomposition

The solution to the wideband approximate system takes the form

$$\mathbf{C}_{\mu}\left(k_0\right)\mathbf{e}\left(k\right)+\tilde{k}^2\mathbf{C}_{\varepsilon}\left(k_0;\ _t\right)\ \left(k\right)\approx\ \left(k\right)\ , \tag{71}$$

where $\tilde{k}=k/k_0$ is the normalized frequency. From the eigendecomposition

$$\mathbf{C}_{\varepsilon}^{-1}\left(k_0;\ _t\right)\ \boldsymbol{\varepsilon}_{\mu}\left(k_0;\mathbf{X}\right)\mathbf{X}\qquad^{-1}, \tag{72}$$

where t is the current textured material state, $\boldsymbol{\Lambda}=\mathrm{diag}\left(\lambda_i\right)$ is the eigenvalue matrix, and $\mathbf{X}$ is the matrix of associated eigenvectors, we can find

$$\mathbf{X}\boldsymbol{\Lambda}\mathbf{X}^{-1}\mathbf{e}\left(k\right)+\tilde{k}^2\mathbf{e}\left(k\right)\approx\mathbf{C}_{\varepsilon}^{-1}\left(k_0;\boldsymbol{\varepsilon}_t\right)\mathbf{f}\left(k\right)\ . \tag{73}$$

To solve this system, note that for each frequency, the relation

$$\left(\mathbf{X}\boldsymbol{\Lambda}\mathbf{X}^{-1}+\tilde{k}^2\,\mathbf{I}\right)\mathbf{e}(k)\approx\mathbf{C}_{\varepsilon}^{-1}\left(k_0;\boldsymbol{\varepsilon}_t\right)\mathbf{f}(k), \tag{74}$$

arises, which becomes

$$\begin{aligned}\mathbf{e}(k)&\approx\left(\mathbf{X}\quad\mathbf{X}\tilde{k}^2\quad\mathbf{C}^{-1}\right)^{-1}\boldsymbol{\varepsilon}_{\varepsilon}^{-1}(k_0;\ _t)\ (k)\\&=\mathbf{X}\boldsymbol{\Lambda}_k^{-1}\mathbf{X}^{-1}\mathbf{C}_{\varepsilon}^{-1}\left(k_0;\boldsymbol{\varepsilon}_t\right)\mathbf{f}(k)\end{aligned}, \tag{75}$$

where $\boldsymbol{\Lambda}_k=\mathrm{diag}\left(\lambda_i+\tilde{k}^2\right)$. For the case of reflection loss at a probe feed, $\mathbf{f}(k)=\tilde{k}\,\mathbf{f}(k_0)$, so the final probe location solution is given by

$$\mathbf{e}(k)\approx\mathbf{X}\ \mathbf{C}_{k'}^{1}\ ^{-1}\ \tilde{\varepsilon}^{1}(k_0;\ _t)\ (k_0), \tag{76}$$

for $\boldsymbol{\Lambda}_{k'}=\mathrm{diag}\left(\dfrac{\lambda_i+\tilde{k}^2}{\tilde{k}}\right)$. Several key insights emerge from examining this functional form of the eigendecomposition.

Extrema for $\mathbf{e}(k)$ occur near the frequencies for which

$$\left.\frac{d\boldsymbol{\Lambda}_{k'}^{-1}}{d\tilde{k}}\right|_{\tilde{k}=\tilde{k}_i}=\left.\frac{d}{d\tilde{k}}\mathrm{diag}\left(\frac{\tilde{k}}{\lambda_i+\tilde{k}^2}\right)\right|_{\tilde{k}=\tilde{k}_i}=\left.\mathrm{diag}\left(\frac{\lambda_i-\tilde{k}^2}{\left[\lambda_i+\tilde{k}^2\right]^2}\right)\right|_{\tilde{k}=\tilde{k}_i}=0. \tag{77}$$

The imaginary component of (77) is zero when $\angle\left(\lambda_i-\tilde{k}^2\right)=\angle\left(\left[\lambda_i+\tilde{k}^2\right]^2\right)$. To solve for the frequency location at the extrema, begin by setting

$$\frac{\mathrm{Re}\{\lambda_i\}-\tilde{k}_i^2}{\mathrm{Im}\{\lambda_i\}}=\frac{\left(\mathrm{Re}\{\lambda_i\}\right)^2-\left(\mathrm{Im}\{\lambda_i\}\right)^2+\tilde{k}_i^4+2\,\mathrm{Re}\{\lambda_i\}\tilde{k}_i^2}{2\,\mathrm{Im}\{\lambda_i\}\left(\mathrm{Re}\{\lambda_i\}+\tilde{k}_i^2\right)}. \tag{78}$$

This establishes the quadratic equation

$$3\tilde{k}_i^4 + 2\,\mathrm{Re}\{\lambda_i\}\tilde{k}_i^2 = |\lambda_i|^2, \tag{79}$$

which becomes

$$\tilde{k}_i^2 = -\frac{\mathrm{Re}\{\lambda_i\}}{3} + \sqrt{\frac{\mathrm{Re}\{\lambda_i\}^2}{9} + \frac{|\lambda_i|^2}{3}}. \tag{80}$$

Each imaginary component extreme of $\mathbf{\Lambda}_{k'}^{-1}$ locates a real resonance for the system, as will be shown later. Eigenvalues for this symmetric, but non-Hermitian, system are complex, and generally track the loss tangent of the material in $\mathbb{C}$-space, such that the imaginary eigenvalue components are small for low-loss materials. An example is shown in Figure 5-1 for two different cases of material loss tangent. The geometry is an offset probe-fed patch placed over a solid material substrate (5 cm x 5 cm x 0.25 cm equal-sized bricks).

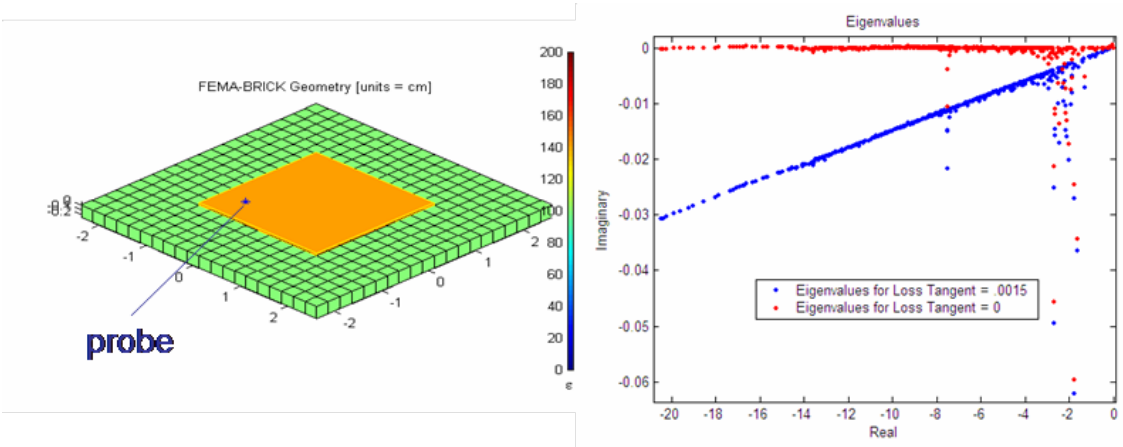

Figure 5-1. Example Geometry (left) and Associated Eigenvalues at 2.5 GHz (right) for Small ($\varepsilon_r = 100 - j0.15$) and Zero ($\varepsilon_r = 100$) Loss Tangents

For this reason, $\mathbf{\Lambda}_{k'}^{-1}$ is not singular for physically meaningful materials. When losses are small, $|\lambda_i| \approx -\mathrm{Re}\{\lambda_i\}$, and substituting this into (80) yields

$$\tilde{k}_i \approx \sqrt{|\lambda_i|} \approx \sqrt{-\mathrm{Re}\{\lambda_i\}} \,. \tag{81}$$

The approximation as a function of the loss-tangent trend is shown in Figure 5-1. Assuming $\tan\delta \approx \mathrm{Im}\{\lambda_i\}/\mathrm{Re}\{\lambda_i\}$, such that $\mathrm{Re}\{\lambda_i\} = -|\lambda_i|/\sqrt{1+\tan^2\delta}$, the error in the approximation as a function of loss tangent is obtained according to

$$\Delta\% = 100 \times \left. \frac{\left| \sqrt{1+\sqrt{1+3a^2}} - \sqrt{3a} \right|}{\left| \sqrt{1+\sqrt{1+3a^2}} \right|} \right|_{a=\sqrt{1+\tan^2\delta}} \,. \tag{82}$$

The error does not approach 1% until the loss tangent exceeds 0.29. Since low-loss textured material designs are sought, the approximation of Equation (81) is used from here forward.

Adding loss to materials is a common practice for wideband antenna design. It is well-known that one way to increase bandwidth for a particular design is to add loss to materials associated with the antenna in a controlled way, in order to optimize the engineering trade between good bandwidth and good overall performance (efficiency and gain). An increased material loss tangent causes the frequency performance of eigenvalues at resonance to be dampened in magnitude. The appropriate amount of dampening not only causes the resonance to better approach the objective value, it also lessens the sensitivity of the magnitude in the vicinity of the resonance (it becomes less

"peaky"). This is easy to see by examining the pole behavior of $\left|\tilde{k}\Big/\left(\lambda_i+\tilde{k}^2\right)\right|$ for normalized frequencies near $\tilde{k}=1$, and $\lambda_i=-1-j\tan\delta$. A plot is shown in Figure 5-2, where the magnitude is simply $\left[\tan\delta\right]^{-1}$ for a small set of various loss tangents. Note the improved behavior in the resonant response at the pole location that accompanies the introduction of additional loss.

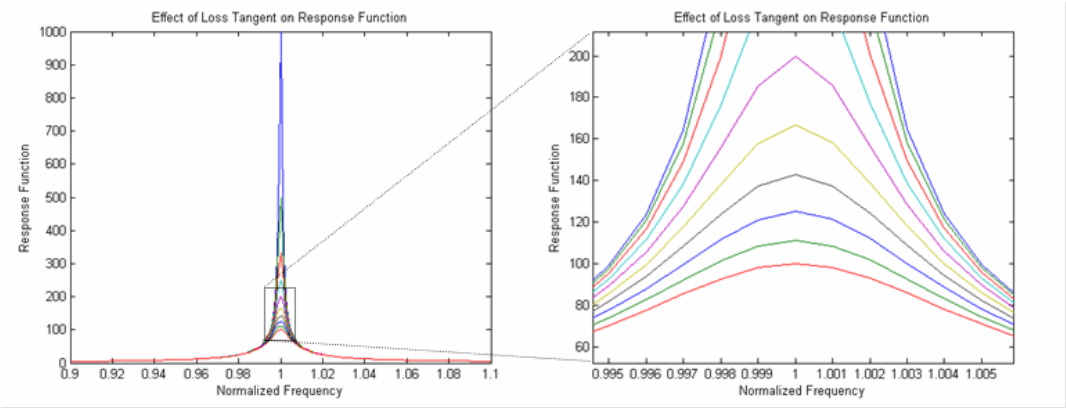

Figure 5-2. Illustration of How Loss Tangent Affects Eigenvalue Pole Behavior

Also noteworthy is the fact that these resonances may lie well outside the band of interest. As such, they do not contribute significantly to the overall reflection loss response function. A general rule for retaining eigenvalues in the approximation of Equation (76) is given by

$$\tilde{k}_{\min}\le\sqrt{\left|\lambda_i\right|}\le\tilde{k}_{\max}, \tag{83}$$

where the frequency range is given by $\tilde{k}\in\left[\tilde{k}_{\min},\tilde{k}_{\max}\right]$. One may, however, choose to keep a few more eigenvalues near the boundary such that this rule should be regarded as approximate.

As in the narrowband case, the new system seeks to achieve particular objective values in one row of $\mathbf{E} = \left[\mathbf{e}_1, \mathbf{e}_2, \ldots, \mathbf{e}_N\right]^T$. If the n^{th} vector is chosen to have as its objective the value(s) $\mathbf{e}_{n,obj} = \left[e_{n,obj}\left(k_1\right), e_{n,obj}\left(k_2\right), \ldots, e_{n,obj}\left(k_F\right)\right]^T$ (a vector containing objectives for each frequency), the constraint equation

$$e_{n,obj}\left(k\right) = \mathbf{x}_n^T \boldsymbol{\Lambda}_k^{-1} \boldsymbol{\beta}\left(k_0, \boldsymbol{\varepsilon}_t\right), \tag{84}$$

is given where

$$\boldsymbol{\beta}\left(k_0; \boldsymbol{\varepsilon}_t\right) = \mathbf{X}^{-1} \mathbf{C}_{\varepsilon}^{-1}\left(k_0; \boldsymbol{\varepsilon}_t\right) \mathbf{f}\left(k_0\right), \tag{85}$$

for each $k \in \left[k_1, k_2, \ldots, k_F\right]$, and $\mathbf{X} = \left[\mathbf{x}_1, \mathbf{x}_2, \ldots, \mathbf{x}_N\right]^T$. This particular constraint equation can be simplified even further (to an *N*-point inner product) by noting that

$$e_{n,obj}\left(k\right) = \boldsymbol{\lambda}_{k'}^{-T} \boldsymbol{\gamma}_n\left(k_0; \boldsymbol{\varepsilon}_t\right), \tag{86}$$

for

$$\boldsymbol{\gamma}_n\left(k_0; \boldsymbol{\varepsilon}_t\right) = \mathbf{x}_n \odot \boldsymbol{\beta}\left(k_0; \boldsymbol{\varepsilon}_t\right), \tag{87}$$

where $\odot$ is the point-wise (Hadamard) product, and $\boldsymbol{\lambda}_{k'}^{-T} = \left[\left(\lambda_1 \tilde{k}^{-1} + \tilde{k}\right)^{-1}, \left(\lambda_2 \tilde{k}^{-1} + \tilde{k}\right)^{-1}, \ldots, \left(\lambda_N \tilde{k}^{-1} + \tilde{k}\right)^{-1}\right]$.

5.2 Validation of Eigendecomposition Approximation

The basic approximation is tested by examining the electric field unknown at the probe location of the electrically small patch antenna example of Figure 5-1, based on a

constant permittivity substrate having $\varepsilon_r = 100 - j0.15$. The center frequency of 2.5 GHz is selected and the wideband behavior from 1 to 4 GHz is used, so that the normalized frequency range is from 0.4 to 1.6. From Equation (83), the applicable eigenvalues for this frequency range should satisfy $|\lambda_i| \in [0.16, 2.56]$, comprising only 68 of the available 901 eigenvalues. These are shown as asterisks in the dotted bounding box in Figure 5-3.

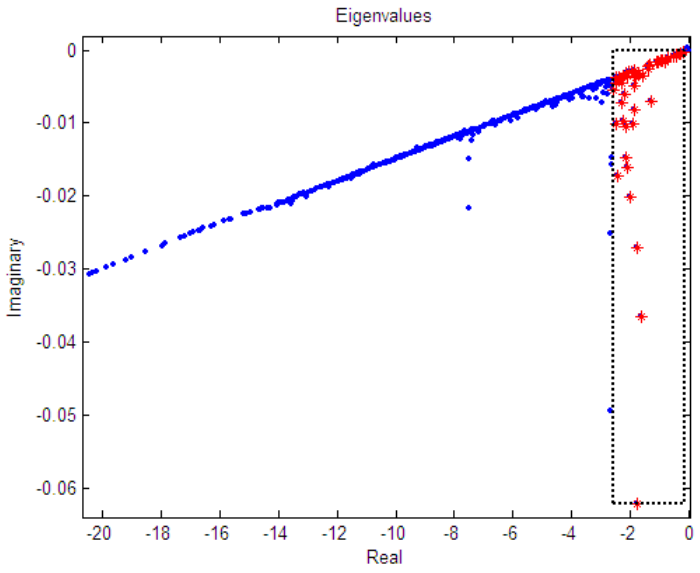

Figure 5-3. Eigenvalues associated with the geometry of Figure 5-1 at 2.5 GHz; dotted bounding box shows the eigenvalues with fall within the range $|\lambda_i| \in [0.16, 2.56]$

Retaining these 68 eigenvalues, Equation (76) is invoked to plot the real and imaginary parts of the E-field unknown value at the probe location as a function of frequency. These data are compared to those obtained from the full wave direct FE-BI predictions. For this example, the field at 300,000 frequency points was computed in 15 seconds (after eigen-decomposition). In contrast, the direct FEMA-BRICK prediction required over 200 seconds on the same CPU to produce about 60 points (insufficiently sampled). Asterisks

in the plots show a more finely sampled sub-segment via direct FEMA-BRICK prediction.

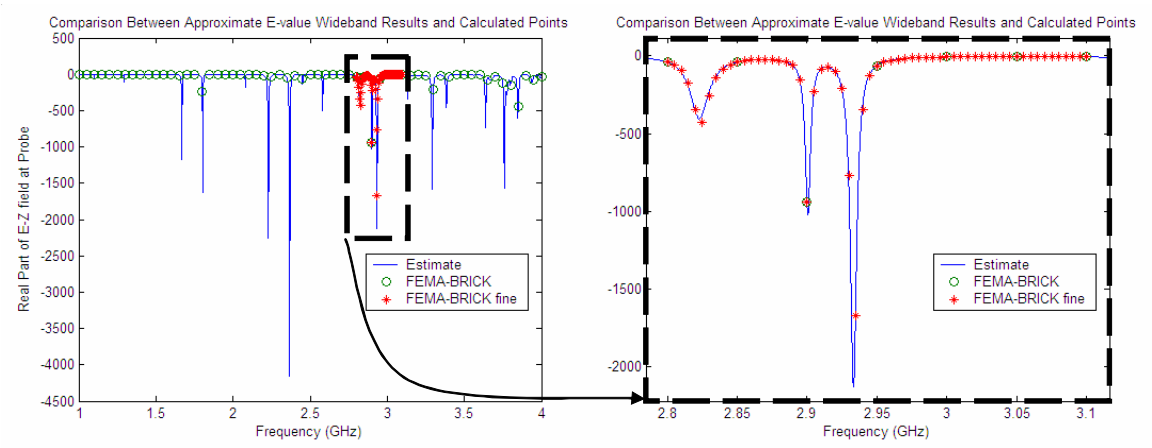

Figure 5-4. Eigenvalue approximation and FEMA-BRICK prediction (with the real part of E-field unknown at probe location) using 68 eigenvalues

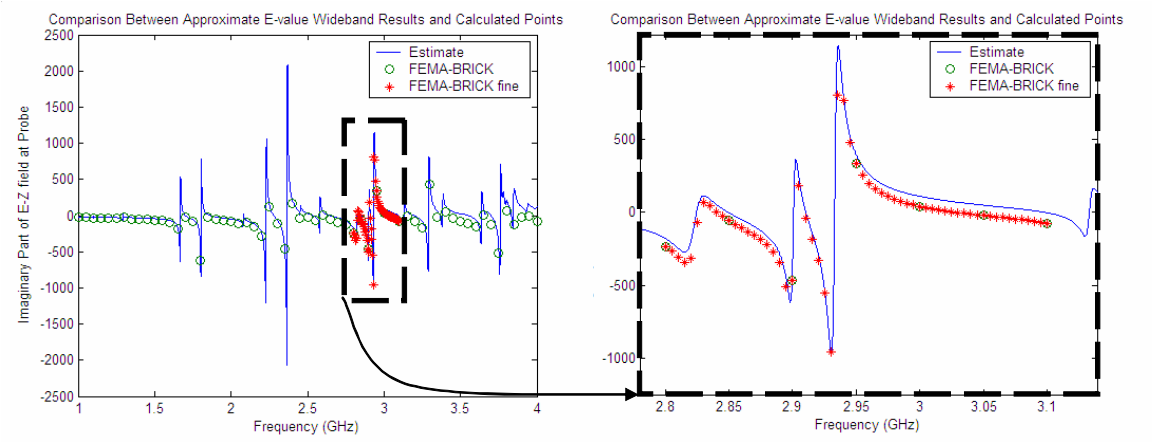

Figure 5-5. Eigenvalue approximation and FEMA-BRICK prediction (with the imaginary part of E-field unknown at probe location) using 68 eigenvalues

Note a slight bias in the imaginary terms of the approximation. This is easily remedied by using all 901 eigenvalues in the approximation because all contributing residues are now considered. Figure 5-6 shows exact agreement between the eigenvalue approach and the FEMA-BRICK result. In general, however, the real components of the E-field

unknowns are most critical. From a standpoint of speed for this computation, the difference between using 901 eigenvalues and 68 eigenvalues is approximately 90 seconds versus 15 seconds on the same CPU for 300,000 frequency points.

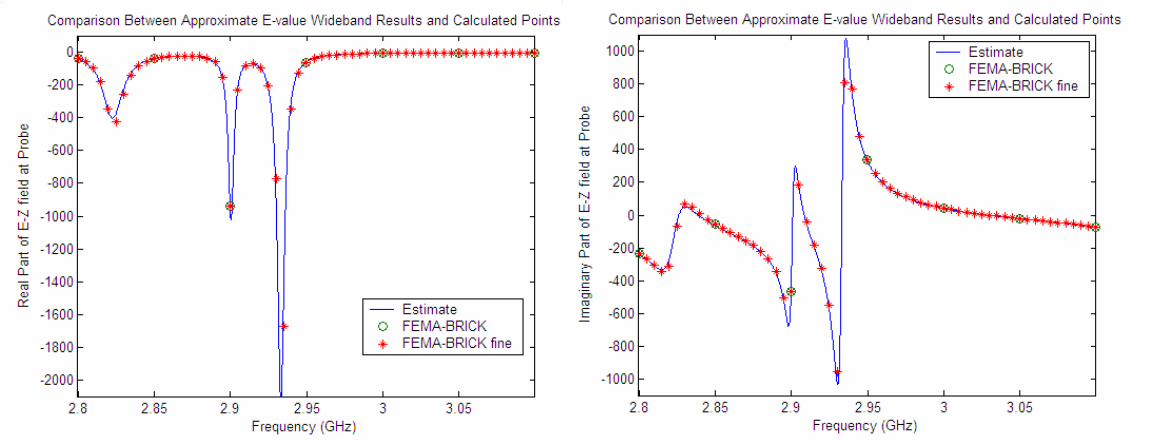

Figure 5-6. Eigenvalue approximation and FEMA-BRICK prediction (with the E-field unknown at probe location – real and imaginary) using all 901 eigenvalues

Over a large fractional bandwidth, the solution can be computed using an effective perturbation to the eigenvalues (i.e., the frequency-dependence of eigenvalues). In this section, the eigenvalues themselves were treated as constant so that the poles were located by the normalized frequency itself. In the next section, through material optimization, these eigenvalues are adjusted to produce a desired characteristic over a band.

5.3 Material Update Characteristics

As in the narrowband case, the permittivity-based finite element matrix can be decomposed as

$$\mathbf{A}_{\varepsilon}^{(2)}\left(k_0,\mathbf{L}_i,\mathbf{D}_i\right)=\qquad^{T}. \tag{88}$$

Provided the material characteristics are largely captured in $\mathbf{D} = \mathrm{diag}(\mathbf{d})$, a material deviation matrix $\Delta\mathbf{D} = \mathrm{diag}(\Delta\mathbf{d})$ is sought such that

$$\begin{aligned}(\mathbf{X}+\lambda\Delta\mathbf{X})\left[\mathrm{diag}(\lambda)+\mathrm{diag}(\mathbf{X})\right](\quad+\Delta\quad)^{-1} = \\ \left\{\mathbf{G}^{(1)}(k_0)+(\mathbf{L}+\Delta\mathbf{L})\left[\mathrm{diag}(\mathbf{d})+\mathrm{diag}(\Delta\mathbf{d})\right](\mathbf{L}+\Delta\mathbf{L})^T\right\}^{-1}\mathbf{C}_\mu(k_0;\ _t),\end{aligned} \tag{89}$$

where any update to the system will correspondingly affect the decomposition of the system by an appropriate Δ. If the lower triangular matrix in the LDL decomposition maintains consistency in the update $[(\mathbf{L}+\Delta\mathbf{L})\rightarrow\mathbf{L}]$, then

$$\begin{aligned}&(\mathbf{X}+\lambda\Delta\mathbf{X})\left[\mathrm{diag}(\lambda)+\mathrm{diag}(\mathbf{X})\right](\quad+\Delta\quad)^{-1} \\ &\quad\approx\left\{\mathbf{G}^{(1)}(k_0)+\mathbf{L}\left[\mathrm{diag}(\mathbf{d}+\Delta\mathbf{d})\right]\mathbf{L}^T\right\}^{-1}\mathbf{C}_\mu(k_0;\ _t) \\ &\quad=\left\{\mathbf{C}_\varepsilon(k_0;\mathbf{L}_t)+\quad\left[\mathrm{diag}(\Delta\quad)\right]\mathbf{C}^T\right\}^{-1}\quad\varepsilon_\mu(k_0;\ _t)\quad,\end{aligned} \tag{90}$$

such that

$$\begin{aligned}&\left[\mathrm{diag}(\lambda)+\mathrm{diag}(\Delta\lambda)\right] \\ &\quad\approx(\mathbf{X}+\Delta\mathbf{X})^{-1}\left\{\mathbf{C}_\varepsilon(k_0;\ _t)+\mathbf{L}\left[\mathrm{diag}(\Delta\quad)\right]\varepsilon^T\right\}^{-1}\mathbf{X}\quad_\mu(\mathbf{X}_0;\ _t)(\quad+\Delta\quad).\end{aligned} \tag{91}$$

This approximation is tested by comparing the two sides of the above relation, revisiting the geometry of Figure 5-1. The initial geometry is again a constant substrate value of $\varepsilon_r = 100 - j0.15$, and the "delta" geometry is a small random perturbation to each block of the substrate. The first comparison is given in Figure 5-7 for the case of a uniform random weighting of $[0.95,1.05]$ applied to all substrate bricks. The second comparison of Figure 5-8 is for the case of a uniform random weighting of $[0.5,1.5]$ applied to all

substrate bricks. In each case, an LDL decomposition was used to determine the diagonal values and compute $\Delta\mathbf{d}$. The solution on the right was strongly diagonal in all cases, so only the quantitative diagonal is shown in the next two examples.

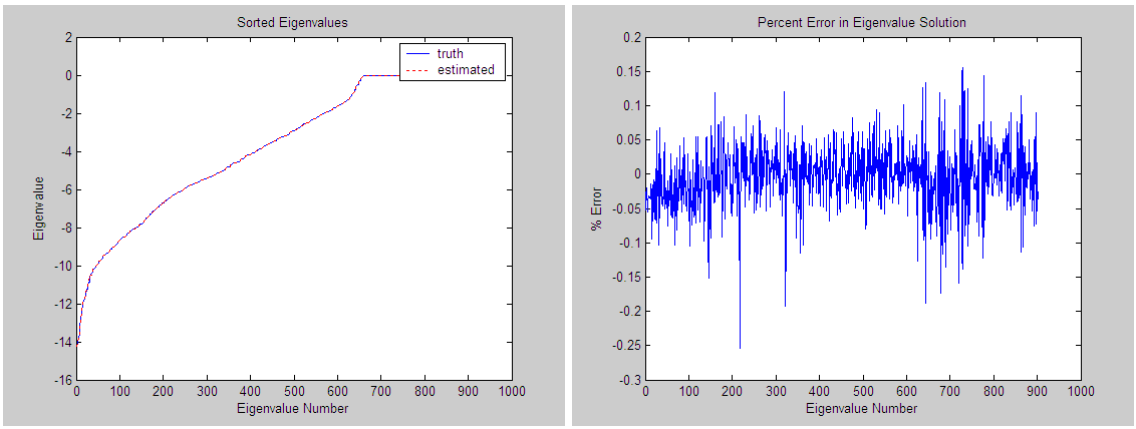

Figure 5-7. Approximation on left side of Equation (91) (left), and the Error of the Approximation for Random Weighting of $[0.95,1.05]$

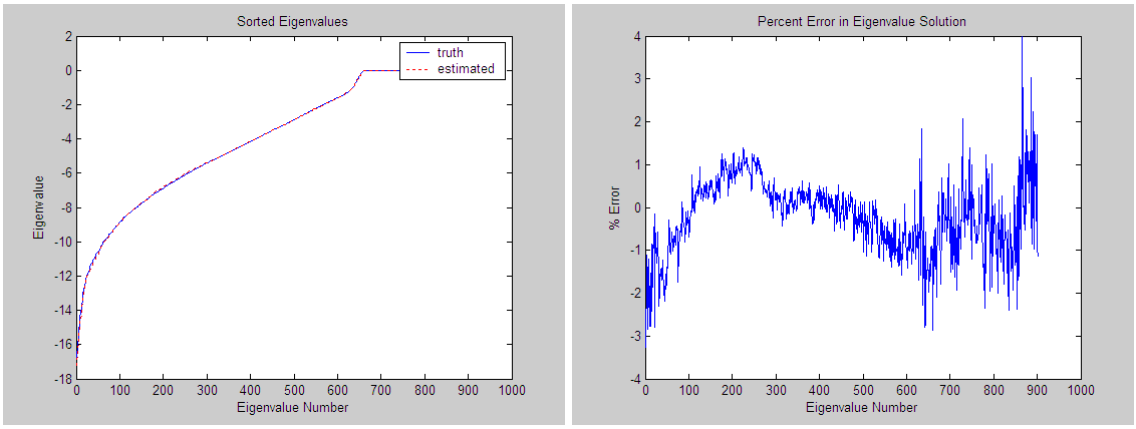

Figure 5-8. Approximation on left side of Equation (91) (left), and the Error of the Approximation for Random Weighting of $[0.5,1.5]$

The approximation appears to deteriorate in a reasonable fashion with increased material deviation and tends to lend credence to the idea that $(\mathbf{L}+\Delta\mathbf{L})\rightarrow\mathbf{L}$ is a fair assumption. This confirms that the lower triangular matrix in the LDL decomposition is largely

dependent on geometry as opposed to material. While the right side of Equation (91) is strongly diagonal, the random perturbations appear to affect the entire error matrix, and are correlated with the strength of the diagonal elements themselves (hence, a consistent percentage error).

Finally, in order to solve for material changes *given* a desired eigenvalue-deviation, small updates are encouraged such that $\mathbf{X}+\Delta\mathbf{X}\rightarrow\mathbf{X}$. In order to discuss the update of eigenvalues and material vectors as weighted updates, the derivation changes slightly at this point. This begins by defining

$$\begin{aligned}\left(\mathbf{X}\mathbf{W}_X\right)\left(\mathbf{W}_\Lambda\mathbf{X}\right)\left(\mathbf{W}_X\right)^{-1} \\ \approx\left\{\mathbf{L}\left(\mathbf{W}_D\mathbf{D}\right)\mathbf{L}^T\right\}^{-1}\mathbf{C}_\mu\left(k_0;\ _t\right)\end{aligned}, \tag{92}$$

such that

$$\mathbf{L}\left(\mathbf{W}_D\mathbf{D}\right)\mathbf{L}^T\left(\mathbf{X}\mathbf{W}_X\right)\left(\mathbf{C}_\Lambda\right)\approx\ _\mu\left(\mathbf{W}_0;\ _t\right)\left(\ _X\right), \tag{93}$$

where $\mathbf{D}$ and Λ are as defined before, and $\mathbf{W}_D=\mathrm{diag}\left(\mathbf{w}_d\right)$ and $\mathbf{W}_\Lambda=\mathrm{diag}\left(\mathbf{w}_\lambda\right)$ are the corresponding update weight matrices. The matrix $\mathbf{W}_X$ is of a non-specific structure and describes the update of the eigenvector matrix. The assumption that $\mathbf{X}+\Delta\mathbf{X}\rightarrow\mathbf{X}$ portends $\mathbf{W}_X\rightarrow\mathbf{I}$. The original (unweighted) relation is given by

$$\mathbf{L}\mathbf{D}\mathbf{L}^T\mathbf{X}\Lambda\approx\mathbf{C}_\mu\left(k_0;\ _t\right)\mathbf{X}\ , \tag{94}$$

such that

$$\mathbf{D}\mathbf{L}^T\mathbf{X}\Lambda \approx \mathbf{L}^{-1}\mathbf{C}_\mu(k_0,\varepsilon_t)\mathbf{X} \quad . \tag{95}$$

Similarly, for the weight update case,

$$(\mathbf{W}_D\mathbf{D})\mathbf{L}^T(\Lambda\mathbf{W}_X)(\mathbf{L}\,\mathbf{C}_\Lambda) \approx {}^{-1}\varepsilon_\mu(\mathbf{X}\mathbf{W}_t)(\quad_X). \tag{96}$$

Manipulating terms slightly,

$$\mathbf{W}_D\mathbf{L}^{-1}\mathbf{C}_\mu(\mathbf{X}\Lambda;\mathbf{W}\quad\Lambda^{-1}\mathbf{W}_X(\mathbf{L}\,\mathbf{C}_\Lambda) \approx {}^{-1}\varepsilon_\mu(\mathbf{X}\mathbf{W}_t)(\quad_X), \tag{97}$$

such that

$$\mathbf{W}_D\mathbf{M} \approx \mathbf{M}\mathbf{W}_\Lambda\mathbf{W}\Lambda^1\quad^{-1}_X \quad , \tag{98}$$

for $\mathbf{M} = \mathbf{I}\varepsilon^{-1}\mathbf{C}\mathbf{X}_\mu(k_0;\ _t)$. The small update assumption, $\mathbf{W}_X \to \mathbf{I}$, then makes this become simply

$$\mathbf{W}_D\mathbf{M} \approx \mathbf{M}\mathbf{W}_\Lambda^{-1}. \tag{99}$$

This takes on the form of a similarity transformation and, as such, will not allow both $\mathbf{W}_D$ and $\mathbf{W}_\Lambda$ to be perfectly diagonal simultaneously (except for the trivial $\mathbf{M} = \mathbf{I}$ case).

In general, $\mathbf{M}$ is poorly conditioned, but is close to column-wise orthogonal. Further, the columns of $\mathbf{M}$ which induce most of the conditioning issues typically align with elements of Λ which are near zero. As such, weighting elements (of $\mathbf{W}_\Lambda$) have no effect in these regions such that direct solutions are not possible. To solve for $\mathbf{W}_D$, find $\mathbf{Q}$ and $\mathbf{R}$ such that

$$\mathbf{M} = \mathbf{Q}^H \mathbf{R} \quad for \quad \mathbf{Q}^H \mathbf{Q} = \mathbf{I}, \tag{100}$$

using an orthogonalization routine (e.g., Gram-Schmidt), and then cast equation (99) as

$$\begin{aligned} \mathbf{R}\mathbf{W}_\Lambda^{-1} &\approx \mathbf{Q}\mathbf{W}_D\mathbf{Q}^H\mathbf{R} \\ &= \left(\sum_i w_{d,i}\, \mathbf{q}_i \mathbf{q}_i^H \right) \mathbf{R} \end{aligned}. \tag{101}$$

The best estimate of update weights is found according to

$$w_{D,i} \approx \frac{\mathbf{q}_i^H \mathbf{R} \mathbf{W}_\Lambda^{-1} \left(\mathbf{q}_i^H \mathbf{R} \right)^H}{\left(\mathbf{q}_i^H \mathbf{R} \right)^H \left(\mathbf{q}_i^H \mathbf{R} \right)}. \tag{102}$$

There are notable inefficiencies associated with making use of these update weights, starting with the initial approximation of equation (99). Typical runs involving the above update equation produce relatively little response in $\mathbf{w}_d = \left[w_{d,1}, w_{d,2}, \ldots, w_{d,N} \right]$ for a given choice of $\mathbf{w}_\lambda = \left[w_{\lambda,1}, w_{\lambda,2}, \ldots, w_{\lambda,N} \right]$. Proportionally, the weights induce the desired effect, but amplification is required to avoid an inordinately large number of iterations. Trials have found that a reasonable update weight can be found for a suitable choice of α such that

$$\mathbf{w}_d^{(\alpha)} = \left[w_{d,1}^\alpha, w_{d,2}^\alpha, \ldots, w_{d,N}^\alpha \right], \tag{103}$$

implying the application of the same weights α times. Large eigenvalue-deviations tend to invalidate the assumptions leading to the equation above, so care must be exercised to perform reasonable corrections during material updates. It is, however, important to

consider that a constant material adjustment can be performed virtually without penalty, since $\mathbf{W}_X = \mathbf{I}$. Assigning $\mathbf{W}_\Lambda = (1+a_0)\mathbf{I}$, for a constant a_0, the material weighting becomes the simple inverse, $\mathbf{W}_D = (1+a_0)^{-1}\mathbf{I}$. As in the previous narrowband development, begin by examining a constant material adjustment only and enforce $a_0 \in \{\mathbb{R}; a_0 > -1\}$. For this, an approximate material multiplication factor is given by the material weight vector $\mathbf{w}_d = (1+a_0)^{-1}$. Returning to Equation (76), the material change is introduced to obtain

$$\mathbf{\Lambda}_{k'} = \text{diag}\left(\frac{\lambda_i \left[1+a_0\right] + \tilde{k}^2}{\tilde{k}} \right). \tag{104}$$

For this example, the estimated performance at the feed over a wide bandwidth and range of constant material adjustments can be quickly obtained, as shown in Figure 4-3. These response functions are entirely expected since the effect of increased material density (increased a_0) is to compress the response.

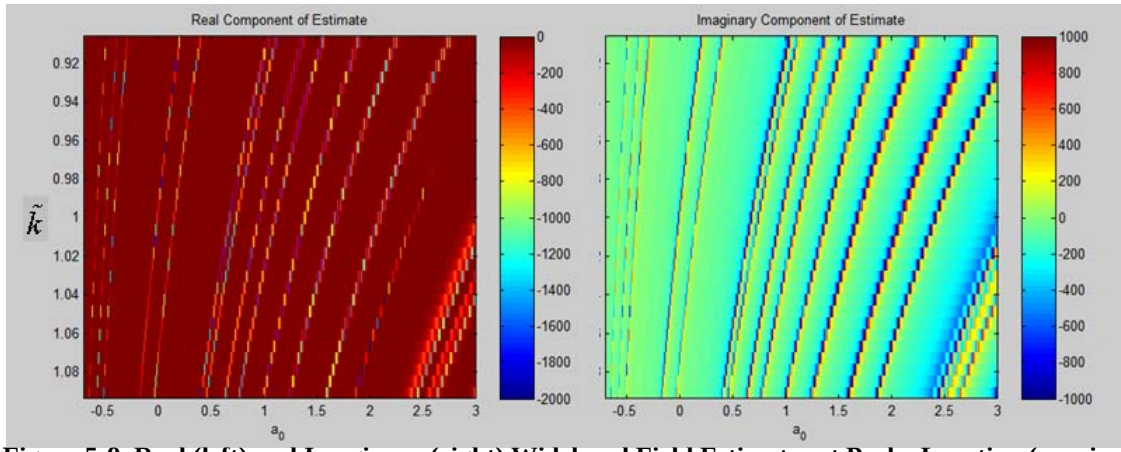

Figure 5-9. Real (left) and Imaginary (right) Wideband Field Estimates at Probe Location (varying $\tilde{k}$ and a_0)

Since updates are provided via the material weighting vector, $\mathbf{w}_\varepsilon$, the relation

$$\mathbf{w}_d = \mathbf{T}_\varepsilon \mathbf{w}_\varepsilon \quad \Leftrightarrow \quad \mathbf{w}_\varepsilon = \mathbf{T}_\varepsilon^{+} \mathbf{w}_d \,, \tag{105}$$

is used to complete the development.

5.4 Manipulation of Eigenvalues for Optimization

The next goal is to modify the eigenvalues directly in order to achieve some desired result. From the above [and Equation (86)] the relation

$$e_{n,obj}\left(k\right) = \boldsymbol{\lambda}_{k'}^{-T} \boldsymbol{\gamma}_n \left(k_0; \boldsymbol{\varepsilon}_t\right), \tag{106}$$

is given for $\boldsymbol{\lambda}_{k'}^{-T} = \left[\left(\lambda_1 w_{\lambda,1}\, \tilde{k}^{-1} + \tilde{k}\right)^{-1}, \left(\lambda_2 w_{\lambda,2}\, \tilde{k}^{-1} + \tilde{k}\right)^{-1}, \ldots, \left(\lambda_N w_{\lambda,N}\, \tilde{k}^{-1} + \tilde{k}\right)^{-1}\right]$. The analysis begins by allowing for total freedom in the adjustment of the $\mathbf{w}_\lambda$ components. In essence, the eigenvalue inverse variables are adjusted as given by (106) above to a form which produces a more favorable result. Expanding this relation,

$$e_{n,obj}\left(\tilde{k},\mathbf{w}_{\lambda},\right)=\boldsymbol{\gamma}_{k'}^{-T}{}_{n}\boldsymbol{\varepsilon}\left(k_0;{}_{t}\right)$$
$$=\sum_{\eta=1}^{N}\frac{\left[\boldsymbol{\gamma}_n\left(k_0;\boldsymbol{\varepsilon}_t\right)\right]_\eta}{\lambda_\eta w_{\lambda,\eta}\tilde{k}^{-1}+\tilde{k}}. \tag{107}$$

In order to prescribe a wideband solution, recognize the following: the design will consist of multiple independent and coincident poles. The location of the pole(s) is a slight adjustment to (81) and is given by

$$\tilde{k}_\eta \approx \sqrt{-\mathrm{Re}\left\{\lambda_\eta w_{\lambda,\eta}\right\}}, \tag{108}$$

such that $\tilde{k}_{\eta_1}=\tilde{k}_{\eta_2}\sqrt{w_{\lambda,\eta_2}/w_{\lambda,\eta_1}}$. The resonance shifts with the square root of the eigenvalue weighting applied. Decreasing eigenvalue weighting shifts the resonance upward in frequency, while an increasing weight shifts the resonant location lower in frequency.

The magnitude of the resonance *due to a particular eigenvalue* at its pole location is recognized by observing that

$$\left.\frac{\left[\boldsymbol{\gamma}_n\left(k_0;\boldsymbol{\varepsilon}_t\right)\right]_\eta}{\lambda_\eta w_{\lambda,\eta}\tilde{k}^{-1}+\tilde{k}}\right|_{\tilde{k}=\tilde{k}_\eta}=\frac{\left[\boldsymbol{\gamma}_n\left(k_0;\boldsymbol{\varepsilon}_t\right)\right]_\eta \tilde{k}_\eta}{\lambda_\eta w_{\lambda,\eta}+\tilde{k}_\eta^2}$$
$$=\frac{\left[\boldsymbol{\gamma}_n\left(k_0;\boldsymbol{\varepsilon}_t\right)\right]_\eta \sqrt{-\mathrm{Re}\left\{\lambda_\eta w_{\lambda,\eta}\right\}}}{\mathrm{Re}\left\{\lambda_\eta w_{\lambda,\eta}\right\}+j\,\mathrm{Im}\left\{\lambda_\eta w_{\lambda,\eta}\right\}-\mathrm{Re}\left\{\lambda_\eta w_{\lambda,\eta}\right\}}, \tag{109}$$
$$=\frac{\left[\boldsymbol{\gamma}_n\left(k_0;\boldsymbol{\varepsilon}_t\right)\right]_\eta \sqrt{-\mathrm{Re}\left\{\lambda_\eta w_{\lambda,\eta}\right\}}}{j\,\mathrm{Im}\left\{\lambda_\eta w_{\lambda,\eta}\right\}}$$

At the location(s) of these pole(s), the magnitude is given by

$$e_{n,obj}\left(\tilde{k}_{P_W}, w_{\lambda,P_W}\right) \approx \sum_{p\in P_W} \frac{\left[\boldsymbol{\gamma}_n\left(k_0;\boldsymbol{\varepsilon}_t\right)\right]_p \sqrt{-\mathrm{Re}\left\{\lambda_p w_{\lambda,p}\right\}}}{j\,\mathrm{Im}\left\{\lambda_p w_{\lambda,p}\right\}\sqrt{}}, \tag{110}$$

where $p \in P_W$ is the set of all coincident poles after weighting. Coincident poles refer to eigenvalue terms having identical frequency locations. Clearly, there is a balanced relationship between resonant location and magnitude. Adjusting eigenvalue weights shifts the resonance location, but it also affects the magnitude. If two or more frequency locations are the same, the sum can grow dramatically at that location. These resonant spaces are very sensitive, so a slight shift apart can make the magnitude manageable.

The eigenvalue weighting is the only quantity which may be adjusted, since $\boldsymbol{\gamma}_n\left(k_0;\boldsymbol{\varepsilon}_t\right)$ and $\boldsymbol{\lambda}$ are established at the outset. If the normalized bandwidth is specified, such that $\tilde{k} \in \left[\tilde{k}_1, \tilde{k}_2\right]$, then the poles of interest must lie in this range. Further note that

$$\begin{aligned} e_{n,obj} &\le \mathrm{Re}\left\{\frac{\left[\boldsymbol{\gamma}_n\left(k_0;\boldsymbol{\varepsilon}_t\right)\right]_p \sqrt{-\mathrm{Re}\left\{\lambda_p w_{\lambda,p}\right\}}}{j\,\mathrm{Im}\left\{\lambda_p w_{\lambda,p}\right\}}\right\} \\ &= \frac{\mathrm{Im}\left\{\left[\boldsymbol{\gamma}_n\left(k_0;\boldsymbol{\varepsilon}_t\right)\right]_p\right\}\sqrt{-\mathrm{Re}\left\{\lambda_p w_{\lambda,p}\right\}}}{\mathrm{Im}\left\{\lambda_p w_{\lambda,p}\right\}} \end{aligned} \tag{111}$$

is required for all p, since the sum of these components must achieve the objective (a value below the objective can not achieve the objective in the sum unless losses are introduced) – refer to Figure 5-4 to note that the standard objective is real and negative. In practice, this inequality may be relaxed depending on the accuracy of the wideband solution sought. Maintaining the inequality for now,

$$B_{n,p} = \mathrm{Im}\left\{\left[\boldsymbol{\gamma}_n\left(k_0;\boldsymbol{\varepsilon}_t\right)\right]_p\right\}\frac{\mathrm{Re}\left\{\lambda_p\right\}}{\mathrm{Im}\left\{\lambda_p\right\}} \leq -\tilde{k}_p\, e_{n,obj} \tag{112}$$

is found as a required inequality for the choice of candidate eigenvalues if it is not the intention to induce loss (i.e., only allow real weighting). This is an important result, because it allows for the quick elimination of eigenvalues within the system from any further consideration in the optimization. The best solution is formulated by adjusting only those eigenvalues which remain. From a practical standpoint, it is also not necessary (and is sometimes problematic) to retain eigenvalue candidates if $B_{n,p}$ is too small – it will take a large number of small-valued candidates to approach the objective. A reasonable rule of thumb is to require $B_{n,p}$ to be greater than some user-specified tolerance, such that the final candidate eigenvalues satisfy

$$\delta_{\mathrm{tol}} \leq B_{n,p} \leq -\tilde{k}_{\max}\, e_{n,obj}\,. \tag{113}$$

This permits one to ignore impractically small eigenvalue contributions. Associated eigenvalues can be weighted if necessary, since they do not affect the outcome. Eigenvalues smaller than $\delta_{\mathrm{tol}} \approx -e_{n,obj}/3$ are not typically practical to use for optimization.

Should one decide to use loss as a way to encourage optimization, they could (in principle) achieve the objective perfectly at the pole location(s) via

$$\mathrm{Re}\left\{\frac{\left[\boldsymbol{\gamma}_n\left(k_0;\boldsymbol{\varepsilon}_t\right)\right]_p\sqrt{-\mathrm{Re}\left\{\lambda_p w_{\lambda,p}\right\}}}{j\,\mathrm{Im}\left\{\lambda_p w_{\lambda,p}\right\}\sqrt{}}\right\}=e_{n,obj}, \tag{114}$$

assuming separation of poles in frequency, such that

$$\begin{aligned} e_{n,obj} &= \frac{\mathrm{Im}\left\{\left[\boldsymbol{\gamma}_n\left(k_0;\boldsymbol{\varepsilon}_t\right)\right]_p\right\}\sqrt{-\mathrm{Re}\left\{\lambda_p\right\}\mathrm{Re}\left\{w_{\lambda,p}\right\}+\mathrm{Im}\left\{\lambda_p\right\}\mathrm{Im}\left\{w_{\lambda,p}\right\}}}{\mathrm{Im}\left\{\lambda_p\right\}\mathrm{Re}\left\{w_{\lambda,p}\right\}+\mathrm{Re}\left\{\lambda_p\right\}\mathrm{Im}\left\{w_{\lambda,p}\right\}} \\ &\approx \frac{\mathrm{Im}\left\{\left[\boldsymbol{\gamma}_n\left(k_0;\boldsymbol{\varepsilon}_t\right)\right]_p\right\}\sqrt{-\mathrm{Re}\left\{\lambda_p\right\}\mathrm{Re}\left\{w_{\lambda,p}\right\}}}{\mathrm{Im}\left\{\lambda_p\right\}\mathrm{Re}\left\{w_{\lambda,p}\right\}+\mathrm{Re}\left\{\lambda_p\right\}\mathrm{Im}\left\{w_{\lambda,p}\right\}} \end{aligned}. \tag{115}$$

The approximation assumes only small losses will be introduced and maintained. From this, the desired lossy component of the eigenvalue weighting as is solved via

$$\mathrm{Im}\left\{w_{\lambda,p}\right\}\approx\frac{\mathrm{Im}\left\{\left[\boldsymbol{\gamma}_n\left(k_0;\boldsymbol{\varepsilon}_t\right)\right]_p\right\}}{e_{n,obj}}\sqrt{\frac{\mathrm{Re}\left\{w_{\lambda,p}\right\}}{-\mathrm{Re}\left\{\lambda_p\right\}}}-\frac{\mathrm{Im}\left\{\lambda_p\right\}\mathrm{Re}\left\{w_{\lambda,p}\right\}}{\mathrm{Re}\left\{\lambda_p\right\}}. \tag{116}$$

Since this magnitude is highly sensitive to loss, it can be expected that the solution to the lossy weight component will remain small.

5.5 Integration of the Eigendecomposition Function

The wideband system according to Equation (107) can be examined in the average (versus frequency), by integrating the sum given by

$$e_{n,obj}\left(\tilde{k},\mathbf{w}_\lambda\right)=\sum_{\eta=1}^{N}\frac{\left[\boldsymbol{\gamma}_n\left(k_0;\boldsymbol{\varepsilon}_t\right)\right]_\eta}{\lambda_\eta w_{\lambda,\eta}\tilde{k}^{-1}+\tilde{k}}, \tag{117}$$

over the band $\tilde{k}\in\left[\tilde{k}_1,\tilde{k}_2\right]$. This becomes

$$\begin{aligned}\overline{e_{n,obj}\left(\Delta\boldsymbol{\lambda};\tilde{k}_1,\tilde{k}_2\right)} &\equiv \frac{1}{\tilde{k}_2-\tilde{k}_1}\int_{\tilde{k}_1}^{\tilde{k}_2}\left[\sum_{\eta=1}^{N}\frac{\left[\boldsymbol{\gamma}_n\left(k_0;\boldsymbol{\varepsilon}_t\right)\right]_\eta}{\lambda_\eta w_{\lambda,\eta}\tilde{k}^{-1}+\tilde{k}}\right]d\tilde{k} \\ &= \frac{1}{\tilde{k}_2-\tilde{k}_1}\sum_{\eta=1}^{N}\frac{\left[\boldsymbol{\gamma}_n\left(k_0;\boldsymbol{\varepsilon}_t\right)\right]_\eta}{2}\ln\left[\frac{\lambda_\eta w_{\lambda,\eta}+\tilde{k}_2^2}{\lambda_\eta w_{\lambda,\eta}+\tilde{k}_1^2}\right]\end{aligned}, \tag{118}$$

such that

$$e^{\overline{e_{n,obj}\left(\mathbf{w}_\lambda;\tilde{k}_1,\tilde{k}_2\right)}} = \prod_{\eta=1}^{N}\left[\frac{\lambda_\eta w_{\lambda,\eta}+\tilde{k}_2^2}{\lambda_\eta w_{\lambda,\eta}+\tilde{k}_1^2}\right]^{\frac{\left[\boldsymbol{\gamma}_n\left(k_0;\boldsymbol{\varepsilon}_t\right)\right]_\eta}{2\left(\tilde{k}_2-\tilde{k}_1\right)}}. \tag{119}$$

As long as the system contains some losses, the above result is well-conditioned. As before, a truly lossless system will contain infinite resonances, and as such will cause the integral to diverge.

One can choose the limits $\tilde{k}\in\left[\tilde{k}_1,\tilde{k}_2\right]$ arbitrarily and in combination, allowing the consideration of several realizations for a given eigendecomposition and associated eigenvalue deviation sequence. For instance, for the normalized frequency vector given by $\tilde{k}\in\left[\tilde{k}_1,\tilde{k}_2,\ldots,\tilde{k}_N\right]$, a particular objective field over the entire band can be forced to satisfy a condition such as

$$\begin{aligned}e_{n,desired} &= \overline{e_{n,obj}\left(\mathbf{w}_\lambda;\tilde{k}_1,\tilde{k}_2\right)} = \overline{e_{n,obj}\left(\mathbf{w}_\lambda;\tilde{k}_2,\tilde{k}_3\right)} \\ &= \cdots = \overline{e_{n,obj}\left(\mathbf{w}_\lambda;\tilde{k}_{N-1},\tilde{k}_N\right)} = \overline{e_{n,obj}\left(\mathbf{w}_\lambda;\tilde{k}_1,\tilde{k}_3\right)} \\ &= \overline{e_{n,obj}\left(\mathbf{w}_\lambda;\tilde{k}_2,\tilde{k}_4\right)} = \cdots = \overline{e_{n,obj}\left(\mathbf{w}_\lambda;\tilde{k}_{N-2},\tilde{k}_N\right)} \\ &= \cdots\end{aligned}, \tag{120}$$

for any combination of boundaries within the band. This is a useful tool for algorithm development when constructing a wideband approximant.

5.6 Wideband Optimization Algorithm Development

With mathematical preliminaries accomplished, users are now in a position to establish an objective function in frequency, determine the eigendecomposition of the system, choose eigenvalues to formulate the optimum, and relate that optimum back to the physical material substrate as a weighted update. The algorithm that must be developed to determine this optimum will be iterative; the eigendecomposition and the physical textured material must be self-consistent (one arises from the other). This will begin with a step-by-step example.

From the previous sections, through the eigendecomposition of the FE-BI system, and an appropriate understanding of the functional form of these associated eigenvalues, decisions can be made regarding which eigenvalues to keep, discard, or ignore altogether. Virtually without penalty, material values can be weighted by a constant to move all eigenvalues within the optimization space in a "wholesale" fashion. From there individual poles can be located (via weighting) as needed to form the wideband result. Further, since the characteristics associated with loss in the eigenvalues are well-understood, loss may be used to dampen the magnitude of contributions if absolutely necessary. The desire is to avoid introducing losses.

To illustrate, first consider the wideband solution for the geometry of Figure 5-10, with $\varepsilon_r = 100 - j0.15$ over the bandwidth 1.0 GHz to 2.0 GHz ($f_0 = 1.5\,\text{GHz}$ such that

$\tilde{k} = [0.67, 1.33]$), and its assoicated eigenvalues. A subset of total eigenvalues is shown in the figure. Note that they are labeled as to whether they aid the optimization ("Keep"), hurt the optimization ("Discard"), or can be ignored (this analysis uses $\delta_{\text{tol}} = -e_{n,obj}/3$). The category they fall in is determined from the inequality in Equation (113), where the "Discards" are those eigenvalues that produce contributions that exceed the objective.

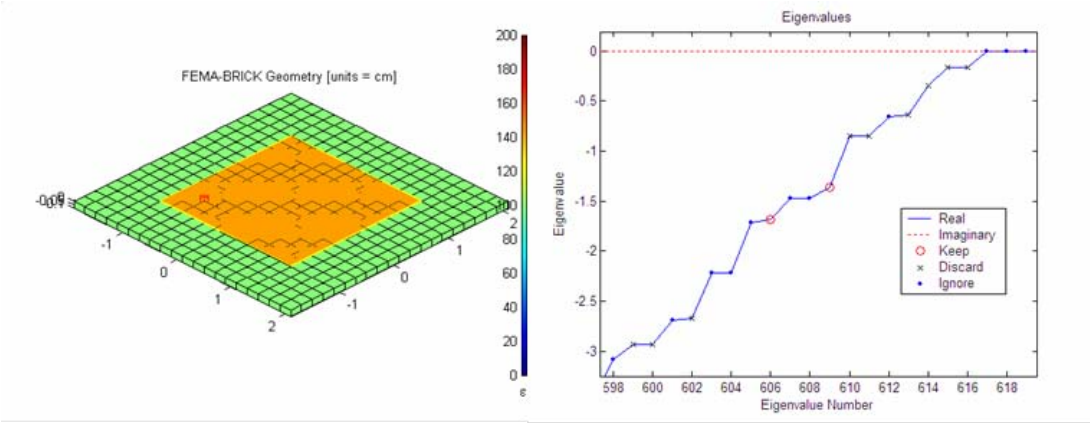

Figure 5-10. Example 4.0 cm × 4.0 cm × 0.1 cm 400 Cell Geometry (left) and Zoom View of Associated Eigenvalues (right)

The field at the probe location that results from this geometry directly is shown in Figure 5-11, along with the correspondence to eigenvalues that induce resonances. The eigenvalues labeled "Discard" are clearly associated with fields that exceed the objective (in this case, a 50 Ω input resistance corresponds to a field at -500 V/cm).

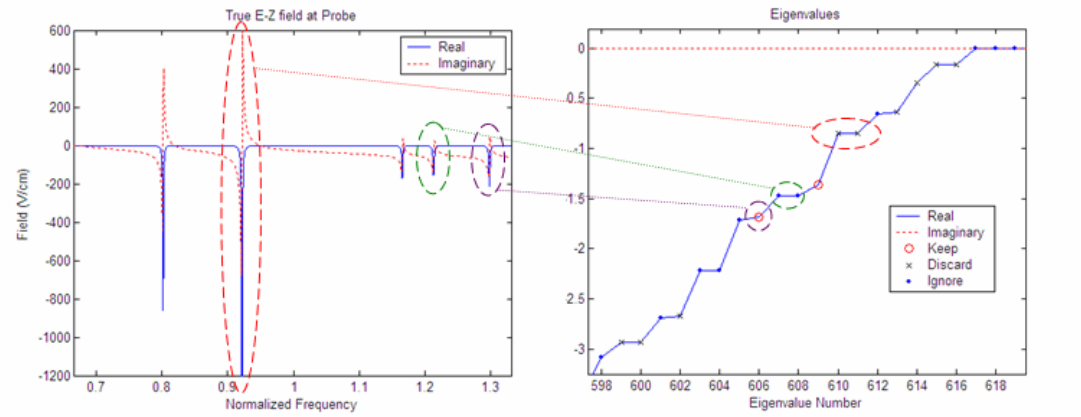

Figure 5-11. Example Geometry Probe Location Frequency Response (left) and Zoom View of Associated Eigenvalues (right) with Correspondences Shown

Next, shift the first "Keep" eigenvalue (located at $\tilde{k}_n = 1.1659$) to a normalized frequency of 0.98. The required eigenvalue weighting is given by

$$w_{\lambda,n} \approx \left(\frac{\left[\tilde{k}_n\right]_{new}}{\left[\tilde{k}_n\right]_{old}} \right)^2 = \left(\frac{0.98}{1.1659} \right)^2 = 0.7065, \qquad (121)$$

for this case, and the result is shown in Figure 5-12.

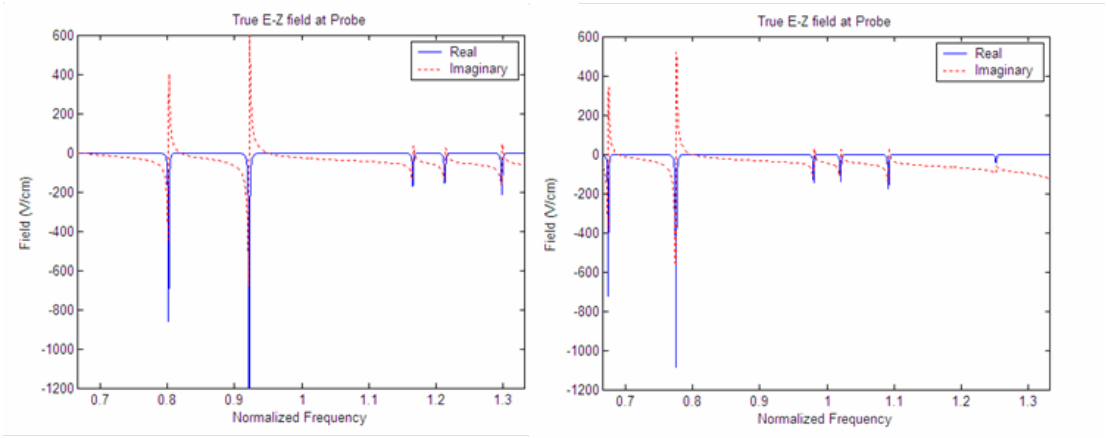

Figure 5-12. Example Geometry Probe Location Frequency Response (left) and Shifted Frequency Response after Constant Material Scaling of 1/.7065 = 1.4154 (right)

Recall from the previous section that the actual material scaling is the inverse of the eigenvalue weighting. From Equation (112), the new field values at their associated resonance locations are similarly scaled according to

$$\left[B_{n,p}\right]_{new} \approx \sqrt{w_{\lambda,n}}\left[B_{n,p}\right]_{old} = 0.8405\left[B_{n,p}\right]_{old}. \tag{122}$$

That frequency response shifts in this fashion via constant material adjustment is very well-understood, but it is interesting to note that the eigenvalues themselves dictate both the shift and the amplitude property changes. Continuing the illustration, two eigenvalues within the band of interest are adjusted next. There are two identical eigenvalues (607 and 608) in Figure 5-11 associated with the resonance now at $\tilde{k}_n = 1.0204$ (previously at $\tilde{k}_n = 1.2136$). These are separated by applying a weight of 4.1744 to point 607 and a weight of 0.1044 to point 608 (remaining eigenvalues weighted by 1.0436). These weights are chosen to bifurcate the target resonance while maintaining a consistent location relative to the center frequency.

Section 5.3 demonstrated that a specific relationship exists between the perturbation of eigenvalues and the perturbation of the textured material. By utilizing Equation (99) and inserting this into Equation (105),

$$\mathbf{w}_{\varepsilon} = \mathbf{T}_{\varepsilon}^{+}\ \mathrm{diag}\left(\mathbf{W}_{D}\right). \tag{123}$$

When the weighting derived here is applied to the material profile obtained from the previous constant weighting, the textured material profile shown in Figure 5-13 is ultimately determined.

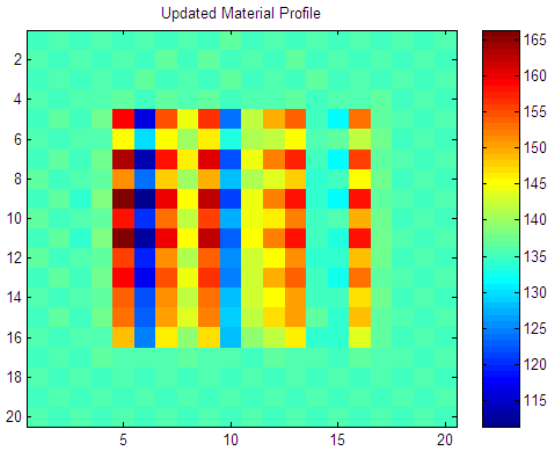

Figure 5-13. Example Derived Textured Material Permittivity Profile (real part)

This textured material results in the wideband result shown in Figure 5-14, where one can clearly observe the desired effect along with the associated eigenvalue resonances.

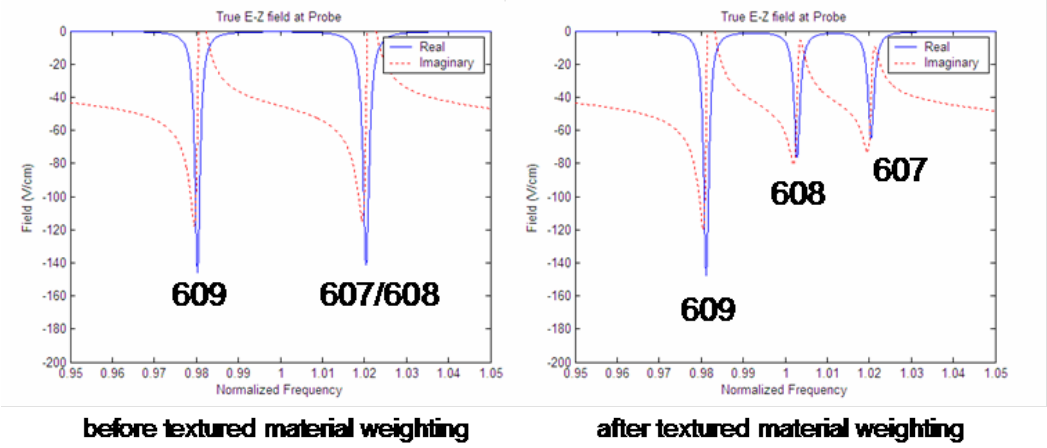

Figure 5-14. Example Bifurcated Resonance in the Frequency Response before (left) and after (right)Textured Material Weighting

We might reason that if resonances can be moved around at will, we can design any response function we choose. There is more to consider, however.

Section 3.2 showed that the stability of the solution was dependent on having an adequate mesh sample-space. Specifically, the general rule of thumb that the cell size should be

some fraction of $\lambda_g = \lambda/\sqrt{\varepsilon_r}$ was highlighted. Bearing this in mind, another key limitation involved in "moving eigenvalues around at will" is that performing this function may involve increasing permittivity. [Note in the examples above that very few candidate ("Keep") eigenvalues exist that are > -1.] For the example above, the cell sizes of 0.2 cm × 0.2 cm × 0.005 cm for the base permittivity of $\varepsilon_r = 100 - j0.15$ result in a cell size in wavelengths of $0.1\,\lambda_g \times 0.1\,\lambda_g \times 0.0025\,\lambda_g$ at the center frequency of 1.5 GHz. If the textured material is allowed to increase in value on the order of 5 times the starting point, this reduces to a cell size of $0.22\,\lambda_g \times 0.22\,\lambda_g \times 0.0056\,\lambda_g$, which begins to encroach on cell-size based accuracy limitations. For these reasons, there are not as many eigenvalues available for optimization as may first seem to be the case. If the material scale factor was limited to 3 (keep only eigenvalue terms > -3), for example, only two eligible eigenvalue terms remain, so optimization performance would be limited.

An option not yet discussed is the selection of alternative antenna geometries. The FEMA-BRICK code is capable of modeling a variety of metal structures on the surface of the substrate so long as the metal can be modeled by rectangular patches. A popular type of antenna is the spiral. The eigenvalue spectra associated with both the rectangular patch antenna and the 2-arm square spiral are quite different, as shown in Figure 5-15.

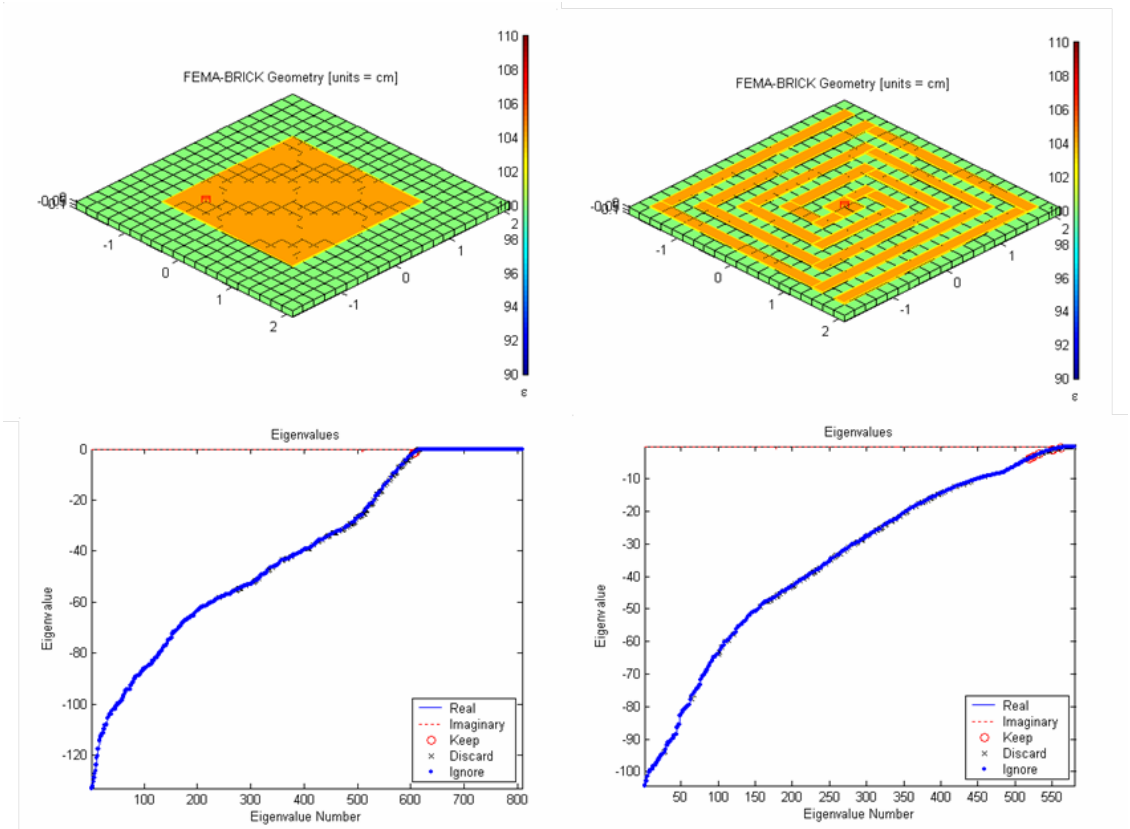

Figure 5-15. Comparison of Geometry and Corresponding Eigenvalues for the Patch Antenna (left) and Square Two-Arm Spiral (right)

Of particular interest is the nature of the eigenvalues approaching zero. For the patch antenna, there are a large number of zero eigenvalues. For the spiral, the eigenvalues approach zero much more gracefully. This is a highly desirable property for optimization, since more potential "Keep" eigen-terms are available.

The algorithm required is thus straightforward, but "human-in-the-loop" intensive. The range of eigenvalue terms that may be used is limited, and the terms that aid optimization are easily identified. In principle, the algorithm only requires a direct solution. In practice, however, iterations are required in order to arrive at the optimum, and choices

must be made along the way. The general algorithm can be described by the block diagram of Figure 5-16.

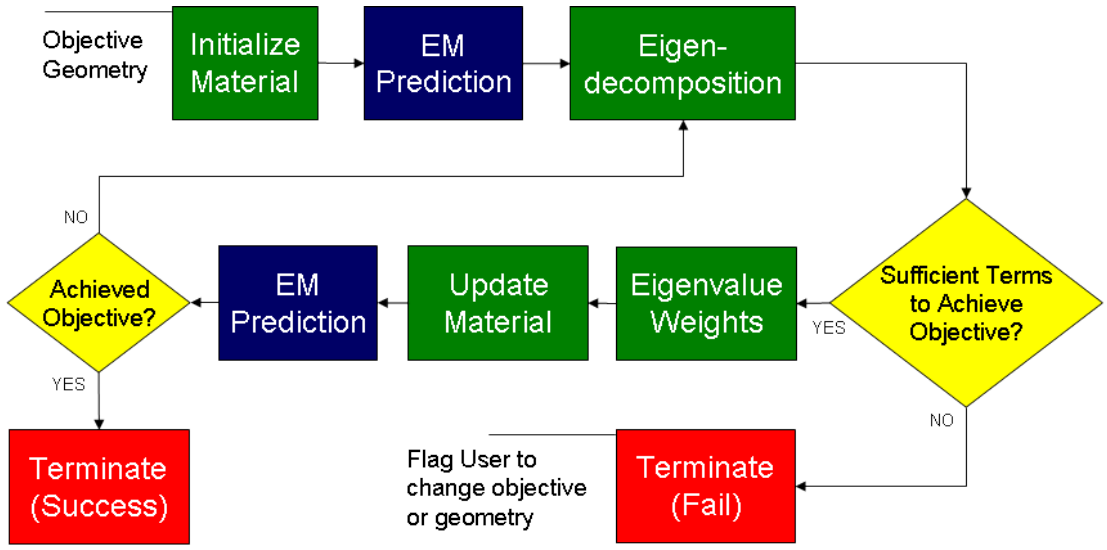

Figure 5-16. Optimization Algorithm Block Diagram

Note that this algorithm should only require a minimal number of iterations provided the eigenvalue weighting applied correctly corresponds to the effect induced by the textured material update. The choice of eigenvalue weights is one for which the user must choose between a number of eligible candidate eigenvalues (possibly requiring complex weighting; introduction of loss), or stringent material requirements. The user can decide upon a wide range of overall optimization choices.

CHAPTER 6 WIDEBAND SYSTEM OPTIMIZATION RESULTS

This chapter explores some of the choices available to designers via this new approach using specific examples. From the previous section, a textured material can be designed to target (a) specific eigenvalue(s) to arrange them in accordance with an objective. This leads to the ability to construct a wideband response. This chapter will walk through two representative examples that help to illustrate both how this is done as well as the limitations associated with it.

6.1 Wideband Optimization Case I – Simple Patch

The first example is one based on the dominant example geometry of the previous chapters: a square patch over a single-layer textured dielectric. This example geometry has a relatively small number of eigenvalues that fall within the range of usage. The example targets only four eigenvalues and attempts to adjust them near each other to form a wideband solution. The geometry and initial material substrate (constant $\varepsilon_r = 100 - j0.15$) is shown in Figure 6-1.

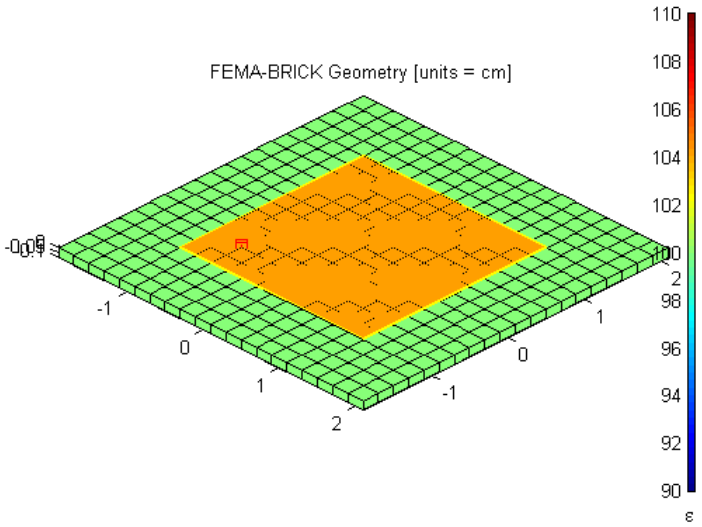

Figure 6-1. Simple Patch Antenna

The eigenvalues corresponding to this geometric design are shown in Figure 6-2. The particular eigenvalues near -1 (those closest to the center frequency) are not large in number and may be characterized by reasonably large jumps coupled with some eigenvalues that are identical (no jump).

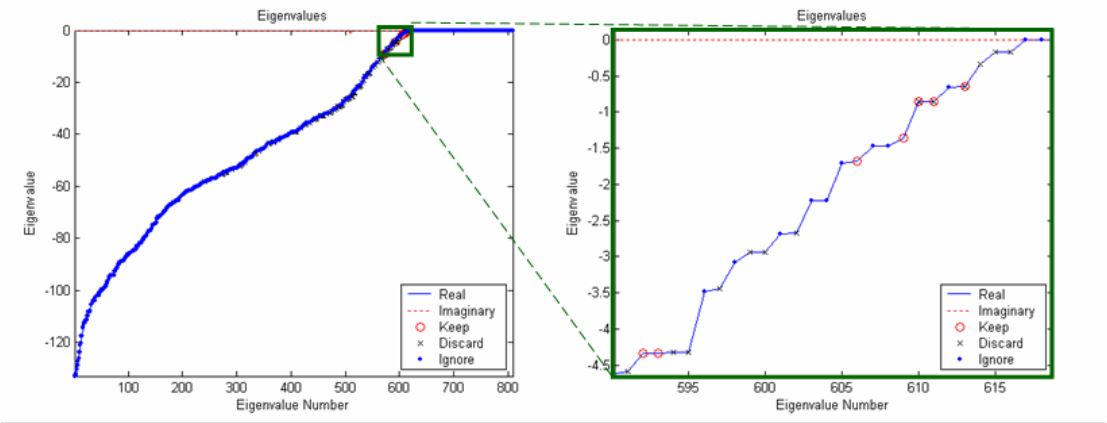

Figure 6-2. Eigenvalues Associated with Simple Patch Antenna

Identical eigenvalue situations are particularly interesting, since they are relatively easy to separate. One need only move one eigenvalue, while the other remains unweighted to

derive the material texture of interest. The response below on the right was obtained in this fashion directly (without iteration) by weighting eigenvalue number 610 and leaving its eigenvalue repeat (611) alone.

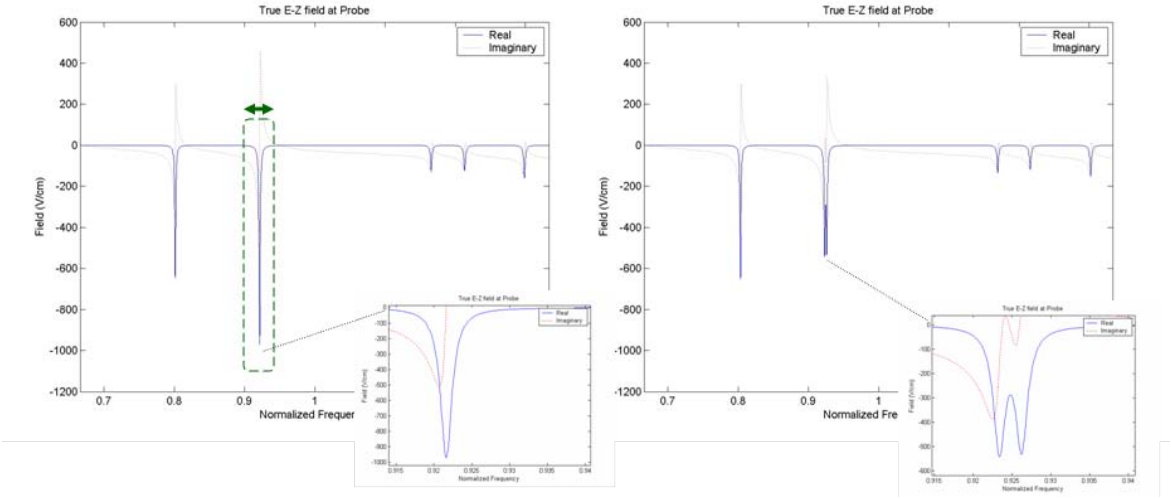

Figure 6-3. Patch Antenna Response Before (left) and After (right) Eigen-mode Separation

The material texturing that produced the desired effect above is shown in Figure 6-4, noting that relatively little contrast in material is required to obtain this as long as the texture is maximally effective. It is interesting to observe in the textured result that some apparent "channeling" or "striping" is occurring in the texture in order to obtain this desired effect. This example serves to illustrate one important quality of this new approach: that a "global" solution must necessarily be defined by the amount of material contrast required to obtain it. Since this work has shown that there are an infinite number of ways to get an identical wideband result, the best solution will be the one that produces an effective answer with the minimum required amount of material change. This approach affords the user the opportunity to evaluate a number of different regions in

which to operate via eigen-space, and make intelligent decisions with respect to weighting based on material limitations, fabrication processes, etc.

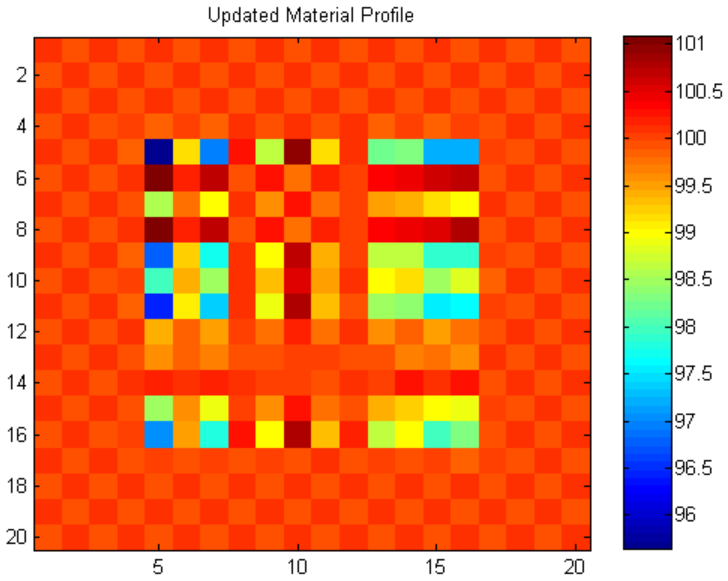

Figure 6-4. Material Texturing Leading to Eigenvalue Separation

The example next sought a material texture that would draw two resonant features together. Two resonances were chosen as shown in Figure 6-5, and a constant weighting was applied in order to shift these resonances about the center frequency. Texturing was incorporated to draw the two resonances toward the center frequency. The result in the image on the right was achieved after three iterations. The material texturing that resulted in each example return is shown in Figure 6-6.

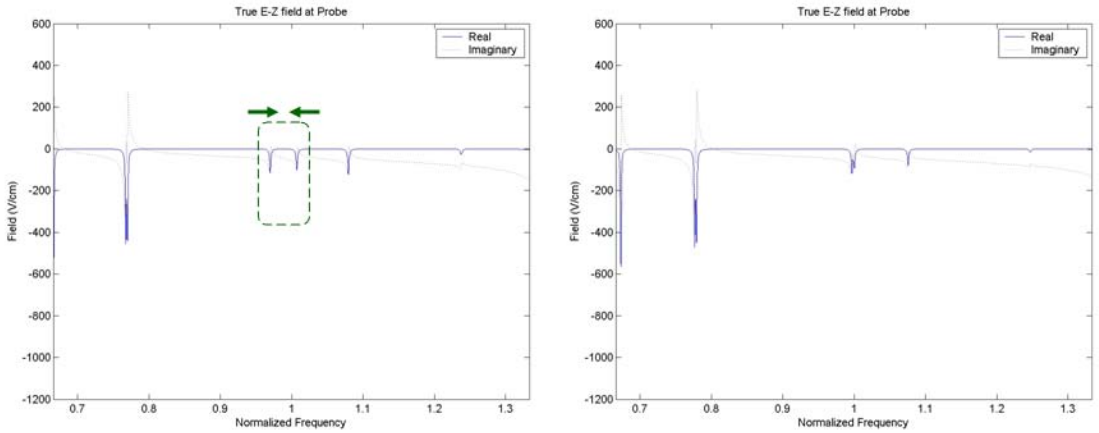

Figure 6-5. Example Showing the Closing of Two Resonances for a Simple Patch

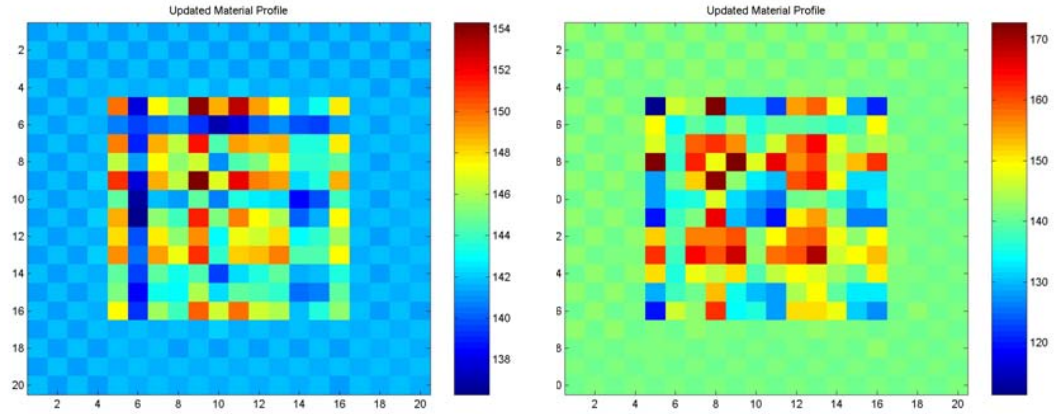

Figure 6-6. Material Texturing (Real Permittivity) Leading to the Resonance Closing Example for the Simple Patch; Intermediate State (left) and Final State (right)

This example demonstrates that even with limited availability of eigenvalue terms, some optimization can be easily achieved. The next example seeks to examine the subspace associated with the square spiral; already shown to provide improved eigenvalue diversity.

6.1.1 System Condition for the Simple Patch

Because texturing is accomplished by weighting all available substrate bricks, it is necessary to test the robustness of the FEMA-BRICK solution itself. For the case of the eigen-mode separation example (Figure 6-3 and Figure 6-4), this can be accomplished by discretizing the determined texture more finely for an alternate FEMA-BRICK solution. The example shown in Figure 6-7 compares the solution for the 20x20 brick geometry to the alternate FEMA-BRICK solution for a 40x40 brick discretization. The solution shifts in frequency as a function of discretization as is typical, but of importance is the fact that the optimized result remains intact; the eigen-modes remain separated.

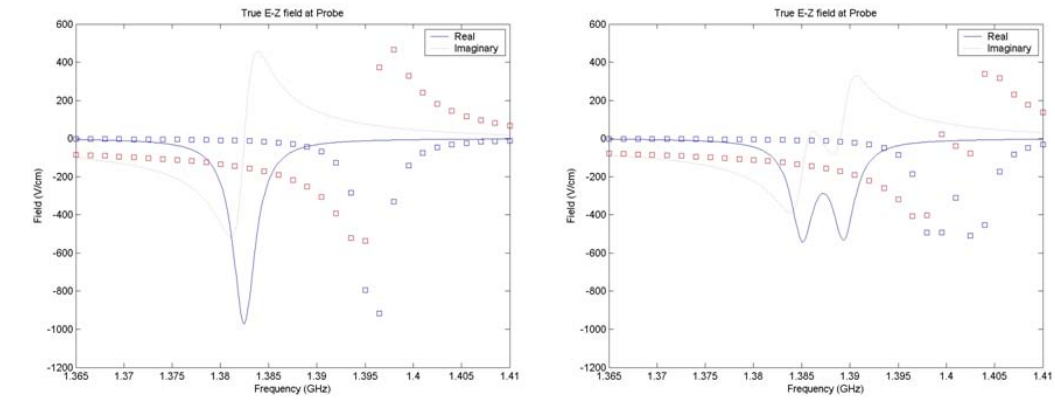

Figure 6-7. Initial (left) and Optimized (right) Simple Patch Solution using 20x20 Bricks (solid lines), and 40x40 Bricks (discrete squares)

The high-density geometry is considered the most accurate. It is important to note that small disagreements between FEMA-BRICK predictions and measurements (or other prediction techniques) may remain due to the tendency for resonances to shift as a function of discretization.

6.2 Wideband Optimization Case II – Two-arm Square Spiral

The second example is one based on a geometry previously shown to have more eigenvalue diversity in the following sense: since the eigenvalues decay away from the maximum (zero) more gradually than the simple patch, the opportunity to make use of more eigenvalues in the optimization may arise. The two-arm design is shown in Figure 6-8, with the feed at the center.

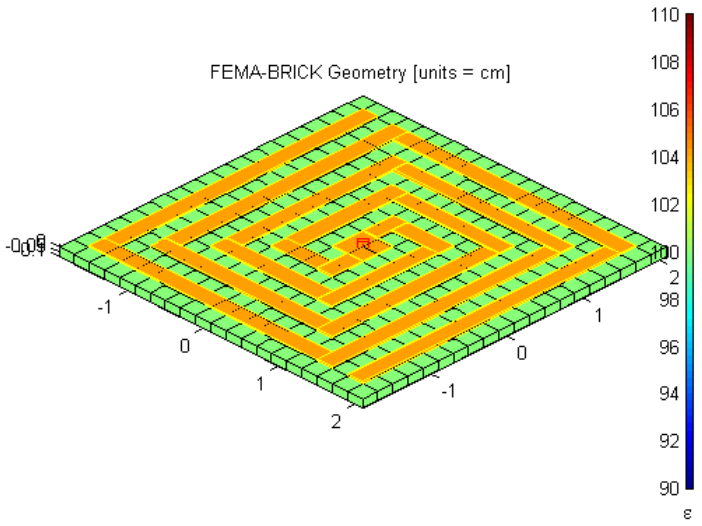

Figure 6-8. Two-arm Spiral Patch Antenna

The eigenvalues corresponding to this geometric design are shown in Figure 6-9.

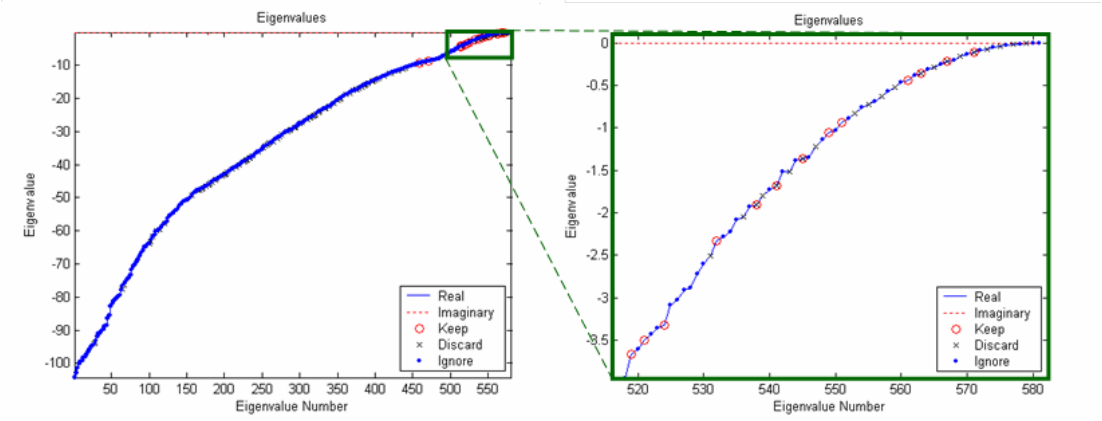

Figure 6-9. Eigenvalues Associated with the Two-arm Spiral Patch Antenna

Note the gradual fall-off of eigenvalues away from zero in this case versus the previous case. Because of the more regular spacing of eigenvalues, responses at regular intervals in the field unknown are observed at the probe location shown below in Figure 6-10.

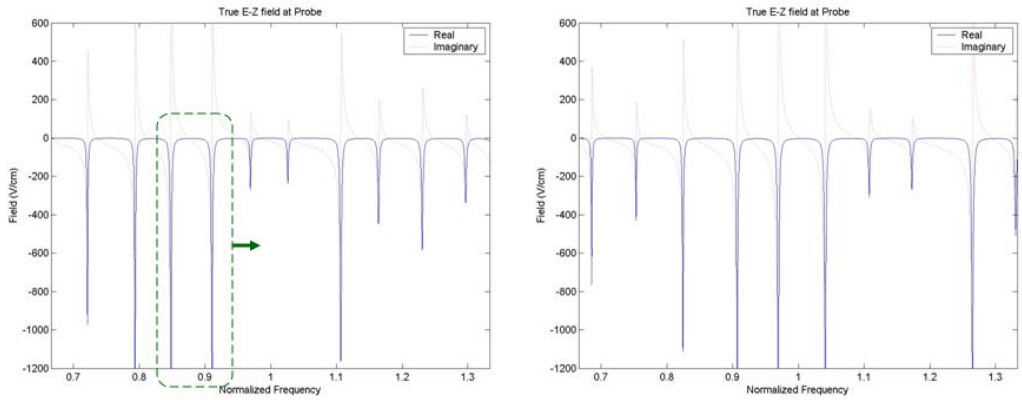

Figure 6-10. Initial Field Unknown Response Associated with Two-arm Spiral Patch Antenna

As shown in the right-side figure, resonances are moved to the right via a constant material adjustment. Next, the eigen-modes are moved closer together to form a broad-band response. This is accomplished in 12 iterations as shown in Figure 6-11 and the material texturing leading to these examples is as shown in Figure 6-12.

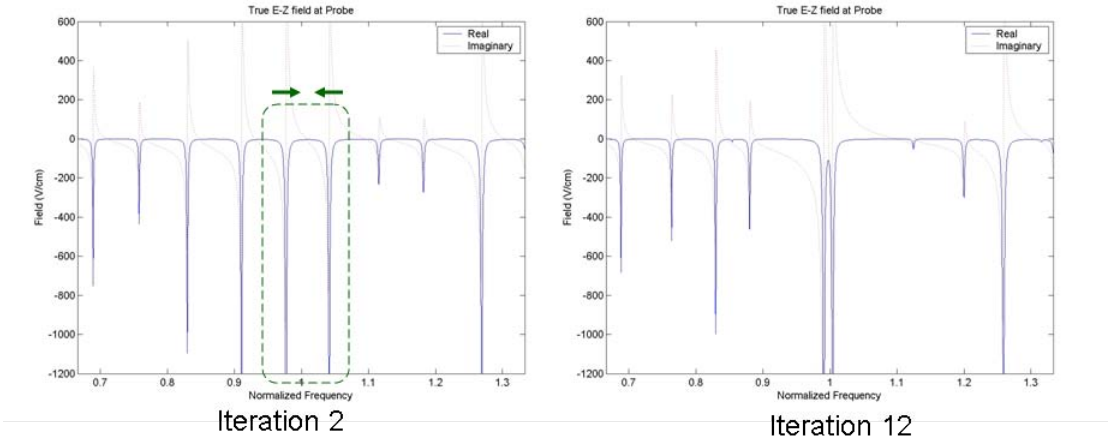

Figure 6-11. Example Showing the Closing of Two Resonances for a Square Spiral

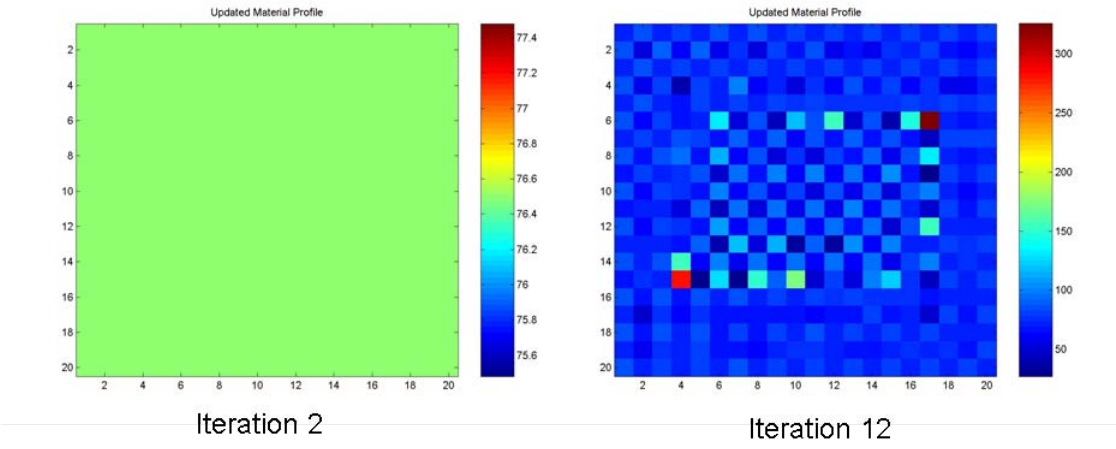

Figure 6-12. Material Texturing (Real Permittivity) Leading to the Resonance Closing Example for the Square Spiral; Intermediate State (left) and Final State (right)

The next step to demonstrate is the introduction of loss in order to better approach a particular objective. For this case, a 50 Ω input resistance corresponds to a field at -500 V/cm. A small loss is introduced by multiplying the existing substrate by the weighting $1 - j0.008$ to obtain the result shown in Figure 6-13.

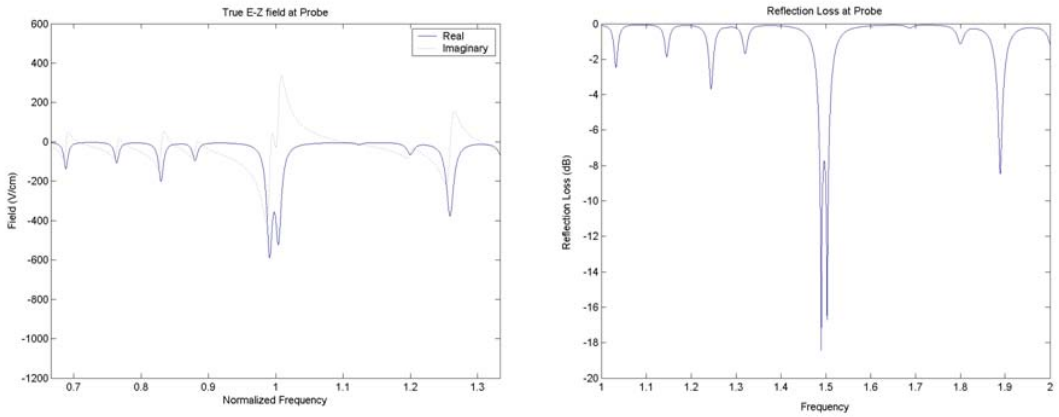

Figure 6-13. Introduction of Material Loss to Obtain Values Near the Objective (left) and Resulting Reflection Loss (right)

Clearly, to obtain an increasingly wideband response, more individual resonances must be employed and lined up in sequence. It is interesting to note in Figure 6-11 above that while the two target resonances above are squeezed together as intended, other resonances are also affected. In particular, the resonance that begins near $\tilde{k}_n \approx 0.9$ actually shifts lower in frequency, while its neighbor is moved upward toward the center frequency. In the next example, this resonance is targeted as well to move three resonances toward the center frequency as illustrated in Figure 6-14.

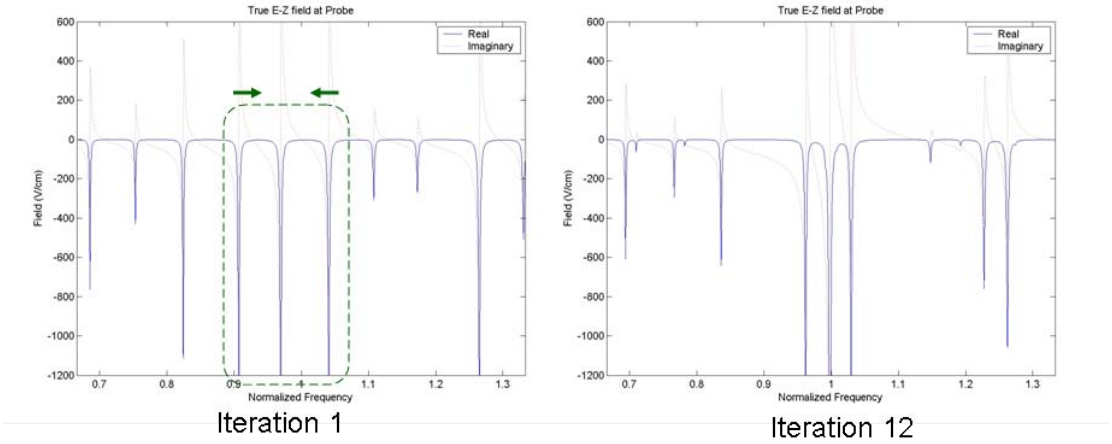

Figure 6-14. Example Showing the Closing of Three Resonances for a Square Spiral

The example shows the initial iteration on the left and iteration 12 on the right. The interesting thing about this case, however, is that the goal frequency for the lower resonance was $\tilde{k}_n \approx 0.995$, and the goal for the upper frequency was $\tilde{k}_n \approx 1.005$; not yet achieved in the example shown. Beyond iteration 12, difficulties are encountered in "squeezing" these resonances further. Increasingly large values of permittivity are called for, such that the condition of the system may be called into question. The E-field unknown at the probe location is next given below in Figure 6-15, starting with iteration 13 and ending with iteration 30.

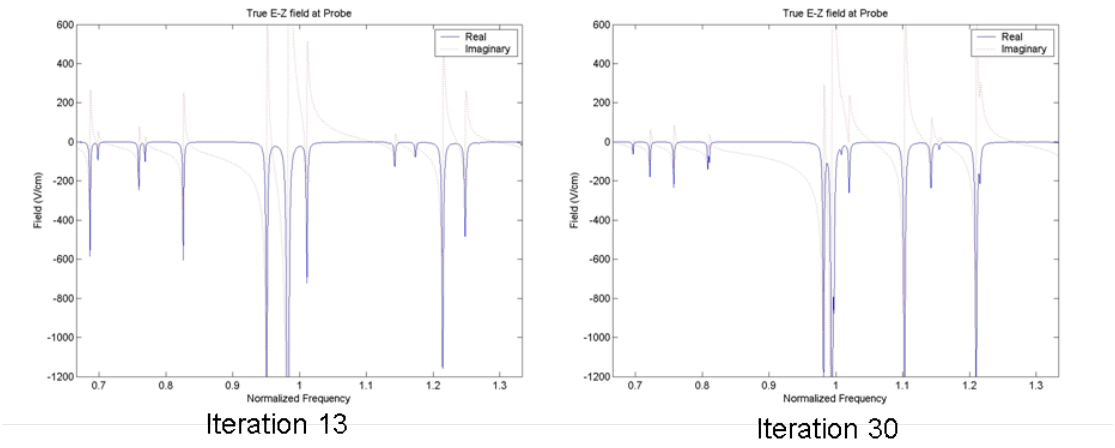

Figure 6-15. Example Showing Additional Attempts to Achieve a Difficult Objective

The E-field unknown is beginning to appear more spurious at iteration 13 (left) and is quite spurious by iteration 30 (right). The reason for this is evident by observing that the desired texturing for iteration 12 (the last "reasonable" iteration) and iteration 30 in Figure 6-16.

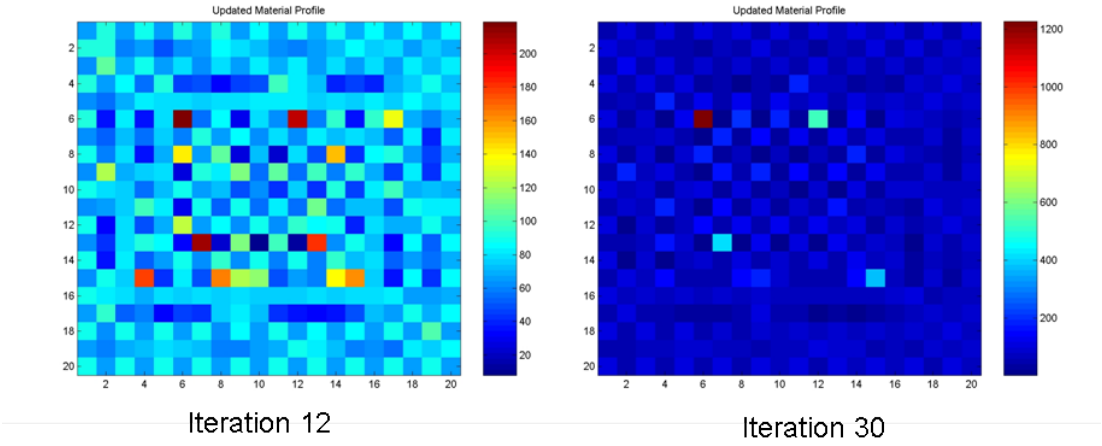

Figure 6-16. Material Texturing (Real Permittivity) Leading to the Errant Resonance Closing Example for the Square Spiral; Intermediate State (left) and Final (Errant) State (right)

Clearly there is a limit to the amount of subspace optimization that can reasonably be obtained due to the need for increasingly large material values. When such large values are introduced, the system becomes poorly conditioned.

It is anticipated that a design tool could be developed based on the work in this dissertation, but consideration of "human-in-the-loop" decision-making is likely to play a large role. Desired objectives can quickly lead to untenable textured substrate situations, and the human is required to intervene when this occurs. An easy-to-understand graphical user interface (GUI) would have to be developed to enable this process. The examples shown in this chapter have attempted to illustrate some of the considerations that a GUI designer would need to employ.

6.2.1 System Condition for the Two-arm Square Spiral

Because of the nature of the metal surface for the square spiral and the chosen mesh discretization, it was prudent to examine the system for different geometries and code formulations to ensure the robustness of the solution. Consider the example of two

identical geometries that have been constructed differently by a factor. The geometries are shown in Figure 6-17, where one has been subdivided into 20 segments per edge and the other has been subdivided into 40. The substrate is of size 4.0 cm × 4.0 cm × 0.1 cm and has value $\varepsilon_r = 100 - j0.15$, and the probe location E-field unknown from 1-2 GHz is investigated.

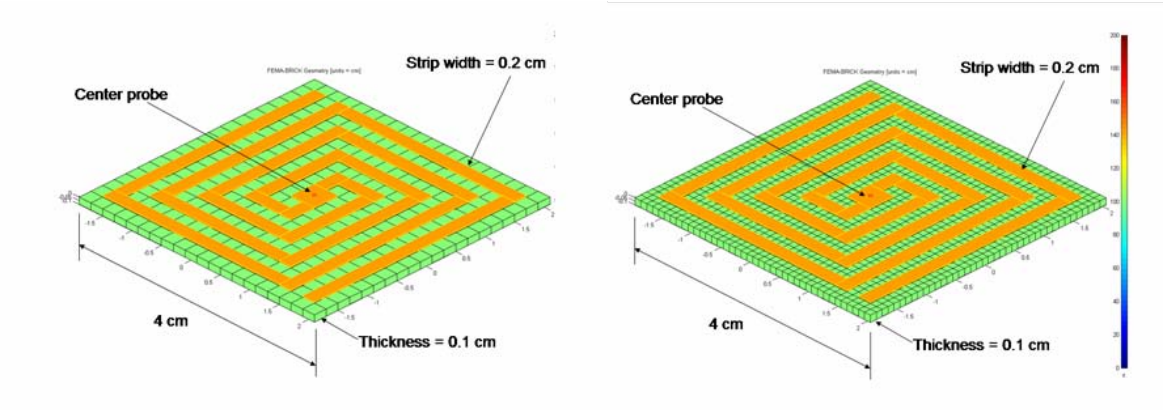

Figure 6-17. Identical Geometry Constructed using 20x20 Bricks (left), and 40x40 Bricks (right)

The respective input impedance (proportional to the Z-directed E-field calculated at the probe location) for each case is shown in Figure 3-7 and is compared to a generalized Surface Integral Equation (SIE) using the Poggio, Miller, Chang, Harrington, Wu, and Tsai (PMCHWT) formulation. The high-density geometry is the most accurate. Observe that higher-density solution is converging toward the SIE solution, as expected.

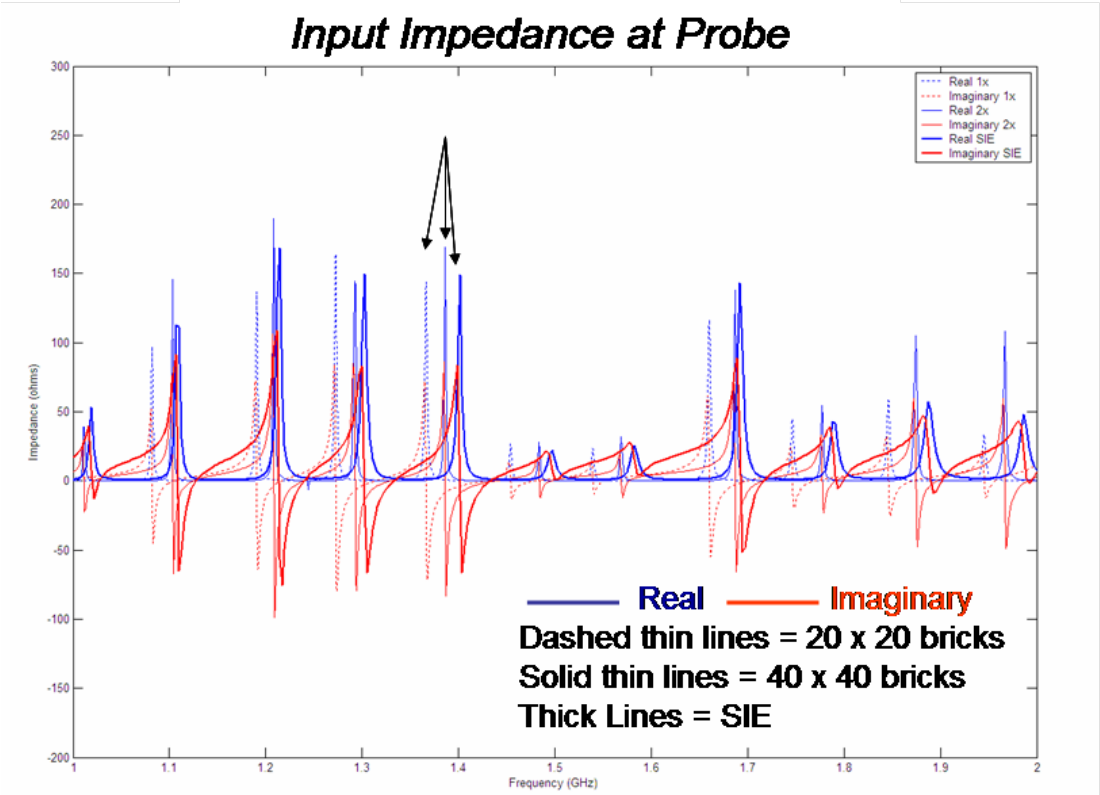

Figure 6-18. Input Impedance for 20x20 Bricks (dashed thin), 40x40 Bricks (solid thin), and SIE Formulation (thick) Shows Convergence of Solution for $\varepsilon_r = 100 - j0.15$

Results show a slightly lower Q (less "peaky" resonance) for the SIE formulation versus the FEMA-BRICK solutions, owing to the fact that the SIE formulation is not performed in the presence of an infinite ground plane.

CHAPTER 7 CONCLUSIONS

This work has demonstrated that electromagnetic optimization is improved by utilizing information inherent to a specific subspace of the electromagnetic system. Specifically, a solution to the optimization of an FE-BI system has been found via eigendecomposition and eigen-mode adjustment. The FE-BI system is among the most general of electromagnetic systems since it combines both finite element and method of moments approaches, making it an ideal choice for this type of work.

This new optimization method is a dramatic advance relative to existing approaches which typically fall into two categories: a) *gradient-based* approaches such as steepest descent or conjugate gradient that are predominantly *local* solutions, and b) *gradient-free* statistical approaches such as the genetic algorithm and simulated annealing that are potentially *global* solutions, but can be extremely time-consuming. This new approach locates eigen-modes in a specified manner to produce an optimal solution that minimally impacts the existing substrate. This solution may be thought of as global in the sense that it is the best solution obtainable with minimal material deviation.

At present, gradient-free statistical optimization approaches (e.g., GA and SA) garner a large amount of research attention owing to their very general applicability. Utilizing intrinsic electromagnetic system information requires a very specific focus and is not as

easily extensible, but the benefits are worth the extra effort, as demonstrated. The following sections briefly highlight the findings and results and provide some suggestions for future research topics.

7.1 Summary of Findings and Results

This work has demonstrated, for the first time, that non-parametric optimization of a textured metamaterial substrate is feasible. A number of important contributions to the field of electromagnetic optimization have been involved in achieving this goal:

- *an operable electromagnetic (eigen-mode) subspace was determined for FE-BI*
- *a (near) instantaneous wideband system solution was demonstrated*
- *modification of eigenvalues in the system subspace was shown to lead to textured material solutions*
- *functionality of eigenvalues to include combined frequency-dependence and material-dependence was demonstrated*

An early key aspect of this work was in determining a subspace in which to enable an iteration mechanism that was maximally effective in finding a textured material update. Since a wideband objective is the goal, it was critical to determine a wideband functional form that could be critically analyzed. In the past, with complete dependence on the electromagnetic engine itself, obtaining properly sampled wideband responses was extremely time-consuming. By carefully analyzing the Green's function associated with boundary integral terms in close proximity, a quadratic representation of the FE-BI system was determined. This led to an eigendecomposition with a convenient functional form: one highly amenable to the type of optimization sought.

This work demonstrated that the frequency-based functional form of the eigenvalues matched extremely well with the actual FEMA-BRICK prediction engine results and

facilitated the computation of results in orders of magnitude less time (~ 50,000 times faster). This was a fortuitous result, but the insight associated with the eigenvalue behavior was the key which ultimately led to an improved optimization paradigm; the intent of this dissertation.

Following a complete mathematical development of the result, example results were shown for the case of a simple patch antenna and a two-arm square-spiral patch. One interesting development was that the eigenvalue behavior was markedly different between these two different cases. This alone helped to explain the popularity of spiral antennas for wideband applications.

7.2 Evaluation of Findings and Results

It was expected that certain elements of the optimization tradespace would prove problematic. Consistent with past related work, achieving wideband solutions involving more than two resonances is difficult, particularly when a local optimum is sought. As a case in point, past work in the area (discussed in Section 1.2) did succeed in designing, constructing, and testing a local solution involve two resonances (see Figure 1-5). This work showed that an arbitrary number of resonances could be led toward achieving a particular wideband objective, but user involvement (or sophisticated programming) would be required to ensure that a particular solution did not iterate toward material values that lead to a poorly conditioned system. Such findings were not generally unexpected, but with the insight afforded by this new approach, a user could easily begin to seek more amenable geometries (with infinite possibilities) and/or regions in eigen-space in which to best operate.

Returning again to the result highlighted during the introduction (Figure 7-1 below), one can understand this result in the context of the results in this dissertation as the *"drawing together" or "pushing apart" of two eigenvalue resonances*. It may be possible that a simpler design can achieve the same end-goal, but it must be constructed (as this was) via realizable materials.

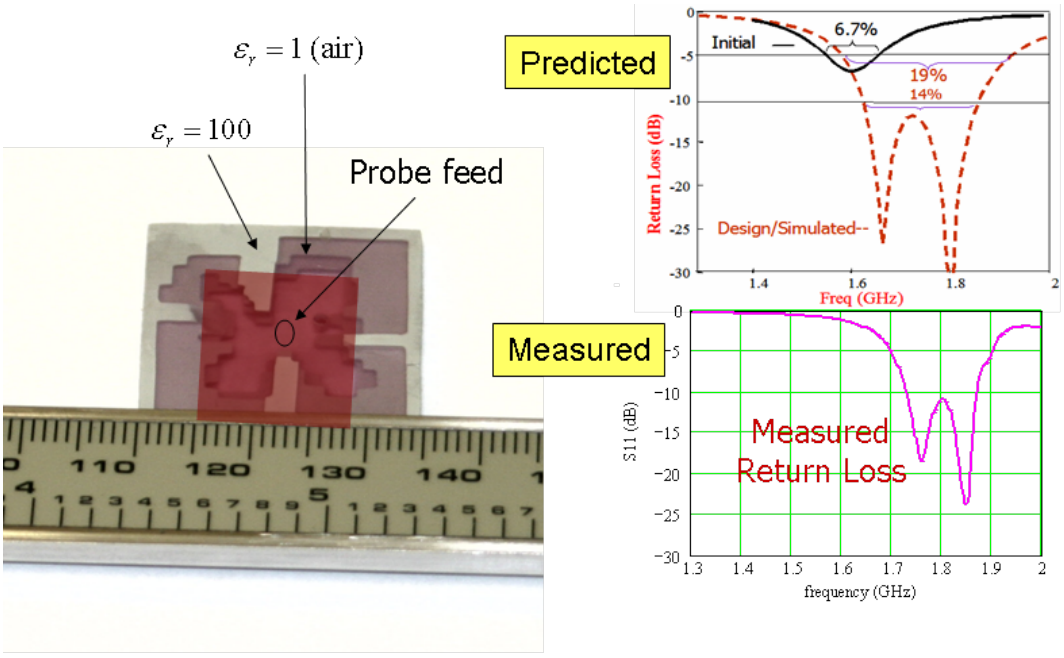

Figure 7-1. Example of a High-Contrast Textured Material Optimization (results in [18, 20])

7.3 Suggestions for Future Research

This work has made available and demonstrated a fundamental insight with respect to the nature of FE-BI–related eigenvalues. The functional form of the eigenvalues themselves can (and will) change as a function of both geometry and material texturing. For demonstration purposes, only optimizations based on material texturing were pursued, as

that was the intent of this dissertation, but many more possibilities remain. By way of a listing, the following topics rise to the top for future research pursuits:

- *Optimization of Geometry*
- *Constrained Optimization of Material*
- *Design of Exotic Materials*
- *Management of Large Systems*
- *Revisit the Total Least Squares Analogy in Eigendecomposition*
- *Application of Equivalent Techniques to other Electromagnetic Problems*

Clearly, changes in the geometry of the patch itself can drastically affect the placement and magnitude of the individual eigenvalues. One could investigate limited parametric cases to develop eigen-mode subspace insight for various patch geometries and feed placements. It may also be possible to find a direct means to encourage optimal surface patch design in much the same way as the textured substrate was derived for this work.

Advances in material geometry now provide a vast assortment of choices with which to design textured substrates. For higher permittivity values, typically ceramics or ceramic composites are the only applicable materials. Specific ceramics are advertised as offering values over a wide range (examples can be found on the Ferro website, for the range $\varepsilon_r \in [10,18000]$ [42]), and particular expertise is required to ensure compatibility amongst material choices. Ceramics can be of a Class I, II, or III dielectric category and can be low- or high-temperature fired, making compatibility a large concern. Two of the future tasks mentioned above work hand-in-hand in this respect. The design of exotic materials is a research topic for materials science experts. These experts must work together with electromagnetic optimization experts to constrain the optimization updates

to be within the limits of available materials. This work did not consider the constraints associated with realizable materials.

To make this technique practical for ever-increasing problem sizes, some means for determining the eigendecomposition in an efficient fashion should be formulated. This could happen in two ways: 1) making efficient use of well-known eigendecomposition update schemes, thus avoiding a complete eigendecomposition with each update, and 2) direct generation of the eigendecomposition. The first approach is relatively straightforward. The second is by far the most interesting. It has been suggested that it may be possible to directly generate the eigendecomposition in the same basic amount of time required to generate the FE-BI system. This would be the superior choice if it were possible.

There are a number of advantages to the use of Total Least Squares (TLS) in optimization problems where uncertainty may exist in the electromagnetic system, the materials themselves, or the measurement approach. It has been suggested that the TLS analogy in eigendecomposition would be to formulate the variational problem as a *minimax* solution. This would require paying careful attention to the resultant structure of the variation, since the structured update must lead directly to a material update.

Finally, techniques such as those developed for this work should be applied to fundamentally different electromagnetic systems. The choice of the FE-BI system for this work was thought to be a great starting point, due to the broad applicability and increased acceptance of FE-BI for solving difficult electromagnetic problems. Similar decompositions for other systems should be found; at the same time determining the

general applicability of the quadratic frequency system approximation for other systems would be of great interest.

APPENDICES

Appendix A: Standard Global Optimizer Approaches and Results

This appendix examines the use of Genetic Algorithms (GA) and Simulated Annealing (SA) for optimization of the chosen application. Before beginning electromagnetic optimization, however, it was first necessary to understand the capabilities and limitations of the search algorithms themselves. Several examples exist in the published literature where GA and SA are compared for the purpose of choosing an appropriate optimization scheme, but few comparisons carefully examine the dependence on several parameters. Since the search space in question for this work has (potentially) a large number of parameters, it was necessary to study the effects of increasing the total number of parameters in a systematic way. To accomplish this, an objective function was selected that is similar in form to the objective function of interest (non-linear, multi-modal), but is computed very quickly and for which the optimum solution is known. Initially, each algorithm was examined using a simple objective function

$$J[\boldsymbol{\alpha}] = \prod_{i=1}^{N} \left| \frac{\sin[\pi(\alpha_i - 5)]}{[\pi(\alpha_i - 5)]} \right|^{-1/N}, \tag{124}$$

where $\boldsymbol{\alpha} = [\alpha_1, \alpha_2, \ldots, \alpha_N]$ is the parameter set. A plot of the objective function for $N = 1$ is shown in Figure A-.

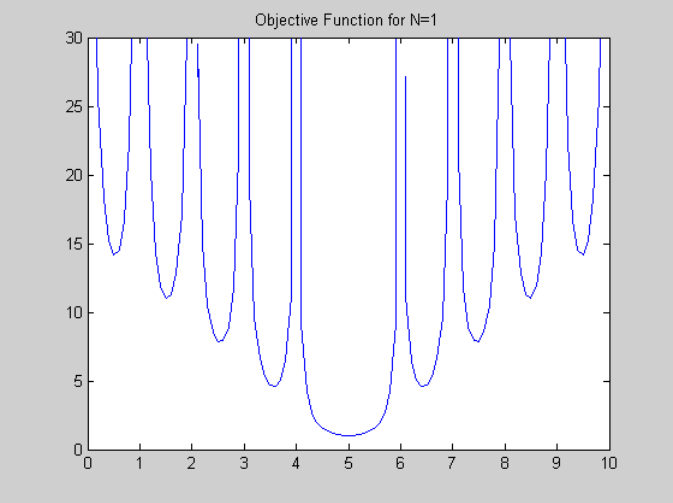

Figure A-1. Objective Function used for Optimization Algorithm Evaluations

This parametric function is similar in form to the objective function of interest and is quickly evaluated. It is clearly multi-modal, having a minimum value of unity at $\alpha_i = 5$ for $i = 1, \ldots, N$. The bounds established for the search scheme for both GA and SA are $\alpha_i \in [0, 10]$. By conducting a test for statistical performance in this way, a reasonable number of parameters for general cases may be established given the timeline required for each objective function evaluation.

The SA and GA approaches share several common traits. They are both based on fundamentally physical processes. They are both referred to as "gradient free" in that the search is not based on the local gradient of the objective function at a given location or realization. [Indeed, from Figure A- above it is clear that a gradient-based approach would fail.] They are both statistical in nature. Other approaches exist that match this criteria. An example is an increasingly popular (in the electromagnetic community) optimization scheme known as Ant Colony Optimization (ACO) [11], also based on physical processes that are gradient free, and statistical.

Finally, note that comparison of these techniques and others over a common framework is generally difficult. A termination criterion is a subjective matter in either case, but since GA optimization may be characterized by long periods of stagnation followed by rapid improvements (discussed later), a reasonable criterion for termination is particularly difficult. In this study, a maximum number of GA iterations was often established. To determine performance, the algorithm was terminated when the total cost function approached the theoretical minimum cost to within a specified tolerance. The SA algorithm uses a termination approach that qualifies the solution based on a specified number of sequential temperature reductions that have not realized a more optimal cost to within a specified tolerance. This criterion was more stringent than that used for GA (even though the tolerance was the same), so the comparison was somewhat skewed in favor of GA. These results are summarized in the following sections.

A.1 Introduction to Genetic Algorithms

Genetic algorithm (GA) optimization hinges on the notion of "survival of the fittest" and works by considering for "mating" only those parameter sets that are of certain strength in the space of the objective function. Objective function cost for a given parameter set is inversely proportional to the strength of the set. Objective function parameters are typically coded in a binary sequence ("gene") that can be combined with other binary sequences to form an overall set of binary sequences ("chromosome") that contains all parameters under observation. The mating process is simply a matter of splitting two strong chromosomes ("parents"), and forming two new chromosomes (children) with paired sets of the original parents. Periodic perturbations ("mutations") are induced to

randomly explore the strength of other sequence sets. Not surprisingly, GA optimization settles for significant amounts of iteration time on the same parameter set, where a great deal of "inbreeding" occurs between the strongest chromosomes only. It is the mutations that ultimately make the set stronger (a fact which can be used to enhance GA performance). When a significant mutation occurs, other strong parametric combinations are quickly found. For this reason, GA may be characterized by long periods of stagnation and rapid improvements. The positive outcome for this case (expensive objective functions) is that there is no need to recalculate objective functions during periods of stagnation. For this reason alone, GA quickly emerges as an optimization approach of choice that has been afforded significant attention in the electromagnetic community. An excellent introduction to GA applications in electromagnetic is found in [30]; this is the approach utilized for this work.

A GA block diagram is shown in Figure A-2. Note that many options exist for GA conditioning: number of encoded bits, number of chromosomes, number of sorting iterations, and strength criteria, among others. For this work, parameters were encoded over their bounds based on a 32 bit encoding scheme. Ranking and mating was accomplished after 32 objective function evaluations. Parents selected for breeding were the top 50% in strength. Mutation was performed by randomly selecting a bit in a random chromosome for reversal during each rank ordering and mating sequence. The figure below shows the initial selection of a vector of chromosomes ($\boldsymbol{\alpha}^{(k)}$ for $k = 0$), and the manner in which objective functions are ranked and selected for breeding. The exit criterion is not well defined in the case of GA. This work adopted the notion of waiting

for a specified period of stagnation before terminating. Results below show the number of sorting iterations (each sorting iteration represents 32 objective function operations in this case) required for a successful solution of the objective function of Equation (124) above.

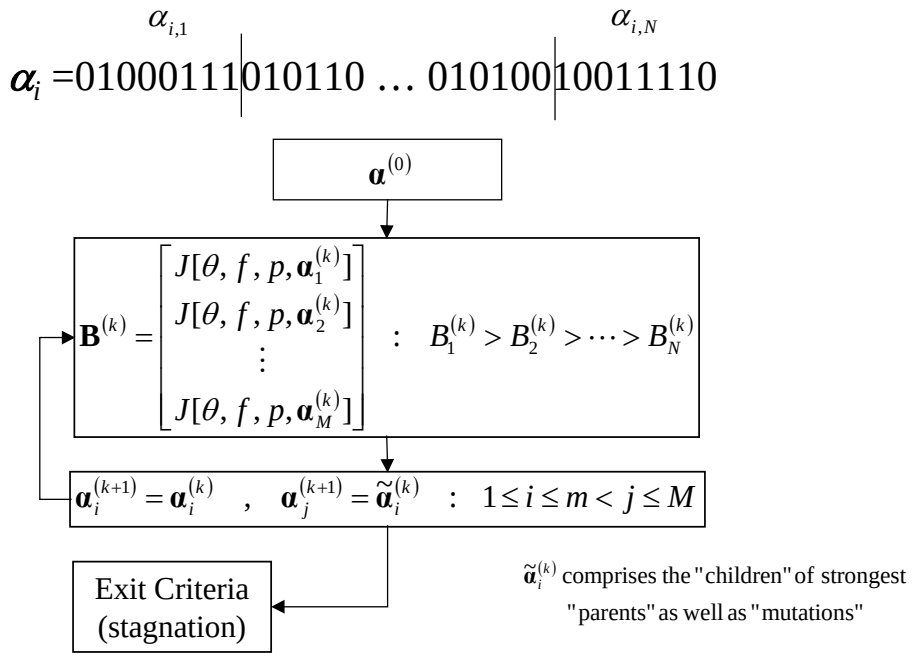

Figure A-2. Block Diagram of Genetic Algorithm Implementation

The objective function of Equation (124) was used to evaluate GA optimization for N=1 up to N=10 parameters. The optimization was terminated, and resulting number of objective function calculations recorded, when the true global minimum was achieved to within the specified tolerance factor (contained in the legend). These tolerance factors do not represent an acceptance of minima other than the global minimum for this particular objective function (see Figure A-), which explains why the variation in estimates among tolerance factors is relatively low.

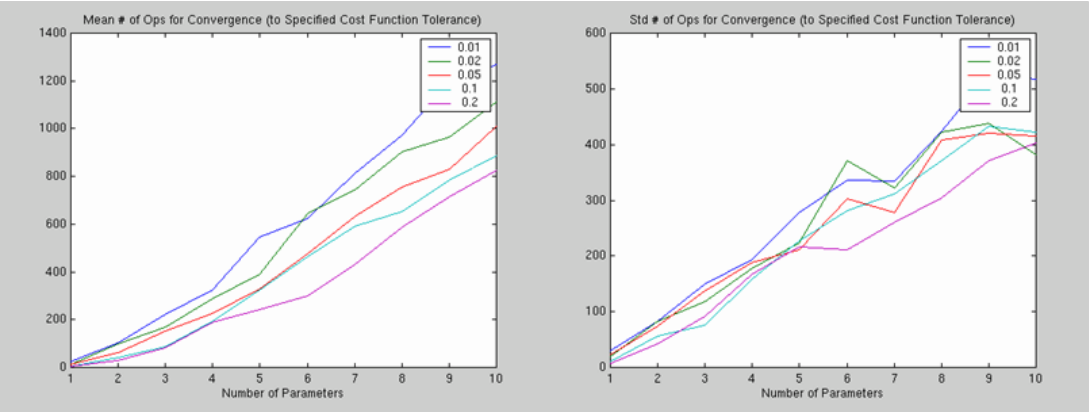

Figure A-3. Performance of Genetic Algorithms versus Number of Parameters to Optimize; Required Sorting Iterations Mean (left) and Standard Deviation (right)

A plot of a typical GA convergence is shown in Figure A-4. These periods of stagnation occur while the algorithm "waits" for a strong mutation to form.

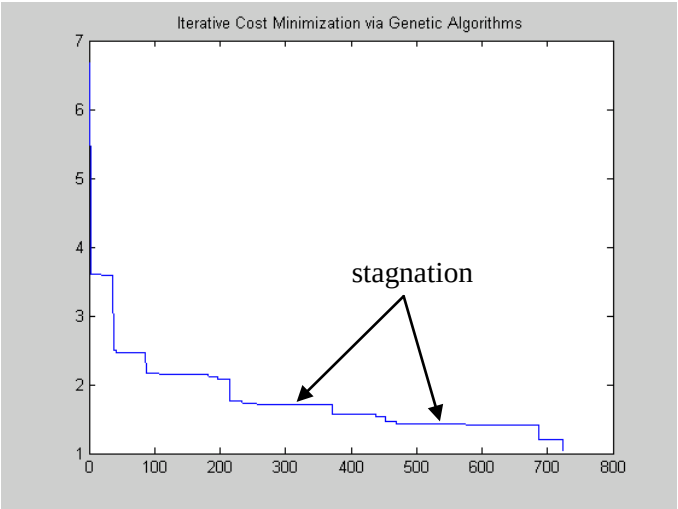

Figure A-4. Genetic Algorithm Performance as a Function of Sorting Iteration

A.2 Introduction to Simulated Annealing

Simulated Annealing (SA) is based on a physical process of cooling metal to an appropriate "ground state" after it has been melted. A proper annealing process allows metal molecules to move about randomly for a longer period, thereby encouraging more optimal crystal lattice formation in the metal solid. A fast cooling process discourages

optimal crystal lattice formation. This is sometimes desired. The process of quickly cooling metal is called *tempering*. Tempering of metal results in a harder metal, but one that has a brittle condition, more subject to breakage. Proper annealing involves establishing a reasonable schedule so that metal hardens in a less brittle state. One can always choose a very slow annealing schedule that ensures proper annealing, but does not make the best use of time. In mass-production, one seeks to optimize the trade between good annealing and a reasonable amount of time. The same principle applies here.

Unlike GA, SA does not discourage the pursuit of less promising paths for parametric optimization. The underlying principle of SA is to accept all parametric sets that realize a cost function improvement, and also accept parametric sets that do not realize an improvement with a probability given by the Metropolis criterion, $\exp\left[-\Delta/T\right]$, for Δ the change in cost function value (degree to which no improvement was realized), and T the current system temperature. As the temperature decreases, the probability of accepting parametric sets that do not show improvement also decreases.

The SA scheme is essentially a Markov process and it may be shown that the transition probability matrix associated with the Metropolis criterion ensures that the optimization converges to the global minimum with probability one. A similar proof is not available for GA, although one may conjecture that if an infinite number of GA iterations are taken, the global minimum will also be found with probability one.

The process adopted is taken from [7] (with the modification of the optimal annealing schedule taken from [33]) and is outlined in Figure A-5. Variables in the figure are given above or are self-explanatory, with the exception of the randomization parameter

($r \in [-1,1]$), and the adjustable parametric step vector ($\boldsymbol{\mu}_{\boldsymbol{\alpha}}$). The index variables are *k* and *n*, and are incremented with objective function and temperature update respectively.

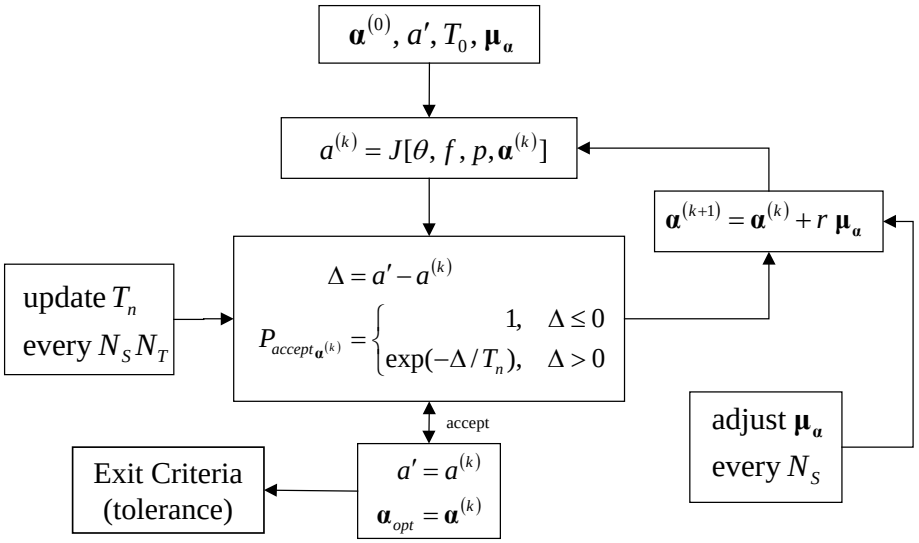

Figure A-5. Block Diagram of Simulated Annealing Implementation

The optimal annealing schedule update formula utilized for this work was (large *t*, *n*),

$$T(t) \sim \frac{D}{\log(t)} \Rightarrow T_n = \frac{T_0}{\log(2+n)}, \tag{125}$$

where *D* is the energy *separating barrier* discussed in [33] and guarantees convergence to the ground state with probability one [7, 8]. The exit criteria is established such that when either the optimization condition has not changed (to within a specified tolerance) for a given temperature update, or the improvement is below a sufficient tolerance for a series of temperature updates, the algorithm terminates. Initial values chosen for this work were based on examining early trials and following recommendations in [7], given as

$$T_0 = 1,\ N_S = 20,\ N_T = 50,\ \boldsymbol{\mu}_{\boldsymbol{\alpha}^{(0)}} = \underline{1},$$

where the initial parametric set is chosen randomly. These choices of parameters produced reasonable results, but whether they are optimal is a question. It has been suggested that one could "optimize the optimizers" by performing repeated SA optimizations using an inner loop encompassed by an SA optimization outer loop that optimizes these parameters choices.

Figure A-6 shows results of SA simulations based on the objective function of Equation (124). A tolerance of 0.01 was chosen, and the results did not vary significantly from the results obtained for a tolerance of 0.1 (similar to Figure A-3). Noteworthy is the actual number of required calculations as opposed to Figure A-3. Similar comparisons have found that SA requires more objective function calls than GA, but as a function of the number of parameters, there appears to be an exponential trend for SA, as opposed to GA, which appears to be more linear.

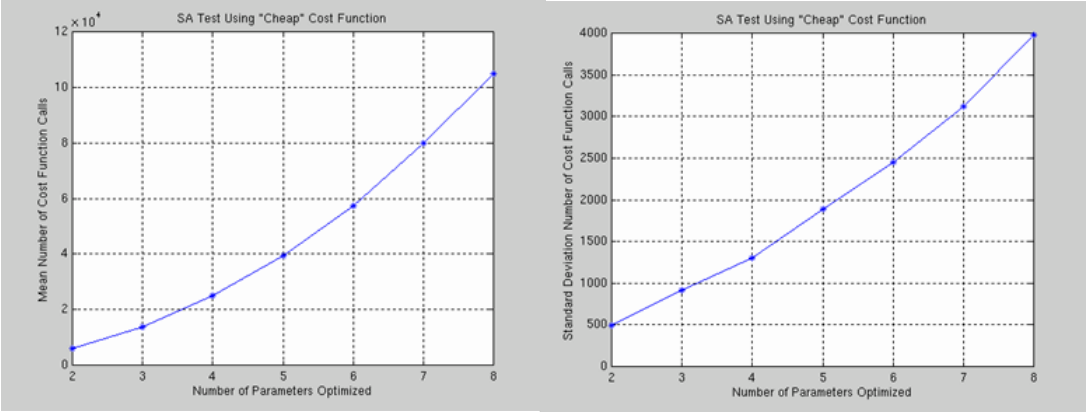

Figure A-6. Performance of Simulated Annealing versus Number of Parameters to Optimize; Required Sorting Iterations Mean (left) and Standard Deviation (right)

A.3 Example GA/SA Comparison with a "Tuned" Objective

To examine further, note that GA may suffer in the case of complex integral equation optima due to the very nature of the solution space. In solving the electromagnetic problem posed in the following, the solution space is expected to be highly tuned to a particular set of parameters. An example objective function was developed as shown in Figure A-7 below.

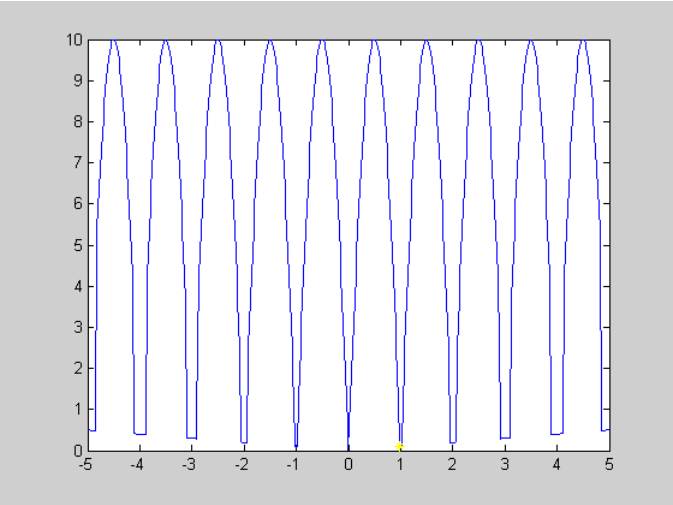

Figure A-7. Example "Tuned" 1-Parameter Objective Function

The optimization for a function of this form is particularly challenging due to the nature of the minima. The function offers several local minima have a well-width inversely proportioned to its depth, with a very slight increase in depth away from the global optimum. It is tempting for an algorithm to choose away from the global optimum. This problem is compounded when multiple parameters are involved, forming a higher dimensional space.

Tests of this function under various algorithm optimization conditions are tabulated below based on each of a variety of GA runs [12] as well as SA.

Table A-1. Tuned Objective Function Example Trials

Algorithm Description	*Correct / Total Trials*
GA; arithmetic crossover, non-uniform mutation, 250 generations	20 / 100
GA; cyclic crossover, non-uniform mutation, 250 generations	12 / 100
GA; simple crossover, non-uniform mutation, 250 generations	12 / 100
GA; arithmetic crossover, uniform mutation, 250 generations	17 / 100
GA; cyclic crossover, uniform mutation, 250 generations	11 / 100
GA; simple crossover, uniform mutation, 250 generations	19 / 100
SA; test for 4 temperature reductions, terminate when within 1% of previous objective	53 / 100

From the above results, the arithmetic crossover, non-uniform mutation GA was chosen to extend to the required optimization for this study. In general, GA had fundamental difficulty in determining the global minimum for a highly tuned point, for even a single-parameter function, however. Given the number of parameters for this problem, it is difficult to say whether any success can be anticipated. The results of SA for the same example above were clearly superior, but also did not find the global solution 100% of the time, and required significantly more cost function evaluations.

In most cases where the global optimum was not located via GA, it was due to the fact that the algorithm chose the second-best solution. Repeating the earlier statement, if one can argue that a reasonable electromagnetic goal is attained to within a required specification, the GA has successfully done its job.

A.4 Search Algorithm Conclusions

While the theoretic condition that SA may approach the global optimum with probability one is attractive, the apparent robustness of GA (ability to consistently find the global solution) and relatively low number of cost function evaluations required, makes GA the best choice for the majority of electromagnetic optimization work.

This work chose to proceed to determine an optimal configuration trade-space via GA for the purpose of further development. As the next section will show, the optimization condition used for observation required approximately two months of high-speed computation to determine. It is expected that a similar SA comparison would require approximately four months to complete. This was not pursued, for reasons that will become clear.

A.5 Initial Investigation of Electromagnetic Optimization using Genetic Algorithms

The optimization objective is based on the reflection loss at the excitation probe input. It is generally accepted that low reflection loss on the input translates to reasonably high gain for electrically small antennas since such antennas are not highly directive as long as the antenna consists entirely of low-loss materials. The relevant equations begin with the objective function

$$\boldsymbol{\alpha}_{opt} = \underset{\boldsymbol{\alpha}}{\operatorname{argmin}}\left[J(\boldsymbol{\alpha})\right], \tag{126}$$

for

$$J(\boldsymbol{\alpha}) = \left\|\mathbf{s}_{11}(\boldsymbol{\alpha})\right\|_f^{\infty}, \tag{127}$$

and $\mathbf{s}_{11}(\boldsymbol{\alpha}) = \left[\left|s_{11}(f_1, g(\boldsymbol{\alpha}))\right|, \left|s_{11}(f_2, g(\boldsymbol{\alpha}))\right|, \ldots, \left|s_{11}(f_N, g(\boldsymbol{\alpha}))\right|\right]^T$. The reflection loss itself is given by

$$\left|s_{11}\right| = \left|\frac{Z_0 - Z_L}{Z_0 + Z_L}\right|, \tag{128}$$

for Z_0 the characteristic impedance of the probe feed, and $Z_L = Z_L(f_n, g(\boldsymbol{\alpha}))$ the calculated input impedance of the antenna feed probe. The input for the antenna is considered to be matched when $Z_0 = Z_L$, resulting in a low reflection loss. The reflection loss is optimized over a reasonably wide bandwidth by adjusting the material parameters associated with the substrate "bricks". It is essential to next understand the manner in which the chosen code obtains the relevant impedance calculation.

For the purpose of this work, it is not the desire to use a GA-style optimizer to develop an end-product but, through the optimization process, to understand the natural optimization trend as it relates to the problem to help draw conclusions about what additional information in the FE-BI construct may be utilized.

The specific geometry for analysis is shown in Figure A-8 and utilizes a substrate size of 7.5cm x 5.1cm x 0.08779cm thick, and patch size (centered) of 5.0cm x 3.4cm. This geometry was chosen to coincide with a test case conducted during the evaluation of the FEMA-BRICK code implementation; it was a test case chosen by the FEMA-BRICK developer for measurement validation [36]. It is a non-ideal case to compare reflection loss to radiation, given the resistive load. Nevertheless, this made for a reasonable starting point.

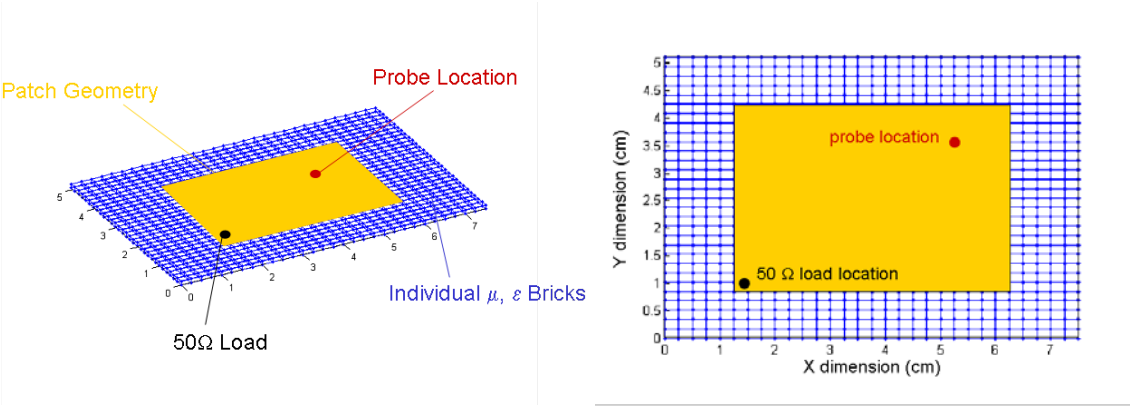

Figure A-8. Patch Antenna Configuration Utilized for Initial Optimization

Optimization parameters are 900 brick contained within the substrate and their values are allowed to vary over four possible values, chosen from those contained in Table A-2: $\boldsymbol{\varepsilon} = [1, 2.17\text{-}j0.0033, 10\text{-}j0.01, 30\text{-}j0.045]$. This enabled a GA code optimization based on two bits per cell, for a chromosome of length 1800.

Table A-2. Materials Considers for Textured Material Substrate Design

Material Name	Permittivity	Composition (Hardened)
Air / Vacuum	1 + j 0	
See FEMA-BRICK Manual	2.17 – j 0.0033	
Stycast	3.3 – j 0.004	Epoxy Resin
Ferro ULF100	10 – j 0.01	$CaMgSi_2O_6$
Ferro ULF280	30 – j 0.045	$BaTiO_3$
Ferro ULF101	100 – j 0.15	Bi – Ba – Nd – Titanate

Clearly, this optimization requires a daunting number of iterations for “brute force” global optimization. To exhaustively test by predicting for all possible combinations

would require 4^{900} trials. Typical wideband runs took on the order of 2 minutes, meaning that an exhaustive search would require more than 10^{536} years! While the global optimum can not be found in a reasonable amount of time this way, observing the progress of a global optimizer may help determine what is of relative importance: making use of the global optimizer in order to gain some insight into the problem, as Goldberg predicted. It was found that while some optimization was accomplished, this particular problem was a case-in-point for a poorly chosen parametric function, such that no real insight into the solution was offered.

The optimization sought was the "best" combination of the individual bricks in order to optimize reflection loss over a band, chosen according to the frequency vector $\mathbf{f} = [f_1, f_2, \ldots, f_N] = [2.65 : 0.01 : 2.75]$ GHz. Arithmetic cross-over with non-uniform mutations were utilized. The optimization was run for a period of approximately two months. The end result was the reflection loss given in Figure A-9 (plotted against the initial reflection loss with constant substrate; $\varepsilon_r = 10 - j0.01$), where a modest reduction over the band of interest is observed. For truly optimized results, performance is generally much better than this, but the number of parameters to optimize is clearly problematic for the GA (or any statistical) routine.

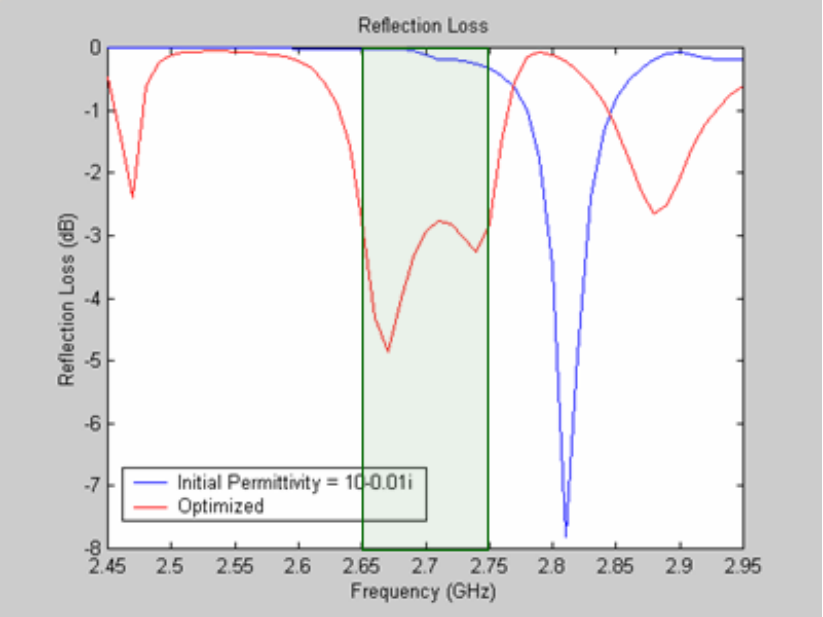

Figure A-9. Genetic Algorithm Probe Feed Reflection Loss Optimization (Optimization Band Shown Shaded In)

As given in Equation (12), the reflection loss curves above are direct results of the computed Z-directed E-field ($E_{Z,probe}$) at the probe location. It is particularly instructive to investigate the electric fields that correspond to regions where the reflection loss is low and high and take note of the fact that there are (theoretically) an infinite number of ways to arrive at a particular refection loss value at any particular point. In fact, one means of performing optimization could involve reorienting the location of the probe itself. The geometry and the possible choices of material parameters are the contraints. The GA permittivity material solution as a function of brick location is shown in Figure A-10.

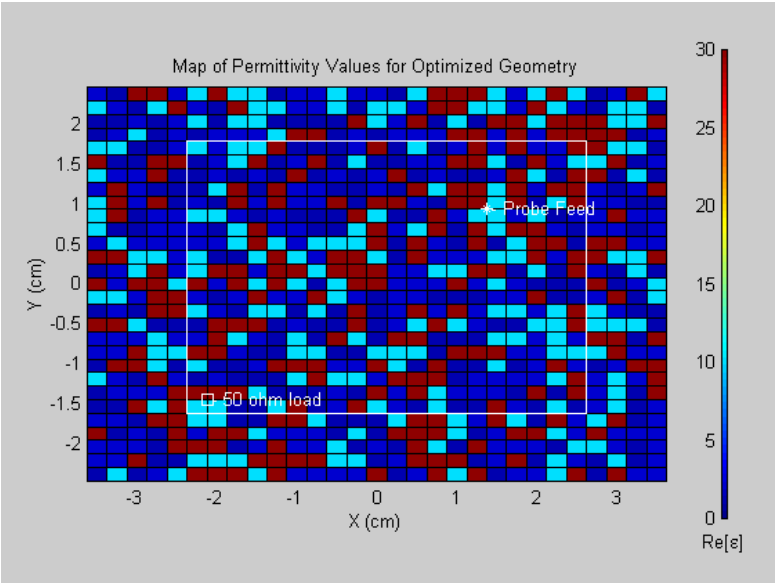

Figure A-10. Permittivity Optimized Brick Configuration

The following figures display the absolute values of E_Z over the single-layer volume at various noted frequencies. The optimized substrate is demonstrated first, starting with the reflection loss minima (2.66 GHz; Figure A-11), and then examining a near-maxima for the same geometry (2.81 GHz; Figure A-12). Following, the original solid substrate ($\varepsilon_r = 10 - j0.01$) Z-directed electric fields are given for corresponding points (2.66 GHz; Figure A-13 and 2.81 GHz; Figure A-14). The fields present in the optimized versus initial substrate configurations are in clear contrast.

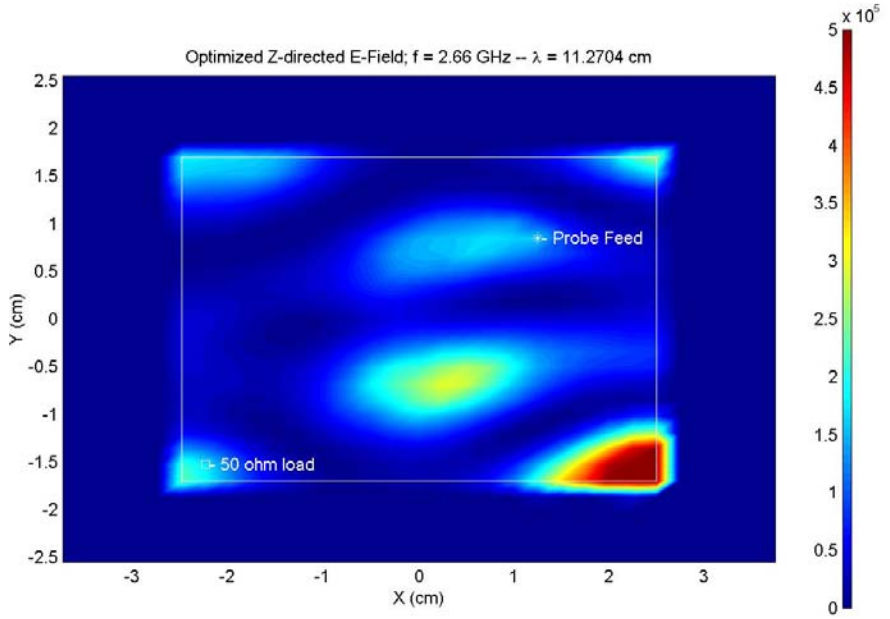

Figure A-11. Optimized Patch Antenna Substrate Z-directed E-field at 2.66 GHz

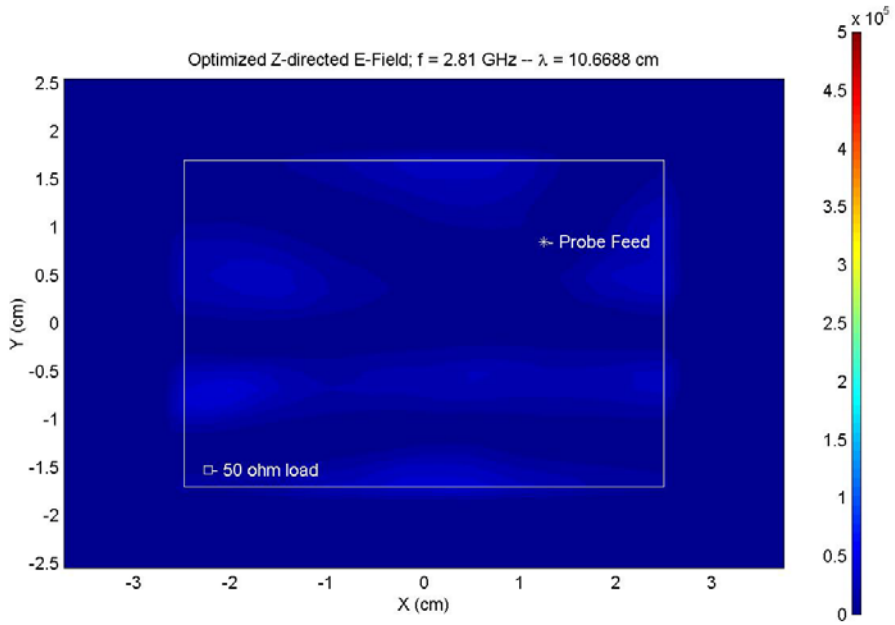

Figure A-12. Optimized Patch Antenna Substrate Z-directed E-field at 2.81 GHz

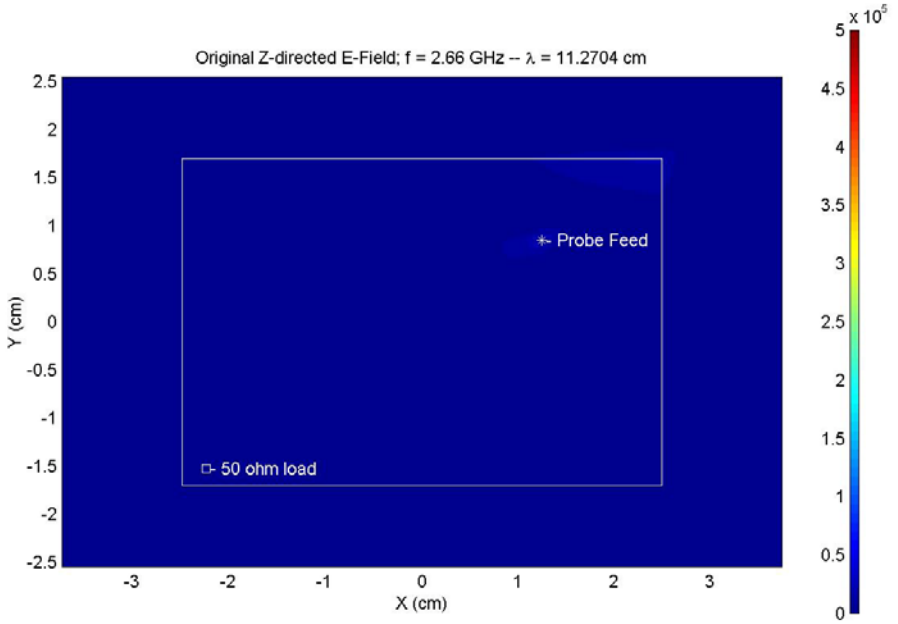

Figure A-13. Patch Antenna Substrate (ε_r = 10-*j*0.01) Z-directed E-field at 2.66 GHz

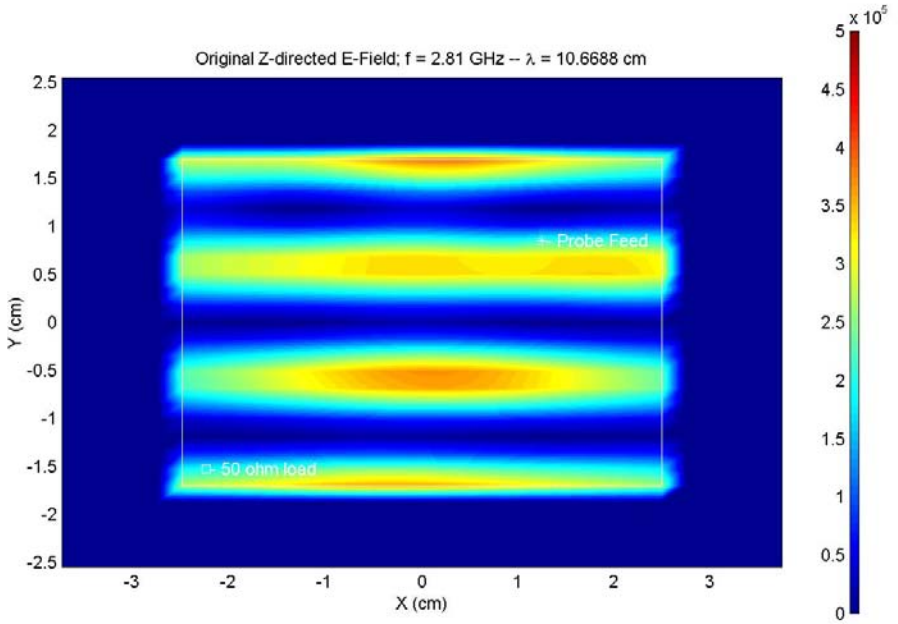

Figure A-14. Optimized Patch Antenna (ε_r = 10-*j*0.01) Substrate Z-directed E-field at 2.81 GHz

These two figures show that E_z (throughout the geometry) has changed markedly and that there is clear structure associated with the changes. Observe that the structural changes in the fields for the optimized geometry appear to be correlated with the material configuration. The reader may have to stare at Figure A-10 and associated E-field unknown solutions for a while to draw this conclusion, however. This result clearly offers little insight into why the design appears to be working.

In general, this problem is too parametrically rich for a GA (or SA) to solve. Even after months of operation, an obvious trend was not observed. More advanced GA approaches (e.g., micro-GA) have not been employed in drawing this conclusion, but it is not necessary. From the initial remarks highlighting the number of years required for an exhaustive search, one is not left with a sense of optimism. In order for such an optimization to work, some engineering judgment and design must play in.

Appendix B: Matrix Decomposition and Solution Detail

This work utilized two principle decomposition approaches which are further described below.

B.1 Constrained Total Least Squares

Early work focused on optimization via a constrained Total Least Squares (TLS) approach that begins with the clear explanation provided by Golub and Van Loan [29] for TLS, with the added complexity of a constraint. The constraint was required to seek the objective, but also caused the system to become overdetermined. Seeking a solution to a basic matrix system ($\mathbf{A} \in \mathbb{C}^{N\times N}$, $\mathbf{x} \in \mathbb{C}^{N\times 1}$, $\mathbf{b} \in \mathbb{C}^{N\times 1}$) given by

$$\mathbf{A}\mathbf{x} = \mathbf{b}, \tag{129}$$

subject to the constraint, $x_n = x_{objective}$, note that

$$\mathbf{A}_u \mathbf{x}_u = \mathbf{b} - \mathbf{a}_n x_{objective} = \mathbf{b}_c, \tag{130}$$

where $\mathbf{A} = \left[\mathbf{A}_u, \mathbf{a}_n\right]$, and $\mathbf{x}_u = \left[x_1, x_2, \ldots, x_{n-1}, x_{n+1}, \ldots, x_{N-1}, x_N\right]^T$. Since $\mathbf{A}_u$ is now overdetermined by the objective removal, the TLS solution is given via the singular value decomposition

$$\mathbf{U}^H \left(\mathbf{M}_r \left[\mathbf{A}_u, \mathbf{b} - \mathbf{a}_n x_{objective}\right] \mathbf{M}_c\right) \mathbf{V} = \quad = \mathrm{diag}\left(\sigma_1, \sigma_2, \ldots, \sigma_{\mathrm{N}}\right), \tag{131}$$

where the **M** matrices are diagonal and are referred to as row-wise and column-wise solution space norm matrices, respectively. The **M** matrices are non-singular by

definition and are used to emphasize certain rows or columns in the solution. Those rows/columns weighted more heavily tend to encourage the TLS solution in their favor.

If $\mathbf{U}$, $\mathbf{V}$, and $\boldsymbol{\Sigma}$ are subsequently partitioned according to

$$\mathbf{U} = \left[\mathbf{U}_1, \mathbf{u}_2\right] \quad \mathbf{V} = \begin{bmatrix} \mathbf{V}_{11} & \mathbf{v}_{12} \\ \mathbf{v}_{21}^T & v_{22} \end{bmatrix} \quad = \begin{bmatrix} \boldsymbol{\Sigma}_1 & 0 \\ 0 & \sigma_N \end{bmatrix} \quad {}_c = \begin{bmatrix} \mathbf{M}_{c_1} & 0 \\ 0 & m_{c_N} \end{bmatrix}, \tag{132}$$

then

$$\mathbf{x}_{u,TLS} = -\frac{1}{v_{22} m_{c_N}} \mathbf{M}_{c_1} \mathbf{v}_{12}, \tag{133}$$

is the unique solution to $\left(\mathbf{A}_u + \Delta\mathbf{A}_u\right)\mathbf{x}_u = \mathbf{b}_c + \Delta\mathbf{b}_c$. In this case, the deviations involved in the solution directly are needed, which are given by [29]

$$\left[\Delta\mathbf{A}_u, \Delta\mathbf{b}_c\right] = -\mathbf{M}_r^{-1}\mathbf{u}_2\sigma_N\left[\mathbf{v}_{12}^T, v_{22}\right]^* \mathbf{M}_c^{-1}. \tag{134}$$

B.2 Sorted Eigendecomposition

The eigendecomposition required for this work simply made use of the standard Matlab library function with a simple sorting operation that re-ordered the eigenvalues according to $\mathrm{Re}\{\lambda_1\} < \mathrm{Re}\{\lambda_2\} < \ldots < \mathrm{Re}\{\lambda_N\}$. Once the sorting index was obtained, the eigenvector matrix was rearranged via a column pivot operation such that

$$\mathbf{X}_{new} = \mathbf{P}\mathbf{X}_{old}, \tag{135}$$

for the appropriate permutation matrix, $\mathbf{P}$ [29].

Appendix C: Matlab Code Module Descriptions

In order to demonstrate the results associated with this work, a library of Matlab routines centered on the exploitation of the FEMA-BRICK Fortran code was developed. This appendix describes the basic modules and their usage. For a copy of the software, please contact the author, Prof Andrew Yagle or Prof John Volakis. The modules and brief description are given below. Typical variable input/output is managed via structured variables, such that all relevant information for a particular system is contained within a single structure. This greatly aids the organization of the optimization from routine to routine. All routines are well-commented and testing scripts are available.

Fema-Brick_RCard_DPatchnewmat.f90: modified version of the original FEMA-BRICK that (when compiled) is called within Matlab via the routine *RunFEMABRICK.m*. All inputs to and outputs from FEMA-BRICK are managed via temporary data files that are read from and written to by the standalone executable. No user interface is available or required. The textured material is managed via a modification to the basic executable that uses the appropriate dielectric brick for the appropriate finite element matrix update.

RunFEMABRICK.m: calls *Fema-Brick_RCard_DPatchnewmat.exe* using values for dielectric texture, size, number of nodes, patch geometry, etc. that establish an appropriate input data file. A working directory is specified as part of the structured input variable where all generated data files are kept. An executable directory is also specified as a pointer to *Fema-Brick_RCard_DPatchnewmat.exe*. The key variable passed to this routine is OutputVars, which is a cell array that specifies all of the desired parameters that FEMA-BRICK should pass back. Obtaining matrix variables, field unknowns, forcing functions and the like are all obtained this way. By allowing the user to specify only the output variables needed as part of the structure, needless waste of memory space is minimized. Where applicable, matrices are stored in Matlab in sparse format, to further save memory space.

RunWidebandFEMABRICK.m: calls *RunFEMABRICK.m* repeatedly to generate the wideband system response variables desired. *RunFEMABRICK.m* can, itself, generate a wideband result in FEMA-BRICK directly, but will not receive (for example) each wideband Green's Function matrix update, if that is desired for each frequency.

FBCase[n].m: initializes the variables needed for a particular case. Example cases which generate the simple patch and the square spiral antenna geometry information are available. This

routine allows for the initialization of different textured material schemes and different frequency vectors.

DisplayField.m and DisplayGeom.m: utilities which produce a graphical representation of the electric field unknowns and the geometry itself, respectively.

GetEigenDecomp.m: obtains all variables associated with the eigendecomposition and optimization. This includes the eigendecomposition (eigenvalue and eigenvector matrix [and inverse]), the LDL decomposition (L inverse), the material transition matrix (pseudo-inverse), the constitutive matrices (with inverses), and γ_n. The probe must be specified and the system matrices, field unknowns and forcing function must be established within the structure of the input variable.

GetEigenBasedFrequencyResponse.m: uses the eigenvalues and γ_n output from *GetEigenDecomp.m* in order to produce the fast wideband solution for a specified frequency vector and center frequency. The output is the wideband result and the normalized frequency vector.

get_candidate_eigenvalues.m: performs the test necessary to determine whether eigenvalues may be used for optimization (based on the discussion of Section 5.4). Parameters for selection of eigenvalues are somewhat subjective, so users may wish to modify the criteria for selection in this script.

place_eig_poles.m: takes as input all eigenvalues and pre-selected eigenvalue locations and outputs the appropriate weight at a given point to apply to an eigenvalue to place it at a desired frequency location (recognizing that several iterations may be required).

eigenweights2matweights.m and matwt2epsilonwt.m: the first performs the conversion between desired eigenvalue weights (as selected by *place_eig_poles.m*), and appropriate material (LDL) diagonal weights, then the second converts that material weighting to permittivity weighting for the textured material update.

REFERENCES

1. Fischer, B.E.; “Two-Dimensional Echo Width Optimization of a Multi-Layer Ogive”, *Report in Support of University of Michigan Directed Study and Qualification*, Jan 2002.
2. Fischer, B.E.; Yagle, A.E.; Volakis, J.L; “Electromagnetic Optimization of a Patch Antenna over a Textured Substrate using Total Least Squares”, *IEEE 2004 Antennas and Propagation Society International Symposium*, Vol 4 , 20-25 Jun 2004, pp. 4428 - 4431.
3. Fischer, B.E.; Yagle, A.E.; Volakis, J.L; “On the Eigen-decomposition of Electromagnetic Systems and the Frequency Dependence of the Associated Eigenvalues”, *IEEE 2005 Antennas and Propagation Society International Symposium*, To Be Published, 2005.
4. Chatterjee A.; Volakis, J.L; Kent, W.J.; “Scattering by a Perfectly Conducting and a Coated Thin Wire Using a Physical Basis Model”, *IEEE Transactions on Antennas and Propagation*, Vol 40, No. 7, Jul 1992.
5. Kempel, L.C.; Volakis, J.L; “TM Scattering by a Metallic Half Plane with a Resistive Sheet Extension”, *IEEE Transactions on Antennas and Propagation*, Vol 41, No. 7, Jul 1993.
6. Kempel, L.C.; Volakis, J.L; Senior, T. B. A.; “Scattering by S-Shaped Surfaces”, *IEEE Transactions on Antennas and Propagation*, Vol 41, No. 6, Jun 1993.
7. Geman, S.; Geman, D.; *IEEE PAMI* **6** 721, 1984.
8. Hajek, B.; *Int. Conf. On Decision and Control* (Piscataway, NJ: IEEE), 1985.
9. Corana, A.; Marchesi, M.; Martini, C.; Ridella, S.; “Minimizing Multimodal Functions of Continuous Variables with the ‘Simulated Annealing’ Algorithm”, *ACM Transactions on Mathematical Software*, Vol. 13, No. 3, pp. 262-280, Sept 1987.
10. Robini, M. C.; Rastello, T.; Magnin, I. E.; “Simulated Annealing, Acceleration Techniques, and Image Restoration”, *IEEE Transactions on Image Processing*, Vol. 8, No. 10, Oct 1999.
11. Dorigo M.; Di Caro, G.; “Ant Colony Optimization: A New Meta-Heuristic”, *Proceedings of the 1999 Congress on Evolutionary Computation, 1999. CEC 99 - 1477 Vol. 2*.
12. Houck, C.R.; Joines, J.A.; Kay, M.G.; *Freeware: Binary and Real-Valued Simulation Evolution for Matlab*, Copyright (C) 1996.
13. Balanis, C. A.; Advanced Engineering Electromagnetics, John Wiley & Sons, New York, 1989.
14. Skinner, J. P.; “AFIT Notes from Course # EE630 Part II”, Nov 1991.
15. McClary, R. L.; “RAM2D 2-D Integral Equation Computer Code”, User’s Manual, Feb 1995.

16. Knott, E. F.; Shaeffer, J. F.; Tuley, M. T.; Radar Cross Section, Artech House, Inc., Norwood MA 02062.

17. Li, Z.; Kiziltas, G.; Volakis, J.L; Kikuchi N.; "Material Design Optimization for Printed Antennas Using the Finite Element-Boundary Integral Method."

18. Kiziltas, G.; D. Psychoudakis, Volakis, J.L; Kikuchi N.; "Topology optimization of dielectric substrates for bandwidth improvements of patch antennas," *IEEE Trans. Antenna and Propagat.,* Vol. 51, Oct. 2003, pp. 2732-2743.

19. Kiziltas, G.; Volakis, J.L; Kikuchi N.; "Metamaterial design via the density method," *2002 IEEE Antennas and Propagation Symposium,* San Antonio, TX, Vol. 1, pp. 748-751.

20. Kiziltas, G.; Y. Koh, Volakis, J.L; Kikuchi, N.; Halloran, J.; "Optimum design and fabrication of volumetric graded substrates for a broadband miniature antenna," 2003 IEEE Int Symposium on Antennas and Propagation, Symposium digest, pp. 485-488, Vol. 1, Columbus, OH.

21. Kiziltas, G.; Psychoudakis, D.; Volakis, J.L; Kikuchi, N.; Halloran, J.; "Miniature Antenna Designs on Metamaterial Substrates", 8th Int. Conference on Electromagnetics in Advanced Appl. (ICEAA), Conf. Proceedings, pp. 431-434, 2003, Torino, Italy.

22. Kiziltas, G.; Volakis, J.L; Kikuchi, N.; Halloran, J.; "Miniature broadband SATCOM antenna design using automated material optimization techniques," 2004 FEM workshop, Madrid, Spain.

23. Kiziltas, G.; Koh, Y.; Volakis, J.L; Kikuchi, N.; Halloran, J.; "Optimum Design and Fabrication of Volumetric Graded Substrate for a Broad-band Miniature Antenna", IEEE 2003Antennas and Propagation Society International Symposium, Vol 1 , 22-27 June 2003, pp. 485-488.

24. Psychoudakis, D.; Knapp, A.; Kiziltas, G.; Volakis, J.L.; Halloran, J.; "Textured LTCC Substrates for Printed Antenna Miniaturization and Bandwidth Improvement", IEEE 2003Antennas and Propagation Society International Symposium, Vol 3 , 22-27 June 2003, pp. 375 -378.

25. Jin, J.-M.; Volakis, J.L.; "A Finite-Element-Boundary-Integral Formulation for Scattering by Three-Dimensional Cavity-Backed Apertures", IEEE Transactions on Antennas and Propagation, Vol: 39, Issue: 1, Jan. 1991.

26. Jin, J.-M.; Volakis, J.L.; Collins, J.D.; "A Finite-Element-Boundary-Integral Method for Scattering and Radiation by Two- and Three-Dimensional Structures", IEEE Antennas and Propagation Society Magazine, 33(3):22-32, June 1991.

27. Jin, J.-M.; Volakis, J.L.; "A Hybrid Finite Element Method for Scattering and Radiation by Microstrip Patch Antennas and Arrays Residing in a Cavity", IEEE Antennas and Propagation Society Magazine, 39(11):1598-1604, November 1991.

28. Volakis, J.L.; Chatterjee, A.;. Kempel, L.C.; *Finite Element Method for Electromagnetics: Antennas*, Microwave Circuits, and Scattering Applications, IEEE Press, New York NY, 1998.

29. Golub, G.H.; Van Loan, C.F.; Matrix Computations; Third Edition, The Johns Hopkins University Press, Baltimore and London, 1996.

30. Haupt, R.L.; "An Introduction to Genetic Algorithms for Electromagnetics", IEEE Antennas and Propagation Magazine, Vol 37, No. 2, Apr 1995.

31. Johnson, J.M.; Rahmat-Samii, Y.; "Genetic Algorithms in Engineering Electromagnetics", IEEE Antennas and Propagation Magazine, Vol 39, No. 4, Apr 1997.

32. Scales, J.A.; Smith, M.L.; Fischer, T.L.; "Global Optimization Methods for Multimodal Inverse Problems", Journal for Computational Physics, 103, 1992.

33. Hoffmann, K.H.; Salamon, P.; "The Optimal Simulated Annealing Schedule for a Simple Model", J. Phys. A: Math. Gen 23 (1990), 3511-3523.

34. Rao, S. S.; *Engineering Optimization: Theory and Practice*, 3rd ed. New York, Wiley, 1996

35. Rahmat-Samii, Y.; Michielssen, E.; *Electromagnetic Optimization by Genetic Algorithms*, New York, Wiley, 1999.

36. Jin, J.-M.; Volakis, J.L.; Alexanian, A.; "Electromagnetic Scattering and Radiation from Microstrip Patch Antennas and Arrays Residing in a Cavity", Project Report and User's Guide for FEMA-BRICK, 1991.

37. Erdemli, Y.E.; Reddy, C.J.; Volakis, J.L; "AWE Technique in Frequency Domain Electromagnetics", *Journal of Electromagnetic Waves and Applications*, Vol 13, 1999, pp. 359-378.

38. Gong, J.; Volakis, J.L; "AWE Implementation for Electromagnetic FEM Analysis", *Electronics Letters*, Vol. 32, No. 24, 21 Nov 1996, pp. 2216-2217.

39. Miller, E.K.; Burke, G.J; "Using Model-based Parameter Estimation to Increase the Physical Interpretability and Numerical Efficiency of Computational Electromagnetics", *Computer Physics Communications*, Vol. 68, No. 1-3, 1991, pp. 43-75.

40. Burke, G.J.; Miller, E.K.; Chakrabarthi, S.; Demarest, K.; "Using Model-based Parameter Estimation to Increase the Efficiency of Computing Electromagnetic Transfer Functions", *IEEE Trans. Magnetics*, Vol. 25, No. 4, 1989, pp. 2807-2810.

41. Coifman, R.; Rokhlin, V.; Wandzura, S.; "The Fast Multipole Method for the Wave Equation: A Pedestrian Prescription", *IEEE Antennas and Propagation Magazine*, Vol. 35, No. 3, 1993, pp. 7-12.

42. Ferro Performance Materials Company Ceramic Composite Website Address; http://www.ferro.com/our+products/electronic/products+and+markets/chip+component+materials/dielectric+formulations+for+ceramic+capacitors.htm.